UNIVERSITY OF OKLAHOMA
GRADUATE COLLEGE

MULTISCALE ANALYSIS OF SEISMIC EVENT SOURCE PARAMETER RESOLUTION AND CHARACTERIZATION

A DISSERTATION
SUBMITTED TO THE GRADUATE FACULTY
in partial fulfillment of the requirements for the
Degree of
DOCTOR OF PHILOSOPHY

By
JIEWEN ZHANG
Norman, Oklahoma
2021

MULTISCALE ANALYSIS OF SEISMIC EVENT SOURCE PARAMETER RESOLUTION AND CHARACTERIZATION

A DISSERTATION APPROVED FOR THE
SCHOOL OF GEOSCIENCES

BY THE COMMITTEE CONSISTING OF

Dr. Xiaowei Chen, Chair

Dr. Brett M. Carpenter

Dr. Junle Jiang

Dr. Jacob I. Walter

Dr. Xingru Wu

Acknowledgement

No one could ever expect the pandemic to have happened all over the world in early 2020 and still have not yet ceased to enlarge, so first I would like to thank myself for getting through it and keeping healthy at this point to finish this dissertation. This brings out the first person I would like to thank rather than myself – my advisor Dr. Xiaowei Chen, who has kept supporting my Ph.D. work during the pandemic after I decided to postpone my graduation twice from early 2020 due to the global situation, but I would like to thank her more on her patience and persistence to teach me knowledge related to my research since 2016 and great tolerance when I made mistakes. Then I would like to thank Dr. Rachel E. Abercrombie, who is in fact my co-advisor, for her guidance that helped me gain knowledge and experience step-by-step and sometimes help to guide my personal problems. Without their help, I would not be able to build myself towards a seismologist, and I wish to always keep connected with them as long as I still stay in academia.

I would also like to thank the rest of my committee members, Dr. Brett Carpenter, Dr. Junle Jiang, Dr. Jake Walter and Dr. Xingru Wu for their support and comments that greatly improved my research work and dissertation.

Next, I need to thank my parents who are on the other side of the Pacific. We are always connected even we are not together geographically. Without their mental support, I would have never been able to step towards the end of my Ph.D. life. It was so pitiful that my parents were not able to come over to attend my graduation ceremony which usually happens only once in a lifetime.

I also need to thank all the friends I got to know since I arrived here in 2016. I am not going to put their names here, but they are an important part of my daily life. Some of them are still here, some have graduated and left here, and some have changed their major; but they are always in my mind.

Finally, I need to thank some people I got to know on the Internet who share the same interests as me, but have never met, they are my source of happiness. I also need to thank people I do not know at all but have contributed to and sacrificed in fighting against the COVID-19, the medical workers risking themselves on the very frontline, the scientists who are dedicated to vaccine development, and everyone working in every single area that keeps the world running during the very hard time.

Chapters 2, 3 and 4 discussed in this dissertation are from 3 papers to be published in the near future. I am the first author of all 3 papers with the guidance of the co-authors of each.

Table of Contents

List of Figures

List of Tables

Chapter 0 Abstract of the dissertation

Earthquake source parameters such as stress drop help us understand the underlying physics of tectonic stress loading and releasing associated with the occurrence of earthquakes, and the influence of human activity on the underground stress status whether in the resource exploration area or in the urban area. In my Ph.D. research, I aim at studying regional and local datasets in different tectonic settings to understand the relationship between stress drop and some other source parameters and those physical processes.

To understand how the stress drop variability helps interpret the fault behaviors related to a large earthquake, I examine the source parameters including stress drop, corner frequency and seismic moment of thousands of small earthquakes along the San Andreas fault (SAF) at the Parkfield area in California, USA. In this research, I first try to understand the uncertainties of these source parameters among different studies and find that it is important to reasonably organize data spatially and temporally to account for the heterogeneity of material properties, such as attenuation and shear wave velocity variations. These results show that proper corrections significantly reduce the scatter in stress drop estimations, and weaken depth/magnitude dependence. The results also suggest that frequency bandwidth has strong influence on corner frequency estimations, insufficient bandwidth may cause systematic underestimation and increased stress drop scatter. The well-resolved stress drops are independent of magnitude within a resolvable corner frequency range, suggesting that these earthquakes follow self-similar rupture processes. The results exhibit complex stable spatial patterns with no clear correlation

with slip partition or slip distributions of the 2004 M6 earthquake. In some regions with a sufficient number of earthquakes, I resolve robust temporal variations that indicate stress drop decrease following the 2004 earthquake, and gradual recovery. These temporal variations do not affect the long-term stress drop spatial variations, suggesting local material properties may control the spatial heterogeneity of stress drop.

To further analyze the source of the uncertainties in the stress drop estimation, I compare the Parkfield small earthquake corner frequency and stress drop estimates using different methods, parameter selection and datasets. A new method based on global optimization and spectral decomposition is proposed and compared to published methods and results. It is found that with sufficient bandwidth, different methods can obtain similar results. When bandwidth is insufficient, corner frequencies above the resolution limit can have very different results depending on different methods. Corner frequencies that are within the resolution limits tend to be similar with different methods. These results suggest that stress drop interpretations should carefully consider the resolution limit for given dataset, and consistency across multiple methods is important to ensure the source parameters are well resolved. Results in this study may help understand the strong variability of stress drop and corner frequency estimates from different studies when they are compiled for comparison.

Finally, I apply the knowledge and practice to microseismic events that occurred during Hydraulic-Fracturing (HF) to examine the similarity and differences in source parameter patterns between earthquakes occurring on faults and microseismic events occurring on hydraulic fractures. To fulfill this, I invert for a 1D velocity model based

on sonic logs and perforation shots. Then, I build a microseismic event catalog by detecting microseismic events from raw microseismic data using Short-Time Average and Long-Time Average Ratio (STA/LTA) method, and locating these events using the inverted 1D velocity model. Using spectra with high signal-to-noise ratio, I obtain source parameters (corner frequency, source radius, and relative stress change) of the detected microseismic events using the new developed method in previous chapters. The high-resolution location and source parameters exhibit spatial migration of microseismic events following fluid diffusion curve, and gradual changes of source parameters with distance from the fracturing point. These observations suggest an influence of fluid on event occurrence and source processes. These microseismic events have relative stress changes increasing with magnitude, suggesting they are non-self-similar, which is different from the natural earthquakes studied in the Parkfield area as well as some other previous research. S/P amplitude ratio analysis of these microseismic events suggests these events are mostly tensile failure and mixed tensile/shear failure events, differing from shear-failure dominated natural earthquakes. My results suggest that microseismic events occurring on hydraulic fractures can have different source processes from natural earthquakes occurring on pre-existing faults.

Chapter 1 Introduction

Earthquakes happen on a daily basis with different sizes and released energy. Though the majority of them are minor and cannot even be felt by humans, some of them release a significant amount of energy and cause catastrophic economic losses and casualties. Examples include the 2008 M8 Wenchuan Earthquake in China that caused collapsed buildings and landslides, and 2011 M9 Tohoku Earthquake that triggered strong tsunami waves that exceeded maximum predicted wave height.

Earthquake occurrence is accompanied with stress drop within the rupture zone and stress increase or decrease in the surrounding areas. Understanding the stress change from earthquakes may provide some clues on the fundamental earthquake scaling relationships and how the earthquake occurrence is related to the tectonic background and fault structures. Earthquakes can have complex patterns of co-seismic and post-seismic stress changes (e.g., *Jiang et al., 2021*). Measurement of stress changes is subject to limitations of observational data and uncertainties due to inversion methods. For large earthquakes, slip models from different studies can be different; however, in most cases, the peak slip and average slip could be similar (e.g., *Ye et al., 2018*). For smaller earthquakes, measuring stress drop is more challenging, and often requires an assumed source model. Previously reported earthquake stress drops range over four orders of magnitude; however, on average, most studies report stress drop is independent of earthquake magnitude (e.g., *Allmann & Shearer, 2009; Abercrombie, 2021*). This indicates earthquake rupture is self-similar, meaning that the average shear stress change remains constant for earthquakes of different sizes. Understanding earthquake scaling relationship allows us to extrapolate the observations of abundant small earthquakes to infrequent larger earthquakes. However, different studies may observe different scaling relationships due to methodology or data processing differences. For example, using the same southern California dataset, *Shearer et al., (2006)* reported self-similar behavior, while *Trugman & Shearer (2017)* observed non-self-similarity. *Shearer et al., (2019)* further evaluated the inversion method, and found that tradeoffs between different parameters can lead to different results.

In this dissertation, I use a well-recorded dataset with sufficient frequency bandwidth, and improved methodology to measure source parameters for small earthquakes in Parkfield, California, to better understand the influence of various factors on source parameter uncertainties. The improved methodology is then applied to microseismic events occurred during hydraulic fracturing experiment to investigate the similarity and differences of source processes between different types of seismic events.

1.1 Stress drop estimation for small earthquakes

Measuring small earthquakes stress drop is hard due to many limitations including low seismic signal quality, poor azimuthal coverage, and limited frequency response on seismic instruments. Given the existence of these challenges, assumptions are made to derive stress drops from dynamic earthquake source models, such as *Brune (1970)* and *Madariaga (1976)*. For a circular crack model, the relationships among source dimension, stress drop, moment and corner frequency can be simplified via the following equations *(Eshelby, 1957; Brune, 1970; Madariaga, 1976)*:

$$\Delta\sigma = \frac{7}{16}\left(\frac{M_0}{r^3}\right), f_c = k\frac{\beta}{r} \tag{1.1}$$

where f_c is the corner frequency that links to the source duration of an earthquake, β represents the shear velocity, r is the source radius, M_0 is the seismic moment and $\Delta\sigma$ is the stress drop. k is a constant that depends on model assumptions, such as the source geometry, and rupture velocity (*Kaneko & Shearer, 2014; 2015*). Using different k values can cause significant differences in the absolute values of stress drops, for example, Brune-type stress drops are approximately 5 times lower than Madariaga-type stress drops. It is important to note that the circular rupture assumption is very rough and oversimplified, and growing data suggests that small earthquakes can exhibit significant rupture complexity (*Allmann & Shearer, 2007; Uchide et al., 2014; Moyer et al., 2018*).

1.2 Approaches to estimate stress drop

The corner frequency can be measured from event source spectrum by fitting a theoretical source model, such as Brune's model (*Brune, 1970*), then stress drop can be computed from the corner frequency. Because the observed displacement spectra combine propagation along the ray path, site responses, and event source terms, proper approaches are needed to isolate the event source terms. Multiple approaches have been proposed by different studies to obtain the source terms and measure stress drop. Here, I will focus on two approaches: Spectral Decomposition and Stacking Method (*Shearer et al., 2006a*) and the Spectral Ratio Method (e.g., *Abercrombie, 2014*).

1) Spectral Decomposition and Stacking Method targets at deriving a global

empirical correction spectrum (ECS) using stacked source spectra of earthquakes. It uses an iterative approach to separate observed spectra on seismometers into source term, station term and path term, then utilize the source term for the stacking process (*Shearer et al., 2006a*). Some variants include *Baltay et al. (2010)*, *Trugman & Shearer (2017)* and *Chen & Abercrombie (2020)*.

2) The spectral ratio method solves for corner frequency of an earthquake by using a nearly collocated smaller event as the Empirical Green's Function (EGF) for a target larger event. First, it calculates the ratio between the recorded spectra of the target earthquake and an EGF event at the same station; then, the ratio is fitted to a theoretical model to obtain the corner frequencies for both the target and EGF events. By calculating the ratio between the recorded spectra at the same station, the path and station terms are canceled out for the nearly collocated event pair. The stability of the method relies on careful parameter and EGF selection.

In this study, both Spectral Decomposition/Stacking Method and the Spectral Ratio Method are included for discussion.

1.3 Earthquake scaling relationship and self-similarity

Earthquake stress drop can help indicate whether earthquakes with different magnitudes are associated with the same physical processes (self-similarity) (*Aki, 1967*). More specifically, if the moment and earthquake dimension (slip and size) are uniformly scaled for small and large earthquakes, the corner frequency will be inversely proportional to the cubic root of the seismic moment, then stress drop should be independent of earthquake size based on equation 1.1. This was supported by multiple studies covering different magnitude ranges, from small and moderate (*Imanishi & Ellsworth, 2006; Allmann & Shearer, 2007; Uchide et al., 2014; Goebel et al., 2015*) to large ones (*Allmann & Shearer, 2009*), but some other studies reported non-self-similarity for earthquakes in different regions (*Mayeda et al., 2005; Oye et al., 2005; Imanishi & Uchide, 2014*).

1.4 Microseismicity

For microseismic events triggered by hydraulic fracturing during oil and gas exploration, it has long been concerned whether they are self-similar. Self-similarity has been found among natural earthquakes (e.g., *Allmann & Shearer, 2009*) and induced earthquakes (e.g., *Wu et al., 2018*), while microseismic events, generally with much lower magnitude than both observable natural and induced earthquakes, are thought to be non-self-similar (e.g., *Urbancic & Young, 1993; Viegas et al., 2015*). It remains unclear whether the inconsistency is from the difference in faulting mechanism: natural/induced earthquakes are mostly shear failure, while the microseismic events are a combination of tensile and shear failure (*Maxwell, 2011; Van der Baan et al., 2013*). The tensile events, generally associated with non-Double-Couple mechanism, are often observed during hydraulic fracturing (*Vavrycuk, 2001; Baig & Urbancic, 2010; Song & Toksöz, 2011*). Based on the far-field spectrum of tensile failure source derived by *Walter & Brune (1993), Eaton et al. (2014)* obtained a non-self-similar relationship between source radius and seismic moment. These may suggest that the source process of microseismic events differs from natural and induced earthquakes.

1.5 Structure of the dissertation

Below is a summary of the topics in the chapters:

Chapter 2: Spatiotemporal variability of earthquake source parameters at Parkfield, California, and their relationship with the 2004 M6 earthquake

Chapter 3: Evaluating source parameters resolution of small earthquakes from multiple factors – An example at Parkfield, California

Chapter 4: High-resolution source mechanism analysis of microseismicity during hydraulic fracturing

One of the most important topics in this dissertation is to understand whether the earthquakes are self-similar, which requires accurate estimation of stress drops of earthquakes. This also involves different types of earthquakes that occurred with different mechanisms and in different circumstances (natural and microseismic events as mentioned above). To achieve this goal, I start in Chapter 2 by evaluating the uncertainties introduced during the process of stress drop estimation for small natural earthquakes in Parkfield, and investigating the influence of various factors on stress drop scaling using a high-resolution borehole network; then in Chapter 3, I compare borehole and surface networks to systematically quantify the factors that affect the accuracy of stress drop estimations, such as data organization, parameter selection, method selection; finally, in Chapter 4, I apply the knowledge gained in the previous two chapters to investigate the scaling relationship of source parameters for microseismic events that involve tensile failure, and the potential difference in source processes from natural earthquakes studied in chapters 2 and 3.

Another important topic is the interpretation of crustal stress distributions as a result of large earthquakes and different slip behaviors. In Chapter 2, after careful evaluation of stress drop uncertainties, I use the stress drop values to understand how the fault behaviors change over space and time in response to the major 2004 M6 Parkfield earthquake. The results show complex spatial patterns that are stable with time. Different spatial patches with high or low stress drops are identified; however, there is no clear relationship between these patches and slip behavior (creeping or locked) or mainshock slip distributions, which suggests that the stress distribution is more related to heterogeneous fault structures. The temporal changes after the 2004 M6 earthquake are relatively small compared to the spatial heterogeneity, and different patches have different temporal responses. In some regions with a sufficient number of earthquakes, a stress drop decrease following the M6 earthquake and a gradual recovery are resolved. In Chapter 4, I characterize the spatiotemporal distribution of source parameters of microseismic events by analyzing their relationship with distances from fracturing points. The results show gradual increase of relative stress drop and source radius with distance from the fracturing point, suggesting possible influence of fluid on event source processes.

References

Abercrombie, R. E. (2021). Resolution and uncertainties in estimates of earthquake stress drop and energy release. *Philosophical Transactions of the Royal Society A: Mathematical, Physical and Engineering Sciences* (Vol. 379). https://doi.org/10.1098/rsta.2020.0131

Allmann, B. P., & Shearer, P. M. (2007). Spatial and temporal stress drop variations in small earthquakes near Parkfield, California. *Journal of Geophysical Research: Solid Earth*, *112*(4), 1–17. https://doi.org/10.1029/2006JB004395

Allmann, B. P., & Shearer, P. M. (2009). Global variations of stress drop for moderate to large earthquakes. *Journal of Geophysical Research: Solid Earth*, *114*(1), 1–22. https://doi.org/10.1029/2008JB005821

van der Baan, M., Eaton, D., & Dusseault, M. (2013). Microseismic monitoring developments in hydraulic fracture stimulation. *ISRM International Conference for Effective and Sustainable Hydraulic Fracturing 2013*, 439–466. https://doi.org/10.5772/56444

Baig, A., & Urbancic, T. (2010). Microseismic moment tensors: A path to understanding frac growth. *The Leading Edge*, *29*(3), 320–324. https://doi.org/10.1190/1.3353729

Baltay, A., Prieto, G., & Beroza, G. C. (2010). Radiated seismic energy from coda measurements and no scaling in apparent stress with seismic moment. *Journal of Geophysical Research: Solid Earth*, *115*(8), 1–12. https://doi.org/10.1029/2009JB006736

Brune, J. N. (1970). Tectonic stress and the spectra of seismic shear waves from earthquakes. *Journal of Geophysical Research*, *75*(26), 4997–5009. https://doi.org/10.1029/JB075i026p04997

Chen, X., & Abercrombie, R. E. (2020). Improved approach for stress drop estimation and its application to an induced earthquake sequence in Oklahoma. *Geophysical Journal International*, *223*(1), 233–253. https://doi.org/10.1093/gji/ggaa316

Eaton, D. W., van der Baan, M., Birkelo, B., & Tary, J. B. (2014). Scaling relations and spectral characteristics of tensile microseisms: Evidence for opening/closing cracks during hydraulic fracturing. *Geophysical Journal International*, *196*(3), 1844–1857. https://doi.org/10.1093/gji/ggt498

Eshelby JD. (1957). The determination of the elastic field of an ellipsoidal inclusion, and related problems. *Proceedings of the Royal Society of London. Series A. Mathematical and Physical Sciences*, *241*(1226), 376–396. https://doi.org/10.1098/rspa.1957.0133

Goebel, T. H. W., Hauksson, E., Shearer, P. M., & Ampuero, J. P. (2015). Stress-drop heterogeneity within tectonically complex regions: A case study of San Gorgonio Pass, southern California. *Geophysical Journal International*, *202*(1), 514–528. https://doi.org/10.1093/gji/ggv160

Imanishi, K., & Ellsworth, W. L. (2006). Source scaling relationships of microearthquakes at Parkfield, CA, determined using the SAFOD Pilot Hole Seismic Array (pp. 81–90). https://doi.org/10.1029/170GM10

Jiang, J., Bock, Y., & Klein, E. (2021). Coevolving early afterslip and aftershock signatures of a San Andreas fault rupture. *Science Advances*, *7*(15), eabc1606. https://doi.org/10.1126/sciadv.abc1606

Kaneko, Y., & Shearer, P. M. (2014). Seismic source spectra and estimated stress drop derived from cohesive-zone models of circular subshear rupture. *Geophysical Journal International*, *197*(2), 1002–1015. https://doi.org/10.1093/gji/ggu030

Kaneko, Y., & Shearer, P. M. (2015). Variability of seismic source spectra, estimated stress drop, and radiated energy, derived from cohesive-zone models of symmetrical and asymmetrical circular and elliptical ruptures. *Journal of Geophysical Research: Solid Earth*, *120*(2), 1053–1079. https://doi.org/10.1002/2014JB011642

Madariaga, R. (1976). Dynamics of an expanding circular fault. *Bulletin of the Seismological Society of America*, *66*(3), 639–666. Retrieved from http://bssa.geoscienceworld.org/content/66/3/639.abstract

Maxwell, S. (2011). Microseismic hydraulic fracture imaging: The path toward optimizing shale gas production. *The Leading Edge*, *30*(3), 340–346. https://doi.org/10.1190/1.3567266

Mayeda, K., Gök, R., Walter, W. R., & Hofstetter, A. (2005). Evidence for non-constant energy/moment scaling from coda-derived source spectra. *Geophysical Research Letters*, *32*(10), 1–4. https://doi.org/10.1029/2005GL022405

Moyer, P. A., Boettcher, M. S., McGuire, J. J., & Collins, J. A. (2018). Spatial and Temporal Variations in Earthquake Stress Drop on Gofar Transform Fault, East Pacific Rise: Implications for Fault Strength. *Journal of Geophysical Research: Solid Earth*, *123*(9), 7722–7740. https://doi.org/10.1029/2018JB015942

Oth, A., Bindi, D., Parolai, S., & di Giacomo, D. (2011). Spectral analysis of K-NET and KiK-net data in Japan, Part II: On attenuation characteristics, source spectra, and site response of borehole and surface stations. *Bulletin of the Seismological Society of America*, *101*(2), 667–687. https://doi.org/10.1785/0120100135

Oye, V., Bungum, H., & Roth, M. (2005). Source parameters and scaling relations for mining-related seismicity within the Pyhäsalmi ore mine, Finland. *Bulletin of the Seismological Society of America*, *95*(3), 1011–1026. https://doi.org/10.1785/0120040170

Shearer, P. M., Prieto, G. A., & Hauksson, E. (2006). Comprehensive analysis of earthquake source spectra in southern California. *Journal of Geophysical Research: Solid Earth*. https://doi.org/10.1029/2005JB003979

Shearer, P. M., Abercrombie, R. E., Trugman, D. T., & Wang, W. (2019). Comparing EGF Methods for Estimating Corner Frequency and Stress Drop From P Wave Spectra. *Journal of Geophysical Research: Solid Earth*, *124*(4). https://doi.org/10.1029/2018JB016957

Song, F., & Toksöz, M. N. (2011). Full-waveform based complete moment tensor inversion and source parameter estimation from downhole microseismic data for hydrofracture monitoring. *Geophysics*, *76*(6). https://doi.org/10.1190/geo2011-0027.1

Trugman, D. T., & Shearer, P. M. (2017). Application of an improved spectral decomposition method to examine earthquake source scaling in Southern California. *Journal of Geophysical Research: Solid Earth*, *122*(4), 2890–2910. https://doi.org/10.1002/2017JB013971

Uchide, T., Shearer, P. M., & Imanishi, K. (2014). Stress drop variations among small earthquakes before the 2011 Tohoku-oki, Japan, earthquake and implications for the main shock. *Journal of Geophysical Research: Solid Earth*, *119*(9), 7164–7174. https://doi.org/10.1002/2014JB010943

Urbancic, T. I., & Young, R. P. (1993). Space-time variations in source parameters of mining-induced seismic events with M < 0. *Bulletin - Seismological Society of America*, *83*(2), 378–397.

Vavryčuk, V. (2001). Inversion for parameters of tensile earthquakes. *Journal of Geophysical Research: Solid Earth*, *106*(B8), 16339–16355. https://doi.org/10.1029/2001JB000372

Viegas, G., Urbancic, T., Baig, A., & Von Lunen, E. (2015). Rupture dynamics and source scaling relations of microseismic hydraulic fractures in shale reservoirs. *13th ISRM International Congress of Rock Mechanics*, *2015-MAY*(May), 1–10.

Walter, W. R., & Brune, J. N. (1993). Spectra of seismic radiation from a tensile crack. *Journal of Geophysical Research: Solid Earth*, *98*(B3), 4449–4459. https://doi.org/10.1029/92JB02414

Wu, Q., Chapman, M., & Chen, X. (2018). Stress-drop variations of induced earthquakes in Oklahoma. *Bulletin of the Seismological Society of America*, *108*(3), 1107–1123. https://doi.org/10.1785/0120170335

Ye, L., Kanamori, H., & Lay, T. (2018). Global variations of large megathrust earthquake rupture characteristics. *Science Advances*, *4*(3), 1–8. https://doi.org/10.1126/sciadv.aao4915

Chapter 2 Spatiotemporal variability of earthquake source parameters at Parkfield, California, and their relationship with the 2004 M6 earthquake

2.1 Abstract

Earthquake stress drop is an important source parameter that directly links to strong ground motion and fundamental questions in earthquake physics. Stress drop estimations are subject to significant uncertainties due to factors such as variations in material properties and data limitations, which limits the applications of stress drop interpretations. Using a high-resolution borehole network, we analyze 4537 earthquakes in the Parkfield area in Northern California between 2001 and 2016 with spectral decomposition and an improved stacking method. To evaluate the influence of spatiotemporal variations of material properties on stress drop estimations, we apply six different strategies to account for spatial variations of velocity and attenuation changes, and divide earthquakes into three separate time periods to correct temporal variations of attenuation. These results show that proper corrections significantly reduce the scatter in stress drop estimations, and weaken depth/magnitude dependence. We further investigate the influence of data limitations on stress drop estimations, and find that insufficient bandwidth may cause systematic underestimation and increased stress drop scatter. The results exhibit complex stable spatial patterns with no clear correlation with slip partition or slip distributions of the 2004 M6 earthquake. In some regions with sufficient number of earthquakes, we resolve robust temporal variations that indicate stress drop decrease following the 2004 earthquake, and gradual recovery.

These temporal variations do not affect the long-term stress drop spatial variations, suggesting local material properties may control the spatial heterogeneity of stress drop.

2.2 Introduction

The stress drop is a measure of the average stress changes during an earthquake. It is one of the most important source parameters that is directly related to strong ground motion and fundamental problems earthquake physics. It is superficially straightforward to compute stress drop from spectral analysis based on corner frequency, but the high variability, both within individual studies (e.g., *Abercrombie et al., 2017*) and between different studies (e.g., *Pennington et al., 2021*), indicates that stress drop measurements are often subject to large uncertainties (e.g., *Abercrombie, 2021*). Published measurements span 4 orders of magnitude, and until real variability can be distinguished from the large uncertainties, the potential for using stress drop measurements to probe the physics of the rupture process, and to assist in the prediction of future ground motions is severely limited (e.g., *Hardebeck, 2020; Molkenthin et al., 2017*).

Earthquake stress drop can help understand whether earthquakes with different magnitudes are associated with the same physical processes (self-similarity) (*Aki, 1967*). Stress drop has been found to be independent of magnitude by multiple studies, and compilations of studies, covering different magnitude ranges, from small and moderate (*Allmann & Shearer, 2007; Goebel et al., 2015; Imanishi & Ellsworth, 2006; Uchide et al., 2014*) to large ones (*Allmann & Shearer, 2009*). In contrast, other studies have reported non-self-similarity, typically over smaller magnitude ranges (*Imanishi &*

Uchide, 2017; Mayeda et al., 2005; Oye et al., 2005). Spatial and temporal variations of stress drop have the potential to reveal heterogeneities and changes in stress distribution within fault zones (*e.g., Allmann & Shearer, 2007; Chaves et al., 2020; Chen & Shearer, 2013; Moyer et al., 2018; Ruhl et al., 2017; Shearer et al., 2006a; Uchide et al., 2014*). However, different studies of the same region have resolved different spatial and temporal distributions; for example, the spatial pattern in Japan from (*Oth, 2013*) appears different from that by *Uchide et al., (2014)* and *Yoshida et al., (2017)*, who used more localized attenuation corrections. Some studies have also observed an increase in stress drop with depth that may reflect increasing stress on the faults, but such dependence may be, at least partially, an artifact of changes in attenuation and velocity with depth *(Allmann & Shearer, 2007; Sumy et al., 2017; Abercrombie et al., 2020)*. *Abercrombie (2014)* analyzed three repeating clusters of small earthquakes on the San Andreas Fault at Parkfield, and found the temporal changes of only one cluster (largest magnitudes) agreed with the results of *Allmann & Shearer (2007)* for the same earthquakes.

The variation in stress drop observed between different earthquakes could be due to real variation in the rupture processes, but the discrepancy among different studies indicates that random and systematic uncertainties are significantly distorting results; the differences between studies are often significantly larger than the calculated uncertainties (e.g., *Huang et al., 2017; Pennington et al., 2021*). The most likely causes of these problems are the simplifying assumptions required (concerning source geometry and attenuation structure), and the inherent ambiguities in separating source and path effects using seismograms with limited frequency range (e.g., *Abercrombie, 2021*). *Shearer et al. (2019)* and *Pennington et al. (2021)* both demonstrated that relative variability is more reliable than absolute values, and that consistency between different approaches provides confidence in the results.

To understand better the uncertainties in stress drop estimates, and improve the quality of the measurements, it requires detailed analyses of the effects caused by frequency bandwidth limits of the data, spatiotemporal variations of attenuation, and possible rupture velocity changes, among other things. As the problems became clearer, many studies have focused on reducing the scatter and improving the resolution of stress drop measurements, and quantifying more realistic uncertainty measurements using high-quality datasets and careful data processing. *Baltay et al. (2011)* showed that results using stacked Empirical Green's Functions (EGF) to correct for path and site effects had much lower standard deviation than previous studies; *Kwiatek et al., (2014)* found the stress drop scattering from EGF analysis is significantly reduced from fixed attenuation correction. *Chen & Abercrombie (2020)* used synthetic tests to develop an improved stacking approach and retrieved stress drop measurements with low standard deviation and reliable spatiotemporal patterns for an induced sequence in Oklahoma. *Shearer et al. (2019)* compared small earthquake corner frequencies estimated using a spectral ratio method (local EGF varying by earthquakes) and spectral decomposition method (a single global EGF for all the earthquakes), and found the spectral ratio corner frequencies are slightly larger than those from the spectral decomposition method. They also showed that the frequency range of the Southern California regional seismic network data is insufficient to resolve source scaling and absolute values of stress drop, and their variation, independently.

To investigate in more detail the relative effects of limited frequency range and assumptions about attenuation structure on stress drop measurements, we need an exceptionally well-recorded data set. The Parkfield segment of the San Andreas Fault in California has been densely instrumented for decades as a consequence of the Parkfield Earthquake Prediction Experiment (*Bakun & Lindh, 1985*), and the San Andreas Fault Observatory at Depth (SAFOD, *Zoback et al., 2011*). This instrumentation includes a borehole seismic network (*Malin et al., 1989*), that is able to record higher frequency signals than the surrounding surface networks. *Allmann & Shearer (2007)* performed a spectral-decomposition based study of earthquake stress drop in the region using the surface recordings. The occurrence of the 2004 M6 earthquake enabled them to look for temporal as well as spatial variation in stress drop. However, many of the earthquakes included in the analysis were relatively small (M<2) and hard to be well resolved due to station limitations. Here we use the higher-frequency borehole recordings to perform a similar analysis, and can investigate directly the effects of using the limited frequency range of the surface data. We are also able to include data for a further decade following the 2004 M6 earthquake than the earlier study.

The large body of previous work in the region provides us with context in which to interpret our results. The seismicity is well-located (e.g., *Waldhauser et al., 2004*), and includes sequences of near-identical, repeating sequences (*Nadeau & McEvilly,* *1999, 2004*). Analysis of variability in the moment and timing of these repeating earthquakes has revealed intriguing spatial and temporal variation in the stressing rate (e.g., *Chen et al., 2010; Lengliné & Marsan, 2009; Nadeau & Johnson, 1998*). Measurements of aseismic slip in the region have also revealed the gradual transition from creeping north-west of Middle Mountain to fully locked to the south-east of the HRSN, as well as temporal variations related to the 2004 M6 earthquake, and other events (e.g., *Murray & Langbein, 2006*). There have also been multiple studies of the coseismic and postseismic slip, and stress changes associated with the 2004 earthquake (e.g., *Dreger et al., 2005; Jiang et al., 2021*). The velocity structure (e.g., *Thurber et al., 2004*) and attenuation structure (e.g., *Abercrombie et al., 2000; Bennington et al., 2008*) are well known, and changes in both following the 2004 M6 earthquake have been observed (e.g., *Brenguier et al., 2008; Kelly et al., 2013; Sheng et al., 2021*). *Allmann & Shearer (2007)*, subsequently referred to as AS2007, found spatial variations in stress drop that did not obviously correlate with other parameters, and remained relatively stable, unaffected by the 2004 M6 earthquake. They also observed temporal changes in both stress drop and attenuation following the M6 earthquake, with different regions of decrease, and increase in each, but the temporal changes in stress drop were small compared to the spatial variation. Detailed studies of individual specific repeating sequences using the borehole recordings reported a decrease in stress drop followed by recovery for some sequences, but not others (e.g., *Abercrombie, 2014, 2021; Kim et al., 2016*), and also increases in attenuation and recovery on a similar time scale (*Kelly et al., 2013*). No large-scale analysis of the borehole recordings for earthquake source parameters has been performed to date.

We use borehole recordings and the spectral decomposition approach (*Shearer et al., 2006a; AS2007; Chen & Abercrombie, 2020*) to estimate stress drop for over four thousand earthquakes M0-4, from 2001-2016, in the San Andreas Fault zone at Parkfield. First, we investigate the effects of using different inversion methods, and allowing for spatial, depth, and temporal variation in attenuation and rupture velocity. We then compare the results obtained with different frequency ranges to quantify the effects of the limited bandwidth that is typically available for studies using surface recordings. Finally, we interpret our preferred results of spatial and temporal stress drop variation in the context of existing observations of the structure, and distribution of seismic and aseismic slip on the fault.

2.3 Data

We select our study area to be an 80 km section of the San Andreas Fault centered at the shallow-borehole High-Resolution Seismic Network (HRSN, *Karageorgi et al., 1992; Malin et al., 1989*). This includes parts of the ‘creeping zone’ to the northwest and the ‘locked zone’ to the southeast of Parkfield (*Harris & Segall, 1987; Murray & Langbein, 2006*). We download the triggered vertical-component waveforms at the 13 HRSN stations for all the earthquakes in the Northern California double-difference catalog (WNC catalog, *Waldhauser, 2009; Waldhauser & Schaff, 2008*), from Northern California Earthquake Data Center (NCEDC), see Figure 2.1). We include only earthquakes between 2001 and 2016 (the time of our download); the recording system was less consistent before 2001, with more frequent recording system changes and lower dynamic range (which caused clipping of large earthquake records). The waveforms have a sampling rate of 250 Hz and we apply the corrections for gain changes included in the instrument response table at the NCEDC. We use P wave phase picks in the NCEDC database, and use an STA/LTA based auto-picker (*Li & Peng, 2016*) to determine automatic picks for any waveforms without catalog arrival times.

We calculate the P-wave displacement spectra required for our analysis, using 1-second time windows, starting 0.1 s before the P wave arrival pick (see example in Figure S2.1). We compute the multi-taper spectral density and convert the recorded velocity spectra to displacement spectra. There is no need to correct for the instrument responses as these are included in the site terms in the spectral decomposition analysis. We also calculate the noise spectra using 1-second windows immediately preceding the signal windows, following the same approach. We select the earthquakes with sufficiently high-quality recording for the spectral analysis. We require an earthquake to be recorded by at least 5 stations, each with signal-to-noise ratio (SNR) higher than 10 at each frequency point between 2 and 60 Hz. The 4537 earthquakes between Mw0 and Mw4 that meet our data selection criteria are shown in Figure 2.1.

2.4 Theoretical Background and Spectral Decomposition Analysis Method

2.4.1 Spectral decomposition to obtain relative event source spectra

To measure the source parameters, we need to isolate the source contribution from the other effects within the recorded earthquake waveforms. An observed waveform (Figure S2.1) can be represented as the convolution:

$$S(t) = ET(t) * ST(t) * PT(t) \tag{2.1}$$

where, ET, ST and PT refer to the event term, site (or station) term and path term, respectively, all functions of time (*t*). Transforming Equation 2.1 to the frequency domain, and taking the logarithm converts the equation into a linear system that can be solved iteratively for ET, ST and PT as functions of frequency, following the Spectral Decomposition method developed by *Shearer et al., (2006a)* using a large number of earthquakes and stations:

$$S(f) = ET(f) + ST(f) + PT(f) + R(f) \qquad (2.2)$$

where $R(f)$ is a residual term from solution of overdetermined equations. Spectral decomposition only obtains the relative shape of the source spectra, however, and an additional correction is required to remove any site effects that are common to all events. After calculating the event spectra (*ET*(*f*), which can be considered relative source spectra), we follow *Shearer et al. (2006a)* to calculate the relative seismic moment of each event assuming it is proportional to their low frequency (2-4 Hz) amplitudes. To convert these relative moment estimates to actual moments and moment-magnitudes, we calculate their relationship with the catalog (*Waldhauser & Schaff, 2008*) local magnitudes. We observe a linear relationship for events with either ML≥1.40 or ML<=0.83, but an excess of events with ML~1 (Figure S2.2). We therefore exclude these ML~1 earthquakes from the calibration. We calculate the best fitting linear relationship for events with ML≥1.40 and ML<=0.83, and assume that ML = Mw when ML = 3.0 (*Shearer et al., 2006a; AS2007*) to derive moment estimates for all earthquakes in our dataset. The linear relationship has a slope of 0.92, consistent with previous studies of earthquakes in this magnitude range that typically find values of about 1 (e.g., *Abercrombie, 1996; Ben-Zion & Zhu, 2002; Hanks & Boore, 1984*), smaller than the 1.5 assumed for larger earthquakes in the original definition of Mw (*Kanamori, 1977*).

Estimating the actual source spectra from the event terms requires either an assumption of a reference site (e.g., *Bindi et al., 2020; Oth et al., 2011*), or a source model (*Shearer et al., 2006a*) to correct for higher frequency attenuation and amplification effects. We follow the approach of *Shearer et al. (2006a)*, calculating empirical correction spectra (ECS) to extract estimates of the absolute source spectra. The basic Spectral Decomposition approach also assumes a simplified attenuation structure in which $PT(t)$ depends only on the travel time. Any spatial variation in attenuation, including dependence on source depth (as observed by Bennington et al., 2008) is not included, and will be absorbed into the event term and bias the resulting source spectra (e.g., *Shearer et al., 2019; Abercrombie et al., 2020*). In other words, $ET(t)$ in equation 2.1 will include both the real source term and a function that includes common effects at all events and all sites, and source region specific attenuation. We investigate the effects of this assumption, and whether it is possible to address its effects by comparing a single ECS for the entire data set with separately calculated ECSs for different spatial source regions. Tomography models have shown strong spatial variations of material properties in the study region (e.g., *Bennington et al., 2008; Thurber et al., 2004; Thurber et al., 2006; Zeng & Thurber, 2019; Zhang et al., 2007*). We search for the most appropriate strategy that allows us to remove the influence of heterogeneous attenuation on stress drop estimations while maintaining an adequate number of events for stable stacking analysis.

2.4.2 Calculation of stress drop from earthquake source spectra

To calculate the source spectra, source parameters and the empirical correction spectra, we assume that the earthquake far-field displacement spectrum can be described by a Brune-type source model (*Brune, 1970*):

$$s(f) = \frac{\mathrm{M}_0}{1 + \left(\frac{f}{f_c}\right)^n} \tag{2.3}$$

where f_c is the corner frequency, and n is high-frequency fall-off rate, which we set to 2 (ω^{-2} model). Some studies have allowed the fall-off rate to vary, but found that it can tradeoff with the corner frequencies (e.g., *Shearer et al., 2019; Trugman & Shearer, 2017; Ye et al., 2013*) and so we choose to fix it here.

Assuming simple circular rupture, the corner frequency (f_c) can be used to calculate the source radius (*Brune, 1970; Madariaga, 1976*):

$$f_c = k\frac{\beta}{r} \tag{2.4}$$

where β represents the shear velocity, and k is a constant that depends on model assumptions, such as the source geometry, and rupture velocity (*Kaneko & Shearer, 2014, 2015*). We choose k=0.32 for P waves from *Madariaga (1976)*, which is consistent with AS2007, and *Kaneko & Shearer (2015)*. The dependence on β introduces a dependence on depth, since β is depth dependent. For example, if rupture velocity is assumed to be a constant fraction of β then depth varying velocity should be used. If a constant β is assumed in equation 2.4 for all depths, then this can also introduce an artificial dependence of source parameters on depth (e.g., *Allmann &*

Shearer, 2007).

The earthquake stress drop ($\Delta\sigma$) can then be calculated from the seismic moment (M_0) and the source radius (r) following *Eshelby (1957)*:

$$\Delta\sigma = \frac{7}{16}\left(\frac{M_0}{r^3}\right) = M_0\left(\frac{f_c}{0.42\beta}\right)^3 \tag{2.5}$$

The stress drop derived from spectral fitting must be considered an approximation. Theoretically it is related to the dynamic properties of the earthquake based on a circular rupture model assumption (*Brune 1970; Madariaga, 1976*), differing from the "static stress drop" derived from finite slip source parameters (e.g., *Noda et al., 2013*). In practice, it may be closer to a static stress drop since it is essentially the ratio of the slip to an approximation of the source dimension.

2.4.3 Stacking method to obtain an Empirical Correction Spectrum (ECS)

We use an adaptation of the stacking method developed and used by *Shearer et al. (2006a)* and AS2007 to invert the event spectra for a source model, source parameters and an empirical Correction Spectrum (ECS). *Shearer et al. (2006a)* stacked the event spectra into small Mw bins, and then inverted for a single ECS common to all events included in the stack and the best fitting stress drop common to all stacked Magnitude ranges, assuming the *Brune (1970)* source model. They also used the same approach to calculate an ECS for each event based on the 200 nearest neighbors, which involves variable spatial averaging due to the variability of the seismicity distribution; AS2007 used the latter approach. *Trugman & Shearer (2017)* also inverted for a common ECS, and allowed for a Mw dependence of stress drop. *Shearer et al. (2019)* showed that this

Mw dependence may not be resolvable with many data sets, finding strong trade-offs among the scaling factor, spectral fall-off rate, and reference stress drops.

Here, we follow a modified stacking approach proposed by *Chen & Abercrombie (2020)*, known as SNSS (Stacking-No-Self-Similarity assumption) to fit the stacked event spectra and solve for the ECS and mean stress drop. The SNSS approach does not include any assumption about stress drop scaling with magnitude, but inverts for the best fitting ECS common to all bins, while allowing the stress drop in each magnitude bin to vary independently. *Chen & Abercrombie (2020)* developed a series of synthetic experiments to validate the SNSS approach, and found that it performed better than the original stacking approach. They were unable to test approaches that simultaneously solve for scaling factors, because synthetic experiments indicated that their data set was too limited, with too much inter-event variability to resolve a scaling factor.

We calculate stacked spectra for each calibrated magnitude bin from Mw0.9 to Mw4.0 in increments of 0.3 M units of calibrated magnitudes. *Chen & Abercrombie (2020)* found that the SNSS approach can recover the true input stress drop when the corner frequency of the lowest magnitude bin is within 80% of the upper limit of the frequency range of the data. This implies that for the upper frequency limit of 60 Hz in this study, the lowest magnitude bin should have a corner frequency of 48 Hz or lower for unbiased stress drop estimation. Assuming the average stress drop of about 6 MPa determined by AS2007, the estimated corner frequency of Mw=0.9 (the smallest magnitude bin that is well recorded) would be 75 Hz, Mw=1.2 would be 53 Hz, and Mw=1.5 would be 38 Hz; thus the corner frequency of the Mw0.9 bin, is too high to constrain in the inversion. Based on these estimations, we combine the SNSS and the fixed-stress drop approach in *Baltay et al. (2010)* to develop a hybrid-adaptive approach that enables us to include the large number of earthquakes in the Mw0.9 bin, but constrain the inversion with larger Mw events. We first apply the SNSS approach to magnitude bins with Mw≥1.5 to obtain the best-fitting reference stress drops for the Mw1.5 bin. Then we fit the stacked event spectra in the Mw0.9 bin fixing the stress drop to the value we obtain for the Mw1.5 bin, to calculate an ECS following *Baltay et al., (2010)*. We refer to this modified approach as the Self-Adaptive SNSS method (but still abbreviate it as SNSS in this study for simplification). This hybrid approach has the advantage of obtaining unbiased stress drop values that are specific to the dataset, instead of an assumed global average value as in *Baltay et al. (2010)*, while also including solutions for small earthquakes and estimation of ECS from the magnitude bin with most abundant earthquakes.

To calculate actual source parameters, each individual event spectrum is corrected using the common ECS determined from the SNSS inversion, and then fit using the selected source model and assumed constants. We perform a comparison of the original method of *Chen & Abercrombie (2020)* with our new hybrid SNSS method using a spatially compact dataset with 220 earthquakes, and find generally consistent results. The new method leads to lower magnitude scaling (Figure 2.2), as a consequence of the different ECS in the two methods, most likely representing the well-known increasing uncertainties and trade-offs as the corner frequency approach the limits of the frequency range of the recorded signal (e.g., *Abercrombie, 2015; Ruhl et al., 2017*). but there is no solid evidence of how the change compares to the magnitude scaling due to frequency band limitation, or if lower magnitude scaling means more accurate stress drop estimation.

2.5 Spectral Analysis of the Parkfield dataset

To investigate the effects of different assumptions about source model, and spatial and temporal variation in path effects (and ECS), we perform a sequence of independent inversions. All of these start from the event spectra calculated in the single spectral decomposition inversion of the entire dataset. We first investigate the effects of spatial binning only, using the entire data set, and then separate the earthquakes into 3 time intervals related to the 2004 M6 earthquake to investigate temporal variation. In the following sections, we will define multiple strategies to organize data and select parameters, see Table 2.1 for references.

2.5.1 Initial single bin inversion (Strategy 1)

First, we perform a single inversion of all the event spectra to solve for stress drops for all individual earthquakes in our dataset. We use the hybrid SNSS approach to calculate a single ECS to correct for the source spectra of all the earthquakes (no consideration of spatial varying attenuation), and use a constant shear wave velocity (assuming constant rupture velocity) to compute stress drops from corner frequencies and moments with Equation 2.4 (Figure 2.3).

To quantify any dependence of stress drop on moment, we calculate the median stress drop in overlapping Mw bins of 1 Mw unit width centered at 0.5 unit intervals. We then use linear regression to find the best fitting trend and R-squared value (squared correlation coefficient) in two separate intervals with a relatively large number of events: (i) Mw0.75-1.75, in which stress drop increases with moment, and (ii) Mw1.75-2.75, in which there is negligible dependence of stress drop with moment, see Table 2.2 and Figures 2.3B and S2.6.

We use a similar approach to quantify any dependence of stress drop on depth, by calculating the median stress drop in 1 km depth intervals. The results of the single inversion with no correction for depth-dependent velocity or attenuation indicate an increase in stress drop with depth, both between 1.5 and 6.5 km, and between 6.5 and 11.5 km (Table 2.2 and Figure 2.3A).

2.5.2 Spatial Variation: With Depth and Along Strike

2.5.2.1 Single bin, constant Vs or variable Vs? (Strategy 2)

To investigate the effects of allowing for a depth-varying rupture velocity, proportional to the shear wave velocity, we compute stress drop using the same corner frequencies from the single inversion (Strategy 1), but use the shear wave velocity from the 1D velocity model (Figure S2.3) used by AS2007, based on the *Thurber et al. (2004)*. Table 2.2 and Figure 2.3 show that the magnitude dependence is slightly weaker between Mw0.75 and Mw1.75, and the depth dependence is significantly weaker than when no depth dependence to velocity was included (Strategy 1), demonstrating the importance of velocity correction in stress drop estimations. We do not apply any lateral velocity correction because of the significantly smaller velocity variation along strike than with depth *(Thurber et al. 2004)*. Also, because our event terms are obtained from all stations, on both sides of the fault, we cannot easily consider the velocity differences across the fault. To do so would require separate spectral decomposition for the stations on each side of the fault (for which we have insufficient stations and earthquakes), and so we simply use an average velocity structure with depth here.

2.5.2.2 Effect of Depth Bins, Constant Vs and Variable Vs (Strategies 3 and 4).

To investigate the effects of allowing the ECS to vary with depth, and account for possible variation in attenuation with depth, we divide the dataset into four depth bins (1-4, 4-5, 5-8 and 8-15km) guided by the velocity structure (Figure S2.3) and earthquake distribution, ensuring sufficient earthquakes within each bin for a stable inversion. We repeat the analysis both assuming a constant shear wave (and rupture) velocity (Strategy 3) and allowing shear wave velocity to vary with depth (Strategy 4). The results are compared to those in the previous inversions in Figure 2.4 and Table 2.2.

At shallower depth, the depth-dependence of stress drop is significantly reduced by using variable β (slope reduces by 60% comparing Strategy 3 and 4), but only slightly reduced with only depth-dependent attenuation (slope only reduces by 22% comparing Strategy 1 and 3). However, at deeper depth, the depth-dependent attenuation correction has significant impact on the depth-dependence of stress drop (slope reduction of 85% between Strategy 1 and 3). Slopes of magnitude dependence are also reduced, albeit slightly.

2.5.2.3 Effect of Spatial Bins, Constant Vs or Variable Vs (Strategies 5 and 6).

To determine a reasonable along-strike spatial bin size to use, we first perform a simple test to compare results of increasing sized spatial bins. Smaller bins allow for greater resolution of spatial variability, and are closer to the assumptions of the underlying EGF approach (e.g., *Abercrombie, 2015*), but in the stacking approach, it is the large number of earthquakes included (e.g., at least 200 as used in AS2007) that provides stability. If the spatial bin size is too small, the number of events will be inadequate to obtain a stable ECS; if the bin size is too big, the spatial variation in ECS will be insufficient to account for heterogeneity.

We select 3 different bin sizes (1x1 km^2, 5x1 km^2 and 10x1 km^2, along-strike between 20 and 30 km, and at 4-5 km depth) from a part of the fault with sufficient earthquakes for stable inversion (Figure 2.4). We use a narrow depth range to minimize the effects of depth dependence in this test. The three bins include 350, 1100, and 1400 earthquakes respectively, and the smaller bins are subsets of the larger bins. We solve for ECS and source parameters within each bin separately, and then compare the results for common events (that is, the 350 events in the 1km bin).

We find that the ECSs from the three spatial bins are almost identical with only minor deviations from the 1 km bin (Figure 2.4), and the corner frequencies and stress drops are nearly identical for the common earthquakes from bins with different sizes. Only minor deviations occur when the corner frequency approaches or exceeds the frequency limit of the data. This comparison suggests that ECS can be assumed to be constant within a 10 km along-strike bin size to resolve earthquake source parameters. This 10 km bin size is large enough that there are enough earthquakes in most bins to apply the stacking analysis with both along strike and depth varying ECS.

Based on this test, we adopt the following preferred spatial binning strategy:

(1) split the 80km long along-strike fault section into 8 along-strike bins of 10 km;

(2) split the along-strike bins into 1-4, 4-5, 5-8 and 8-15km depth bins (i.e., the same as depth ranges used in Strategies 3 and 4, Section 2.3.2.2);

(3) only invert spatial bins containing at least 200 events to guarantee enough earthquakes above Mw>0.9 (Figure S2.4).

We also compare the performance of the original SNSS in *Chen & Abercrombie (2020)* with the new hybrid SNSS in Figure S2.5. We repeat the analysis both assuming a constant shear wave (and rupture) velocity (Strategy 5) and allowing shear wave velocity (β) to vary with depth (Strategy 6). The results are compared to those in the previous inversions. We note that the spatial bins further reduce the magnitude dependence between Mw0.75 and Mw1.75 with slopes reduced to 0.384 and 0.354 with constant and variable β, respectively (Table 2.2). The depth dependence does not change significantly compared to simple 1-dimensional depth binning (Strategies 3 and 4).

2.5.2.4 Summary of effects of spatial attenuation and velocity corrections in stress drop calculation

Figure 2.3 compares the results of our inversions to investigate the effects of spatial binning (with depth and along-strike) and varying rupture velocity on the separation of source and path effects in the Parkfield region. The relatively wide frequency range of the borehole data compared to previous spectral decomposition studies provides improved resolution of source from the path and site effects. Figure 2.5 shows the distribution of stress drops obtained using each strategy. Not surprisingly, the largest effects are on the depth dependence of the resulting stress drop estimates, but the magnitude dependence is also affected.

Including a depth-dependent attenuation correction (Strategy 3, depth binning) significantly reduces both the magnitude and depth dependence, and the standard deviation of the resulting stress drops (Figure 2.5) compared to Strategy 1. The finer scale lateral binning of Strategy 5 (10 km along-strike binning) only slightly reduces the dependence and standard deviation of Strategy 3 (no along-strike binning), suggesting that along-strike variation in attenuation is less significant that with depth in the study area.

The comparisons between Strategies 6 and 5, between 4 and 3, as well as between 2 and 1, show that velocity correction also significantly reduces the dependence of the calculated stress drops on both magnitude and depth.

The variation in velocity has more effect at shallow depths, where the velocity is increasing rapidly with depth, than deeper, where it is changing more slowly. Conversely, the ECS correction has a larger effect at greater depths, implying that the difference in path effects continues to be significant in this depth range.

The ECS attenuation correction and velocity corrections also have different effects on the magnitude and depth dependence of stress drops. From Table 2.2 and Figure 2.4, magnitude dependence is more significantly reduced by improved attenuation corrections than depth-dependent velocity correction, while for depth dependence, the influence of velocity correction is more significant. AS2007 also found that depth dependence in stress drop is sensitive to the assumed velocity structure, and did not resolve any significant increase in stress drop with depth. They also found no dependence of stress drop on magnitude in a similar range to this study.

Figure 2.6 compares the empirical correction spectra (ECS) obtained, showing greater variability with depth than along strike, consistent with the effects on stress drop. These spatial-bin specific ECS correct for site effects common to all events. They also attempt to correct for the difference between the average regional travel-time dependent path terms from the original spectral decomposition, and the real, along path attenuation that depends on the individual source and station locations. It is hard to interpret the ECS in terms of absolute attenuation, but their differences do provide quantitative information about the variability in attenuation for earthquakes in different source locations. We fit the slopes of ECS spectra between 20 and 60 Hz, following *Anderson & Hough (1984)*, to quantify the variability of t* in different depth ranges, and along strike (Figure 2.6). t* describes the total attenuation over travel path between source and station, and is defined as (*Scherbaum, 1990*):

$$t^* = \int_P \big(u(l)/Q(l)\big)\, dl \tag{2.6}$$

where *P* represents the ray path, *u(l)* is the slowness over the path, and *Q(l)* is the quality factor over the path).

As we apply increased correction for spatial variation of velocity and attenuation, the standard deviations progressively decrease from 0.66 for Strategy 1 to 0.41 for Strategy 6 (Figure 2.5a), implying that the variability in stress drop in an earthquake population strongly depends on data processing, and trades-off with attenuation and velocity corrections. Meanwhile, we calculate the root mean square (RMS) of the misfits between ECS and individual source spectra by frequency sample for Strategy 2, 4 and 6, and find that the median RMS of misfits from the 3 strategies synchronizes with the drop of stress drop standard deviations, which suggests that the proposed corrections may lead to better spectral fitting; however, by introducing the corrections we also introduce more free parameters that trade-off with the misfits.

2.5.3 Temporal attenuation correction

The 2004 M6 earthquake caused temporal changes in both the velocity and attenuation structure at Parkfield (*Kelly et al., 2013; Brenguier et al. 2008; Sheng et al., 2021*). To investigate any temporal variation in stress drop, we need to ensure that we are not just misinterpreting temporal variation in attenuation and other path and site effects. Hence, following AS2007 and *Abercrombie et al. (2020)*, we divide the dataset into distinct time periods and calculate separate inversions for each. To balance the number of earthquakes needed for stable inversion, and the temporal dependence of the observed changes, we divide our dataset into three time periods (Figure S2.6): (1) before 2004 M6 earthquake; (2) one year following the M6 earthquake (Sep. 2004 - Sep. 2005), the approximate duration of significant attenuation and velocity changes; (3) after September 2005. We then repeat the first four different strategies used in our analysis of spatial variation. We refer to them using the same numbering, with the additional note of being temporally corrected. The first time period, before the M6 2004 earthquake has the fewest earthquakes, and so the ECS and resulting source parameters for all spatial bins in this time interval are consequently the least well resolved (Figure S2.7). We do not make any temporal corrections for changes in velocity because they are too small (~0.25%, *Brenguier et al., 2008; Sheng et al., 2021*) to have any significant effect within our resolution and uncertainties.

There are insufficient earthquakes to divide them both along strike and into different temporal ranges for Strategies 5 and 6. We take advantage of the coherent ECSs for spatial bins of the same depth range, and adopt a hybrid-approach to combine temporal corrections and the finer-scale spatial binning for Strategies 5 and 6. First we calculate the difference between the ECS in different time periods in each depth bin, then apply these relative temporal differences to the respective ECS for the spatial bins calculated for the entire time period (Section 2.5.2.3) to obtain "pseudo-" temporal ECSs for each grid during each time period. Finally, we solve for the source parameters for each earthquake using the corresponding ECS based on occurrence time and location. We refer to these, our preferred, parameters as Strategy 6, with temporal correction.

Figure 2.5 shows the minimal effect of the temporal attenuation correction on the distribution of stress drops obtained using the different strategies. We suspect this is partly related to the increased uncertainty in the inversions, due to the smaller numbers of events in each one, offsets the increased number of free parameters. The inversions with and without temporal binning have very similar median stress drops, and reveal similar behavior of stress drop with respect to depth and magnitude (Table 1 and Figure S2.7).

Figure S2.8 shows the ECS changes for each depth bin for the three time periods, with higher amplitudes of ECS indicating lower attenuation (see supplementary text S1). We quantify the relative change in attenuation with time following the approach mentioned above. From Pre-2004 to 2004-2005, the overall ECS amplitude decreases slightly for 1-4 km (t* increase of 0.05ms) and more significantly for 4-5 km, 5-8 km and 8-15 km (t* increases of 1.75ms, 0.84ms and 0.75ms, respectively). From 2004-2005 to Post-2005, we see the reverse behavior, with the overall ECS amplitude increasing and t* decreasing by 0.18ms (1-4 km), 0.30ms (4-5 km), 1.20ms (5-8 km) and 0.32ms (8-15 km). The t* variations suggest increased attenuation immediately following the 2004 M6 earthquake, and gradual recovery over long term, which is consistent with previous studies of attenuation changes (e.g., *Kelly et al., 2013*). Figure S2.9 shows individual event corner frequencies before and after temporal correction have an average ratio of 1.011 with standard deviation of 0.34, suggesting the influence of temporal correction is relatively small.

2.6 Results and Discussion

We calculate stress drop for earthquakes at Parkfield using a variety of different approaches to correct for spatially and temporally varying material properties, in an attempt to resolve the real spatial and temporal variation in earthquake sources. We use the shallow borehole (HRSN) recordings, and only include earthquakes recorded by at least 5 stations with high signal to noise ratio over the frequency range 2-60 Hz; this is a relatively wide frequency range compared to many previous spectral-decomposition studies (e.g., AS2007; *Trugman, 2020; Trugman & Shearer, 2017*). We apply the self-adaptive SNSS method, that does not assume any magnitude scaling, to calculate the empirical correction spectra (ECS) and isolate the source spectra. We compare our results to those of recent studies of stress drop at Parkfield including the large-scale study of AS2007 and the smaller scale analysis of *Abercrombie (2014)*. We begin by discussing the trends, resolution and uncertainties in the data set as a whole, and then consider the spatio-temporal patterns and their reliability.

2.6.1 Separation and resolution of source and path effects

Perhaps the most challenging problem with obtaining earthquake source parameters is to separate the source from the path and site effects. We apply a series of data processing strategies to improve the robustness of stress drop estimation. Our resolution benefits from the relatively low noise, and wider bandwidth of the borehole stations compared to the previous similar style analysis by AS2007. This can be seen in the lower standard deviation for stress drop variability we obtain for each of our Strategies, compared to the earlier study by AS2007 (Figure 2.5). We find that the assumptions and choices involved in both the attenuation and velocity corrections can lead to apparent magnitude or depth dependence (Figure 2.3). The final strategy that includes both factors results in the least stress drop dependence and the lowest standard deviation of stress drop variability. AS2007 used a spatially varying ECS, with the spatial smoothing depending on the local density of seismicity, and also found no resolvable magnitude or depth dependence to their stress drop values. As in most previous studies of stress drop, we observe that the standard deviation gradually increases with decreasing magnitudes. The standard deviation increases from <0.1 (for Mw≥2.8) to 0.24 (for Mw≤1), but, even the smallest magnitude bin in this study has lower standard deviation than the largest magnitude bin in AS2007, implying a more well-constrained inversion and better parameter resolution (Figure 2.8). This confirms that a borehole network with higher bandwidth, lower noise, and less attenuated signals can retrieve better measurements of source parameters for small earthquakes.

The standard deviation in stress drop in the entire data set decreases significantly with increasing allowance for depth dependence of attenuation and rupture velocity, implying that these factors contribute to the apparent variability of stress drop. Comparison of the empirical correction spectra shows decreasing attenuation with depth, consistent with the increase in velocity and Q with depth previously observed in the region (e.g., *Thurber et al., 2004; Bennington et al., 2008*). These previous analyses also find that the along strike variation is less than that with depth, again consistent with our results. Unfortunately, because the spectral decomposition approach combines stations from all azimuths and distances, we cannot investigate any difference in attenuation across the fault.

2.6.2 Implications for stress drop scaling with depth and magnitude

Previous work has shown that the limited frequency range of the earthquake spectra available for modeling can significantly bias the resulting estimates of corner frequency. For example, *Shearer et al. (2019)* showed that the frequency bandwidth of regional Southern California Seismic Network data (~2-20 Hz) is inadequate to distinguish between different source models and scaling, and *Abercrombie (2015)* showed how decreasing frequency range biased the results in empirical Green's function analysis. Here our relatively wide frequency range (2-60 Hz), larger than almost all previous spectral decomposition studies provide increased resolution.

To further explore the influence of the frequency band on corner frequency estimations, and guide our interpretation of our new results, we repeat our analysis limiting the frequency range to first, 2-20 Hz and second, 2-40Hz. Figure 2.7 (a, b) shows that corner frequencies calculated with a narrower frequency band are much more scattered than those with a wider frequency band, especially when the corner frequency exceeds the upper limits. In addition, higher corner frequencies are systematically underestimated when using a lower maximum data frequency (Figure 2.7c). Previous work using an empirical Green's function approach by Abercrombie (2015), *Abercrombie et al. (2017)* and *Ruhl et al. (2017)* found that systematic low bias in corner frequency estimates starts at a half or two thirds of the maximum frequency of the data. *Chen & Abercrombie (2020)* found similar results using spectral decomposition, although their synthetic tests suggested that sometimes corner frequencies of 80% the maximum frequency could be resolved using the SNSS approach. In Figure S2.5 we show that our new hybrid SNSS approach somewhat mitigates the problem compared to the original SNSS approach in *Chen & Abercrombie (2020)*; in the hybrid approach the smallest magnitude bin has stress drop derived from the largest magnitude bins that are used to calculate the empirical correction spectra. We still observe increased variability at smaller magnitudes, probably largely reflecting increased uncertainties, but we see less systematic bias.

AS2007 used surface stations and a narrower frequency range in their analysis, the narrower frequency range being a direct consequence of the near-surface attenuation and higher noise in the surface recordings. It is likely that the lower frequency bandwidth is causing the higher standard deviation and the lower median values reported by AS2007, compared to the current analysis (Figure 2.5 and 2.7). Figure 2.7d shows a constant shift of approximately a factor of 1.2 when compared to our preferred, full bandwidth results. This translates to approximately 1.7 times (1.2^3) difference in stress drop, consistent with the difference of the median stress drop values in these two studies; we obtain ~10MPa for the borehole dataset, while AS2007 report ~6MPa using similar constants in equation 2.5. In Figure 2.7c we see that the AS2007 corner frequencies are lower than those from our analysis using the same (2-20 Hz) frequency range. This suggests that the more attenuated surface data may tend to underestimate the stress drop during the ECS calculation, although the random uncertainties are also large from such a limited range (e.g., *Shearer et al., 2019*).

In all analyses shown in Figure 2.7, some events with corner frequencies near the limits of the data can be very high, or low. This is possibly due to a combination of the effects of limited bandwidth with complexity in the earthquake sources themselves, that is ignored in the simple spectra fitting. *Abercrombie (2021)* demonstrates how this can bias the results, especially for particularly complex events, and *Yoshimitsu et al. (2019)* also note how the inappropriateness of the simple Brune source model individual earthquakes greatly increases the uncertainties of stress drop estimates.

Given the above discussion, Mw1.5 is the lowest magnitude for which we should be able to resolve corner frequency without bias using our approach, given the maximum signal frequency of 60 Hz and a reference stress drop of 10 MPa. In practice, we find that the median stress drop of the M>1.1 earthquakes (median $\log_{10}(\Delta\sigma) = 1.24$) is not significantly different from that of the M>1.5 events (median $\log_{10}(\Delta\sigma) =$

1.32), given the standard deviation of the whole data set (0.43). We also compare the spatiotemporal variations of stress drop with different magnitude cutoffs in Figure S2.10, and find that patterns with M>1.1 are similar to higher magnitude cutoffs, therefore, we include earthquakes with M>1.1 in our interpretations.

2.6.3 Frequency range and magnitude range of reliable parameters

We find that including reasonable corrections for depth dependent attenuation and rupture velocity can remove all need for any systematic dependence of stress drop on source depth in the upper 15 km at Parkfield. This is consistent with the previous results of. It is also in agreement with a recent meta-analysis (*Abercrombie et al., 2020*) that showed that previously reported increases in stress drop with depth could be artifacts of inadequate correction for depth dependent path effects.

Less intuitively, improving corrections for depth variation in attenuation and velocity also decreased the resulting magnitude dependence of the stress drop results. The magnitude dependence is weak to the point of negligible above M1.75, but at lower magnitudes, some increase in stress drop with magnitude remains, regardless of correction strategy (see Figures 2.3, S2.6 and Table 1). We also observe increased variability at smaller magnitudes (Figure 2.8), probably largely reflecting increasing uncertainties. Based on previous analysis of the effects of frequency bandwidth limitations (e.g., *Abercrombie, 2021*) and our own analysis discussed above, we interpret this is a resolution effect, rather than a real physical effect.

2.6.4 Spatiotemporal variability of stress drop and the effects of the 2004 M6 Earthquake

Figure 2.9 shows the stress drop spatial variations in 3 time periods: 1) Mar 2001 – Sep 2004, 2) Sep 2004 – Sep 2005, and 3) Sep 2005 – Aug 2016, projected onto the San Andreas Fault. We smooth the distribution by dividing the study area into 4 km (along strike) by 2 km (along depth) grids, and obtain the median stress drop for grids with more than 5 earthquakes. Here we use the results for Strategy 6 (including corrections for both spatial and temporal attenuation, and depth-dependent velocity) and use earthquakes with M>1.1. The relatively small number of earthquakes in time period 1 (before the 2004 M6 earthquake) limits the spatial resolution in that time period. We also calculate a comparable figure using the results of Strategy 6, without temporal variation (Figure S2.11) and observe very similar patterns, suggesting that the results are not significantly affected by uncertainties in the temporal corrections.

From Figure 2.9, we observe considerable small-scale heterogeneity, but general stability and consistency over the entire time period. AS2007 also observed no significant change in the spatial distribution before and after the 2004 M6 earthquake. We infer this to indicate that the spatial variability in fault conditions is significantly larger than any temporal effects caused by the coseismic or postseismic slip. Similar spatial stability was reported by *Ruhl et al. (2017)* for the well recorded Mogul earthquake sequence in Nevada, as well as *Uchide et al. (2014)* for M3.0-4.5 earthquakes in the 2011 Tohoku earthquake area, suggesting structural or material heterogeneity is the dominant factor of stress drop variability. This is also consistent with the constant rupture directivity of sequences at Parkfield analyzed by *Abercrombie et al. (2020)*, but contrasts with similar-sized spatial and temporal variation associated an M6 earthquake on the Gofar transform fault, reported by *Moyer et al. (2018)*.

Also in Figure 2.9, we observe no clear difference between the stress drop distribution in the locked and creeping parts of the fault. Inversions by *Murray & Langbein (2006)* indicate that above about 15 km depth, NW of the 1966 hypocenter, the fault is essentially creeping throughout this time period, and to the SE it is primarily locked, slipping seismically and post-seismically in 2004 to 2005. This division is not visible in Figure 2.9, suggesting that the stress drops of small earthquakes are not primarily affected by the nature of slip on the surrounding fault at large scale. These results contrast with the reported along-strike variation in stress drop of earthquakes on the Gofar oceanic transform associated with different levels of inferred seismic and aseismic slip (*Moyer et al., 2018*). With only two examples, we cannot draw any reliable conclusions as to why the faults may behave (or only appear to behave) differently.

We compare our observations of spatially varying stress drop to the various finite-fault inversions of the 2004 M6 earthquake (*Dreger et al. 2005, Custódio et al., 2005*), but again see no clear correlation. This is partly because of variability in the different inversions which do not have resolution on the scale of the spatial heterogeneity we observe, but we see strong variation in stress drop even in regions with high slip in most models (e.g., between the 1966 hypocenter and SAFOD). Combining GPS data and seismicity, *Jiang et al. (2021)* observed that the evolution of spatial distribution of slip after the mainshock is different at different time scales, suggesting afterslip rate and local structure controls fine-scale seismicity behaviors.

At smaller scale, we observe considerable variability, that shows some consistency and some variation from the earlier results of AS2007. Their study included more earthquakes before the 2004 M6, but also is likely to have larger uncertainties because of the lower quality of their data. The high level of small-scale heterogeneity is consistent with the observations of the behavior of repeating sequences by *Lengline and Marsan (2009)*. It does not show any clear dependence on other known characteristics of the fault zone. For example, we observe regions of high and low stress drop around the hypocenters of both the 1966 and the 2004 earthquakes.

The temporal variations we observe in both attenuation and stress drop are relatively small compared to the spatial variations. Figure S2.8 shows the differences in attenuation in different depth and time periods. Figure 2.10 compares our observed temporal variation in stress drop, in the different time periods, to that reported by AS2007. Because of the shorter time span of AS2007 after the 2004 earthquake, we only compare the temporal changes between period 2 and period 1. For each grid used in Figure 2.9, we calculate the difference in average stress drop values between successive time periods (i.e., Period 2 - Period 1, and Period 3 - Period 2). Again, we use all earthquakes M>1.1; we obtain consistent results with a magnitude cut-off of 1.1 or larger (Figure S2.10). Like AS2007, we observe regions of increase and decrease in stress drop following the 2004 M6 earthquake. The region of high slip in the M6 earthquake (according to *Dreger et al., 2005*) encompasses stable patches of high and low stress drop.

The increase in absolute values of attenuation at shallow depths (< 4 km), obtained here following the 2004 M6 earthquake, are almost a factor of ten smaller than those calculated from repeating earthquakes in the same depth range by *Kelly et al. (2013)*. This may represent a combination of temporal averaging, and smoothing of small-scale heterogeneous behavior in our larger-scale analysis, or result from the uncertainties in either or both studies. Unlike *Kelly et al. (2013)*, we observe larger temporal variation in attenuation at greater depths (5-8 km). This also contrasts with the conclusion that the larger velocity changes (~0.25%) are limited to the upper 1-2 km (*Sheng et al., 2021; Wu et al., 2016*). We observe a decrease in attenuation from 2005 to 2016, that is about 1/2 to 2/3 times that of the increase following the 2004 M6 earthquake. This asymmetry may indicate incomplete recovery, or simply reflect the uncertainties. *Malagnini et al. (2019)* investigated temporal and spatial changes in attenuation at Parkfield using coda waves, and reported variation on a range of time scales. They found that the 2004 M6 earthquake affected the attenuation variation on the NE and SW sides of the San Andreas Fault very differently. Our analysis averages the behavior of both sides of the fault.

Clearly, fully separating temporal variation in stress drop and attenuation remains a challenge, and we take this into account as we attempt to interpret out results. To discuss the complex patterns, we observe and their resolution, we focus on four regions indicated on Figure 2.9 and 2.10. Ideally, we would use smaller regions, guided by the spatial variation, but they contain insufficient earthquakes to make reliable conclusions. We therefore choose regions thought to represent different conditions and behaviors, and explore the stress drop variations within.

Region I: SAFOD Region. We start by discussing the shallow region surrounding SAFOD as it includes repeating sequences of well-studied earthquakes that we can use to assist in assessing the reliability of our results. It is a region of fairly average stress drop values in our analysis (Figure 2.9). *Abercrombie (2014)* used an individual-event based spectral-ratio approach to obtain corner frequencies, and for earthquakes in the three sequences of earthquakes targeted by SAFOD. For the largest magnitude sequence (T1, M~2.1) the simple circular source model was a good approximation, and *Abercrombie (2014)* found good agreement with the results of AS2007 for the same events; both studies found that the immediately after the 2004 M6 earthquake had significantly lower stress drops than the other events. Time domain source modeling, also using empirical Green's functions, by *Dreger et al. (2005)*, and *Kim et al. (2016)* also revealed a similar relative temporal behavior for the same earthquake sequence. Sequence T2 involved complex sources and was not well modeled by Abercrombie (2014). Sequence T3 is too small to be resolved in the study of AS2007, but *Abercrombie (2014)* observed similar decrease in stress drop for events in this sequence immediately following the 2004 M6 event, albeit with larger uncertainties. In Figure 2.11, we compare our results to those of *Abercrombie (2014)* for the same earthquakes. We see better agreement for the lower frequency measurements, but at higher corner frequencies the results of *Abercrombie (2014)* are systematically higher. This could be due to *Abercrombie (2014)* using a higher upper frequency limit for these well-recorded earthquakes (~90 Hz) or else may be method dependent (see *Shearer et al., 2019;*

Abercrombie, 2021). *Pennington et al. (2021)* performed a comprehensive comparison of methods to estimate stress drop for earthquakes in the Prague, OK, 2011 sequence, and found that although the absolute values varied considerably, there was good agreement between the relatively low and high stress drop populations among the different methods and independent studies. For the better-quality results of *Abercrombie (2014)* in Sequences T1 and T3, we observe that both studies have relatively low corner frequencies for the events immediately after the 2004 M6, compared to the other events. This comparison gives us some confidence that we are observing real temporal variation. It is still possible that very localized, short-term variation in attenuation is causing similar apparent variation in source parameters in all the studies. Certainly, the earthquake seismograms recorded shortly after the M6 event have relatively low high-frequency energy. The fact that in our work, and that of *Abercrombie (2014)* and *Abercrombie et al. (2020)*, some temporal stress drop variation remains regardless of the various attenuation corrections tried, suggests that at least some of the variation in source parameters is real.

Figure 2.10 shows on average a small increase in stress drop in the region around SAFOD, in the year after the M6 earthquake, followed by a small decrease. Figure 2.10, B1 shows the high level of variability and the changes within the one-year period we average for our Time 2. The variability implies that identifying more significant variations would require smaller scale spatial and temporal resolution than is available.

Region II: Aseismic Creep Region. This region is of interest as it is in the part of the fault thought to be almost entirely slipping aseismically (e.g., *Murray & Langbein,* *2006*). In our analysis, it is characterized by relatively high values, but they are no higher than those around the 2004 hypocenter, and the creeping region nearer to SAFOD has lower values, negating a simple relation between high stress drop and creep (Figure 2.9). AS2007 observed an apparent increase in stress drop in this region, following the M6 but did not have sufficient earthquakes to resolve it. The region is just outside the HRSN network, but we observe a decrease in stress drop following the M6, and an increase afterwards. Again, these are very small trends amidst much variability (Figure 2.10, B2).

Region III: 1966 Hypocentral Region. This region, also known as the Middle Mountain asperity, also shows variable behavior with patches of relatively high and low stress drop. Unfortunately, the lack of events in these individual smaller regions in all time periods means that we cannot resolve time variation on this scale. The region is dominated by a decrease in stress drop (Figure 2.10, B3) immediately following the 2004 M6 earthquake, and then returns to normal within the year. The immediate decrease of stress drop is consistent with observations from other large earthquakes, for example, the M5.7 Prague earthquake (*Yenier et al., 2017*). In fact, some high stress drop events in the region near the end of time period 2 increase the average and lead to an apparent decrease in stress drop in the following time period (compare Figure 2.10, B3 with Figures 2.10, A2 and A3). In this region, *Abercrombie et al. (2020)* and *McLaskey et al. (2012)* observed one relatively well-recorded sequence to exhibit a possible decrease then gradual increase in stress drop. South of the 1966 hypocenter in this region, *Jiang et al. (2021)* observed significant coseismic slip and afterslip about 8 hours following the 2004 earthquake, which coincide with an area of stress drop increase (Figure 2.10, A2), suggesting possible influence of fault slip on stress drop changes.

Region IV: 2004 Hypocentral Region. Like the hypocentral region of the 1966 earthquake, this region shows some strong spatial variation and less clear temporal variation, with opposite changes to AS2007 (Figures 2.10, A1 and A2). This is largely because of the lack of events prior to the M6 earthquake. Figures 2.10, A2, A3 and B4 suggest that the region is dominated by a decrease in stress drop immediately following the M6, and then gradual recovery. This region experienced complex slip history with coseismic slip and afterslip featuring slip reversals and slip pulses (area R1 in *Jiang et al., 2021*). These complex stress changes complicate the interpretation of stress drop variations in this region.

Overall, in region I, which is located at the shallow portion of cosesimic slip zone, we observe less coherent temporal changes in relation with the 2004 M6 earthquakes, however, individual repeating sequences exhibit robust stress drop decrease after the 2004 event. In region II, where no significant coseismic and post-seismic slip has been reported, we observe small trend with large variability. In region III, where both significant seismic and postseismic slip are observed, clear temporal variation of stress drop is observed. Temporal variation of region IV is less resolved due to limited number of earthquakes prior to the 2004 earthquake. Observations in regions I and III suggest that fault slip influence spatiotemporal distributions of stress drop. However, amplitudes of temporal stress drop changes are relatively small compared to background stress drop spatial distributions, indicating that local fault structure is likely the major cause of spatial heterogeneity.

2.7 Conclusions

We use shallow borehole recordings of 4537 earthquakes at Parkfield, California, to investigate resolution scaling, and spatio-temporal variation. We find:

1. Correction for spatio-temporal variation in material properties is needed to improve the accuracy of stress drop estimations. In Parkfield region, corrections of along-depth attenuation and along-depth rupture velocity variations provide most significant improvement in stress drop estimations. Assessment of optimal correction strategy may be needed for different study regions.
2. Frequency band is important. Insufficient bandwidth may lead to systematic underestimation, and increased scattering of corner frequency/stress drop. Interpretation of stress drop distributions should only include events within resolution limit of the available dataset.
3. Both apparent depth and magnitude dependence can be caused by poor corrections and limited frequency range. We see neither at Parkfield.
4. At Parkfield we observe strong, stable, spatial variability at small scale, with no significant dependence on the slip pattern (creeping versus locked) or the slip distribution of the M6 earthquake.
5. Temporal variations of stress drop following the 2004 M6 earthquake can be observed in regions with sufficient number of events and well-resolved

coseismic/post-seismic slip.

2.8 Acknowledgement

We thank Dr. Peter Shearer for sharing his ideas in the process of determining the SNSS method, and the USGS/HRSN personnel who collect and distribute Parkfield dataset online for public use (visit the USGS at https://usgs.gov for further details). Data for this study come from the High-Resolution Seismic Network (HRSN) doi:10.7932/HRSN, operated by the UC Berkeley Seismological Laboratory, which is archived at the Northern California Earthquake Data Center (NCEDC), doi:10.7932/NCEDC. Waveform data, metadata, or data products for this study were accessed through the Northern California Earthquake Data Center (NCEDC), doi:10.7932/NCEDC. This research project is supported by National Science Foundation (NSF) under Awards 1547071 and 1547083.

References

Abercrombie, R. E. (2000). Crustal attenuation and site effects at Parkfield, California. *Journal of Geophysical Research: Solid Earth*, *105*(3), 6277–6286. https://doi.org/10.1029/1999jb900425

Abercrombie, R. E. (1996). The magnitude-frequency distribution of earthquakes recorded with deep seismometers at Cajon Pass, southern California. *Tectonophysics*. https://doi.org/10.1016/0040-1951(96)00052-2

Abercrombie, R. E. (2014). Stress drops of repeating earthquakes on the San Andreas Fault at Parkfield. *Geophysical Research Letters*, *41*(24), 8784–8791. https://doi.org/10.1002/2014GL062079

Abercrombie, R. E. (2015). Investigating uncertainties in empirical Green's function analysis of earthquake source parameters. *Journal of Geophysical Research: Solid Earth*, *120*(6), 4263–4277. https://doi.org/10.1002/2015JB011984

Abercrombie, R. E. (2021). Resolution and uncertainties in estimates of earthquake stress drop and energy release. *Philosophical Transactions of the Royal Society A: Mathematical, Physical and Engineering Sciences* (Vol. 379). https://doi.org/10.1098/rsta.2020.0131

Abercrombie, R. E., Bannister, S., Ristau, J., & Doser, D. (2017). Variability of earthquake stress drop in a subduction setting, the Hikurangi Margin, New Zealand. *Geophysical Journal International*, *208*(1), 306–320. https://doi.org/10.1093/gji/ggw393

Abercrombie, R. E., Chen, X., & Zhang, J. (2020). Repeating Earthquakes With Remarkably Repeatable Ruptures on the San Andreas Fault at Parkfield. *Geophysical Research Letters*, *47*(23), 1–10. https://doi.org/10.1029/2020GL089820

Aki, K. (1967). Scaling law of seismic spectrum. *Journal of Geophysical Research*, *72*(4), 1217–1231. https://doi.org/10.1029/JZ072i004p01217

Allmann, B. P., & Shearer, P. M. (2007). Spatial and temporal stress drop variations in small earthquakes near Parkfield, California. *Journal of Geophysical Research: Solid Earth*, *112*(4), 1–17. https://doi.org/10.1029/2006JB004395

Allmann, B. P., & Shearer, P. M. (2009). Global variations of stress drop for moderate to large earthquakes. *Journal of Geophysical Research: Solid Earth*, *114*(1), 1–22. https://doi.org/10.1029/2008JB005821

Anderson, J. G., & Hough, S. E. (1984). A model for the shape of the fourier amplitude spectrum of acceleration at high frequencies. *Bulletin of the Seismological Society of America*, *74*(5), 1969–1993.

Bakun, W. H., & Lindh, A. G. (1985). The Parkfield, California, Earthquake Prediction Experiment. *Science*, *229*, 4714.

Baltay, A., Prieto, G., & Beroza, G. C. (2010). Radiated seismic energy from coda measurements and no scaling in apparent stress with seismic moment. *Journal of Geophysical Research: Solid Earth*, *115*(8), 1–12. https://doi.org/10.1029/2009JB006736

Baltay, A., Ide, S., Prieto, G., & Beroza, G. (2011). Variability in earthquake stress drop and apparent stress. *Geophysical Research Letters*, *38*(6), 1–6. https://doi.org/10.1029/2011GL046698

Ben-Zion, Y., & Zhu, L. (2002). Potency-magnitude scaling relations for Southern California earthquakes with 1.0 < ML < 7.0. *Geophysical Journal International*, *148*(3), F1–F5. https://doi.org/10.1046/j.1365-246X.2002.01637.x

Bennington, N., Thurber, C., & Roecker, S. (2008). Three-dimensional seismic attenuation structure around the SAFOD site, Parkfield, California. *Bulletin of the Seismological Society of America*, *98*(6), 2934–2947. https://doi.org/10.1785/0120080175

Bindi, D., Spallarossa, D., Picozzi, M., & Morasca, P. (2020). Reliability of source parameters for small events in central italy: Insights from spectral decomposition analysis applied to both synthetic and real data. *Bulletin of the Seismological Society of America*, *110*(6), 3139–3157. https://doi.org/10.1785/0120200126

Brenguier, F., Campillo, M., Hadziioannou, C., Shapiro, N. M., Nadeau, R. M., & Larose, E. (2008). Postseismic Relaxation Along the San Andreas Fault at Parkfield from Continuous Seismological Observations. *Science*, *321*(5895), 1478–1481. https://doi.org/10.1126/science.1160943

Brune, J. N. (1970). Tectonic stress and the spectra of seismic shear waves from earthquakes. *Journal of Geophysical Research*, *75*(26), 4997–5009. https://doi.org/10.1029/JB075i026p04997

Chaves, E. J., Schwartz, S. Y., & Abercrombie, R. E. (2020). Repeating earthquakes record fault weakening and healing in areas of megathrust postseismic slip. *Science Advances*, *6*(32), 2–10. https://doi.org/10.1126/sciadv.aaz9317

Chen, K. H., Bürgmann, R., Nadeau, R. M., Chen, T., & Lapusta, N. (2010). Postseismic variations in seismic moment and recurrence interval of repeating earthquakes. *Earth and Planetary Science Letters*, *299*(1–2), 118–125. https://doi.org/10.1016/j.epsl.2010.08.027

Chen, X., & Shearer, P. (2013). California foreshock sequences suggest aseismic triggering process. *Geophys. Res. Lett.*, *40*, 2602–2607. https://doi.org/10.1002/grl.50444

Chen, Xiaowei, & Abercrombie, R. E. (2020). Improved approach for stress drop estimation and its application to an induced earthquake sequence in Oklahoma. *Geophysical Journal International*, *223*(1), 233–253. https://doi.org/10.1093/gji/ggaa316

Custódio, S., Liu, P., & Archuleta, R. J. (2005). The 2004 Mw6.0 Parkfield, California, earthquake: Inversion of near-source ground motion using multiple data sets. *Geophysical Research Letters*, *32*(23), 1–4. https://doi.org/10.1029/2005GL024417

Dibblee, T.W., Jr. (1971). Geologic map of the Parkfield quadrangle, California: U.S. Geological Survey Open-File Map, 1 pl., scale 1:62,500

Dreger, D. S., Gee, L., Lombard, P., Murray, M. H., & Romanowicz, B. (2005). Rapid finite-source analysis and near-fault strong ground motions: Application to the 2003 Mw 6.5 San Simeon and 2004 Mw 6.0 Parkfield earthquakes.

Seismological Research Letters, *76*(1), 40–48. https://doi.org/10.1785/gssrl.76.1.40

Eshelby JD. (1957). The determination of the elastic field of an ellipsoidal inclusion, and related problems. *Proceedings of the Royal Society of London. Series A. Mathematical and Physical Sciences*, *241*(1226), 376–396. https://doi.org/10.1098/rspa.1957.0133

Goebel, T. H. W., Hauksson, E., Shearer, P. M., & Ampuero, J. P. (2015). Stress-drop heterogeneity within tectonically complex regions: A case study of San Gorgonio Pass, southern California. *Geophysical Journal International*, *202*(1), 514–528. https://doi.org/10.1093/gji/ggv160

Hanks, T. C., & Boore, D. M. (1984). Moment- magnitude relations in theory and practice. *Journal of Geophysical Research*, *89*(B7), 6229–6235. https://doi.org/10.1029/JB089iB07p06229

Hardebeck, J. L. (2020). Are the Stress Drops of Small Earthquakes Good Predictors of the Stress Drops of Moderate-to-Large Earthquakes? *Journal of Geophysical Research: Solid Earth*, *125*(3), 1–23. https://doi.org/10.1029/2019JB018831

Harris, R. A., & Segall, P. (1987). Detection of a locked zone at depth on the Parkfield, California, segment of the San Andreas fault (USA). *Journal of Geophysical Research*, *92*(B8), 7945–7962. https://doi.org/10.1029/JB092iB08p07945

Huang, Y., Ellsworth, W. L., & Beroza, G. C. (2017). Stress drops of induced and tectonic earthquakes in the central United States are indistinguishable. *Science Advances*, *3*(8), 1–8. https://doi.org/10.1126/sciadv.1700772

Imanishi, K., & Uchide, T. (2017). Non-self-similar source property for microforeshocks of the 2014 Mw 6.2 Northern Nagano, central Japan, earthquake. *Geophysical Research Letters*, *44*(11), 5401–5410. https://doi.org/10.1002/2017GL073018

Imanishi, Kazutoshi, & Ellsworth, W. L. (2006). Source scaling relationships of microearthquakes at Parkfield, CA, determined using the SAFOD Pilot Hole Seismic Array (pp. 81–90). https://doi.org/10.1029/170GM10

Jiang, J., Bock, Y., & Klein, E. (2021). Coevolving early afterslip and aftershock signatures of a San Andreas fault rupture. *Science Advances*, *7*(15), eabc1606. https://doi.org/10.1126/sciadv.abc1606

Kanamori, H. (1977). The energy release in great earthquakes. *Journal of Geophysical Research*, *82*(20), 2981–2987. https://doi.org/10.1029/jb082i020p02981

Kaneko, Y., & Shearer, P. M. (2014). Seismic source spectra and estimated stress drop derived from cohesive-zone models of circular subshear rupture. *Geophysical Journal International*, *197*(2), 1002–1015. https://doi.org/10.1093/gji/ggu030

Kaneko, Y., & Shearer, P. M. (2015). Variability of seismic source spectra, estimated stress drop, and radiated energy, derived from cohesive-zone models of symmetrical and asymmetrical circular and elliptical ruptures. *Journal of*

Geophysical Research: Solid Earth, *120*(2), 1053–1079. https://doi.org/10.1002/2014JB011642

Karageorgi, E., Clymer, R., & McEvilly, T. V. (1992). Seismological studies at Parkfield. II. Search for temporal variations in wave propagation using vibroseis. *Bulletin of the Seismological Society of America*, *82*(3), 1388–1415.

Kelly, C. M., Rietbrock, A., Faulkner, D. R., & Nadeau, R. M. (2013). Temporal changes in attenuation associated with the 2004 M6.0 Parkfield earthquake. *Journal of Geophysical Research: Solid Earth*, *118*(2), 630–645. https://doi.org/10.1002/jgrb.50088

Kim, A., Dreger, D. S., Taira, T., & Nadeau, R. M. (2016). Changes in repeating earthquake slip behavior following the 2004 Parkfield main shock from waveform empirical Green's functions finite-source inversion. *Journal of Geophysical Research B: Solid Earth*, *121*(3), 1910–1926. https://doi.org/10.1002/2015JB012562

Kwiatek, G., Bulut, F., Bohnhoff, M., & Dresen, G. (2014). High-resolution analysis of seismicity induced at Berlín geothermal field, El Salvador. *Geothermics*, *52*, 98–111. https://doi.org/10.1016/j.geothermics.2013.09.008

Lengliné, O., & Marsan, D. (2009). Inferring the coseismic and postseismic stress changes caused by the 2004 Mw = 6 Parkfield earthquake from variations of recurrence times of microearthquakes. *Journal of Geophysical Research: Solid Earth*, *114*(10), 1–19. https://doi.org/10.1029/2008JB006118

Li, Z., & Peng, Z. (2016). An automatic phase picker for local earthquakes with predetermined locations: Combining a signal-to-noise ratio detector with 1D velocity model inversion. *Seismological Research Letters*, *87*(6), 1397–1405. https://doi.org/10.1785/0220160027

Madariaga, R. (1976). Dynamics of an expanding circular fault. *Bulletin of the Seismological Society of America*, *66*(3), 639–666. Retrieved from http://bssa.geoscienceworld.org/content/66/3/639.abstract

Malagnini, L., Dreger, D. S., Bürgmann, R., Munafò, I., & Sebastiani, G. (2019). Modulation of Seismic Attenuation at Parkfield, Before and After the 2004 M6 Earthquake. *Journal of Geophysical Research: Solid Earth*, *124*(6), 5836–5853. https://doi.org/10.1029/2019JB017372

MALIN, P. E., BLAKESLEE, S. N., ALVAREZ, M. G., & MARTIN, A. J. (1989). Microearthquake Imaging of the Parkfield Asperity. *Science*, *244*(4904), 557–559. https://doi.org/10.1126/science.244.4904.557

Mayeda, K., Gök, R., Walter, W. R., & Hofstetter, A. (2005). Evidence for non-constant energy/moment scaling from coda-derived source spectra. *Geophysical Research Letters*, *32*(10), 1–4. https://doi.org/10.1029/2005GL022405

McLaskey, G. C., Thomas, A. M., Glaser, S. D., & Nadeau, R. M. (2012). Fault healing promotes high-frequency earthquakes in laboratory experiments and on natural faults. *Nature*, *491*(7422), 101–104. https://doi.org/10.1038/nature11512

Molkenthin, C., Scherbaum, F., Griewank, A., Leovey, H., Kucherenko, S., & Cotton, F. (2017). Derivative-based global sensitivity analysis: Upper bounding of sensitivities in seismic-hazard assessment using automatic differentiation.

Bulletin of the Seismological Society of America, *107*(2), 984–1004. https://doi.org/10.1785/0120160185

Moyer, P. A., Boettcher, M. S., McGuire, J. J., & Collins, J. A. (2018). Spatial and Temporal Variations in Earthquake Stress Drop on Gofar Transform Fault, East Pacific Rise: Implications for Fault Strength. *Journal of Geophysical Research: Solid Earth*, *123*(9), 7722–7740. https://doi.org/10.1029/2018JB015942

Murray, J., & Langbein, J. (2006). Slip on the San Andreas fault at Parkfield, California, over two earthquake cycles, and the implications for seismic hazard. *Bulletin of the Seismological Society of America*, *96*(4 B), 283–303. https://doi.org/10.1785/0120050820

Nadeau, R. M., & Johnson, L. R. (1998). Seismological studies at Parkfield VI: moment release rates and estimates of source parameters for small repeating earthquakes. *Bulletin of the Seismological Society of America*, *88*(3), 790–814.

Nadeau, R. M., & McEvilly, T. V. (1999). Fault slip rates at depth from recurrence intervals of repeating microearthquakes. *Science*, *285*(5428), 718–721. https://doi.org/10.1126/science.285.5428.718

Nadeau, R. M., & McEvitty, T. V. (2004). Periodic Pulsing of Characteristic Microearthquakes on the San Andreas Fault. *Science*, *303*(5655), 220–222. https://doi.org/10.1126/science.1090353

Noda, H., Lapusta, N., & Kanamori, H. (2013). Comparison of average stress drop measures for ruptures with heterogeneous stress change and implications for earthquake physics. *Geophysical Journal International*, *193*(3), 1691–1712. https://doi.org/10.1093/gji/ggt074

Oth, A. (2013). On the characteristics of earthquake stress release variations in Japan. *Earth and Planetary Science Letters*, *377–378*, 132–141. https://doi.org/10.1016/j.epsl.2013.06.037

Oth, A., Bindi, D., Parolai, S., & di Giacomo, D. (2011). Spectral analysis of K-NET and KiK-net data in Japan, Part II: On attenuation characteristics, source spectra, and site response of borehole and surface stations. *Bulletin of the Seismological Society of America*, *101*(2), 667–687. https://doi.org/10.1785/0120100135

Oye, V., Bungum, H., & Roth, M. (2005). Source parameters and scaling relations for mining-related seismicity within the Pyhäsalmi ore mine, Finland. *Bulletin of the Seismological Society of America*, *95*(3), 1011–1026. https://doi.org/10.1785/0120040170

Pennington, C. N., Chen, X., Abercrombie, R. E., & Wu, Q. (2021). Cross Validation of Stress Drop Estimates and Interpretations for the 2011 Prague, OK, Earthquake Sequence Using Multiple Methods. *Journal of Geophysical Research: Solid Earth*, *126*(3), 1–24. https://doi.org/10.1029/2020JB020888

Ruhl, C. J., Abercrombie, R. E., & Smith, K. D. (2017). Spatiotemporal Variation of Stress Drop During the 2008 Mogul, Nevada, Earthquake Swarm. *Journal of Geophysical Research: Solid Earth*, *122*(10), 8163–8180. https://doi.org/10.1002/2017JB014601

Scherbaum, F. (1990). Combined inversion for the three-dimensional Q structure and source parameters using microearthquake spectra. *Journal of Geophysical Research*, *95*(B8), 12423. https://doi.org/10.1029/JB095iB08p12423

Shearer, P. M., Prieto, G. A., & Hauksson, E. (2006a). Comprehensive analysis of earthquake source spectra in southern California. *Journal of Geophysical Research: Solid Earth*. https://doi.org/10.1029/2005JB003979

Shearer, P. M., Prieto, G. A., & Hauksson, E. (2006b). Comprehensive analysis of earthquake source spectra in southern California. *Journal of Geophysical Research: Solid Earth*, *111*(6), 1–21. https://doi.org/10.1029/2005JB003979

Shearer, P. M., Abercrombie, R. E., Trugman, D. T., & Wang, W. (2019). Comparing EGF Methods for Estimating Corner Frequency and Stress Drop From P Wave Spectra. *Journal of Geophysical Research: Solid Earth*, *124*(4). https://doi.org/10.1029/2018JB016957

Sheng, Y., Ellsworth, W. L., Lellouch, A., & Beroza, G. C. (2021). Depth Constraints on Coseismic Velocity Changes From Frequency-Dependent Measurements of Repeating Earthquake Waveforms. *Journal of Geophysical Research: Solid Earth*, *126*(2), 1–12. https://doi.org/10.1029/2020JB020421

Sumy, D. F., Neighbors, C. J., Cochran, E. S., & Keranen, K. M. (2017). Low stress drops observed for aftershocks of the 2011 Mw 5.7 Prague, Oklahoma, earthquake. *Journal of Geophysical Research: Solid Earth*, *122*(5), 3813–3834. https://doi.org/10.1002/2016JB013153

Thurber, C., Roecker, S., Zhang, H., Baher, S., & Ellsworth, W. (2004). Fine-scale structure of the San Andreas fault zone and location of the SAFOD target earthquakes. *Geophysical Research Letters*, *31*(12), n/a-n/a. https://doi.org/10.1029/2003gl019398

Thurber, Clifford, Zhang, H., Waldhauser, F., Hardebeck, J., Michael, A., & Eberhart-Phillips, D. (2006). Three-dimensional compressional wavespeed model, earthquake relocations, and focal mechanisms for the Parkfield, California, region. *Bulletin of the Seismological Society of America*, *96*(4 B), 38–49. https://doi.org/10.1785/0120050825

Trugman, D. T. (2020). Stress-drop and source scaling of the 2019 ridgecrest, California, earthquake sequence. *Bulletin of the Seismological Society of America*, *110*(4), 1859–1871. https://doi.org/10.1785/0120200009

Trugman, D. T., & Shearer, P. M. (2017). Application of an improved spectral decomposition method to examine earthquake source scaling in Southern California. *Journal of Geophysical Research: Solid Earth*, *122*(4), 2890–2910. https://doi.org/10.1002/2017JB013971

Uchide, T., Shearer, P. M., & Imanishi, K. (2014). Stress drop variations among small earthquakes before the 2011 Tohoku-oki, Japan, earthquake and implications for the main shock. *Journal of Geophysical Research: Solid Earth*, *119*(9), 7164–7174. https://doi.org/10.1002/2014JB010943

Waldhauser, F., Ellsworth, W. L., Schaff, D. P., & Cole, A. (2004). Streaks, multiplets, and holes: High-resolution spatio-temporal behavior of Parkfield seismicity. *Geophysical Research Letters*, *31*(18), 2–5. https://doi.org/10.1029/2004GL020649

Waldhauser, Felix. (2009). Near-real-time double-difference event location using long-term seismic archives, with application to northern California. *Bulletin of the Seismological Society of America*, *99*(5), 2736–2748. https://doi.org/10.1785/0120080294

Waldhauser, Felix, & Schaff, D. P. (2008). Large-scale relocation of two decades of Northern California seismicity using cross-correlation and double-difference methods. *Journal of Geophysical Research: Solid Earth*, *113*(8), 1–15. https://doi.org/10.1029/2007JB005479

Wu, Q., Chapman, M. C., Beale, J. N., & Shamsalsadati, S. (2016). Near-source geometrical spreading in the central virginia seismic zone determined from the aftershocks of the 2011 mineral, Virginia, earthquake. *Bulletin of the Seismological Society of America*, *106*(3), 943–955. https://doi.org/10.1785/0120150314

Ye, L., Lay, T., & Kanamori, H. (2013). Ground shaking and seismic source spectra for large earthquakes around the megathrust fault offshore of northeastern Honshu, Japan. *Bulletin of the Seismological Society of America*, *103*(2 B), 1221–1241. https://doi.org/10.1785/0120120115

Yenier, E., Atkinson, G. M., & Sumy, D. F. (2017). Ground Motions for Induced Earthquakes in Oklahoma. *Bull. Seismol. Soc. Am.*, *107*(1). https://doi.org/10.1785/0120160114

Yoshida, K., Saito, T., Urata, Y., Asano, Y., & Hasegawa, A. (2017). Temporal Changes in Stress Drop, Frictional Strength, and Earthquake Size Distribution in the 2011 Yamagata-Fukushima, NE Japan, Earthquake Swarm, Caused by Fluid Migration. *Journal of Geophysical Research: Solid Earth*, *122*(12). https://doi.org/10.1002/2017JB014334

Yoshimitsu, N., Ellsworth, W. L., & Beroza, G. C. (2019). Robust Stress Drop Estimates of Potentially Induced Earthquakes in Oklahoma: Evaluation of Empirical Green's Function. *Journal of Geophysical Research: Solid Earth*, *124*(6), 5854–5866. https://doi.org/10.1029/2019JB017483

Zeng, X., & Thurber, C. (2019). Three-dimensional shear wave velocity structure revealed with ambient noise tomography in the Parkfield, California region. *Physics of the Earth and Planetary Interiors*, *292*, 67–75. https://doi.org/10.1016/j.pepi.2019.05.007

Zhang, H., Liu, Y., Thurber, C., & Roecker, S. (2007). Three-dimensional shear-wave splitting tomography in the Parkfield, California, region. *Geophysical Research Letters*, *34*(24), 1–6. https://doi.org/10.1029/2007GL031951

Zhang, J., Chen, X., & Abercrombie, R. E. (2019). Resolving the spatiotemporal variability of small earthquake source parameters at Parkfield and their relationship with 2004M6 Parkfield earthquake. In *AGU Fall Meeting Abstracts* (Vol. 2019, pp. S52C-05).

Zoback, M., Hickman, S., & Ellsworth, W. (2011). Scientific drilling into the San Andreas fault zone - An overview of SAFOD's first five years. *Scientific Drilling*, (1), 14–28. https://doi.org/10.2204/iodp.sd.11.02.2011

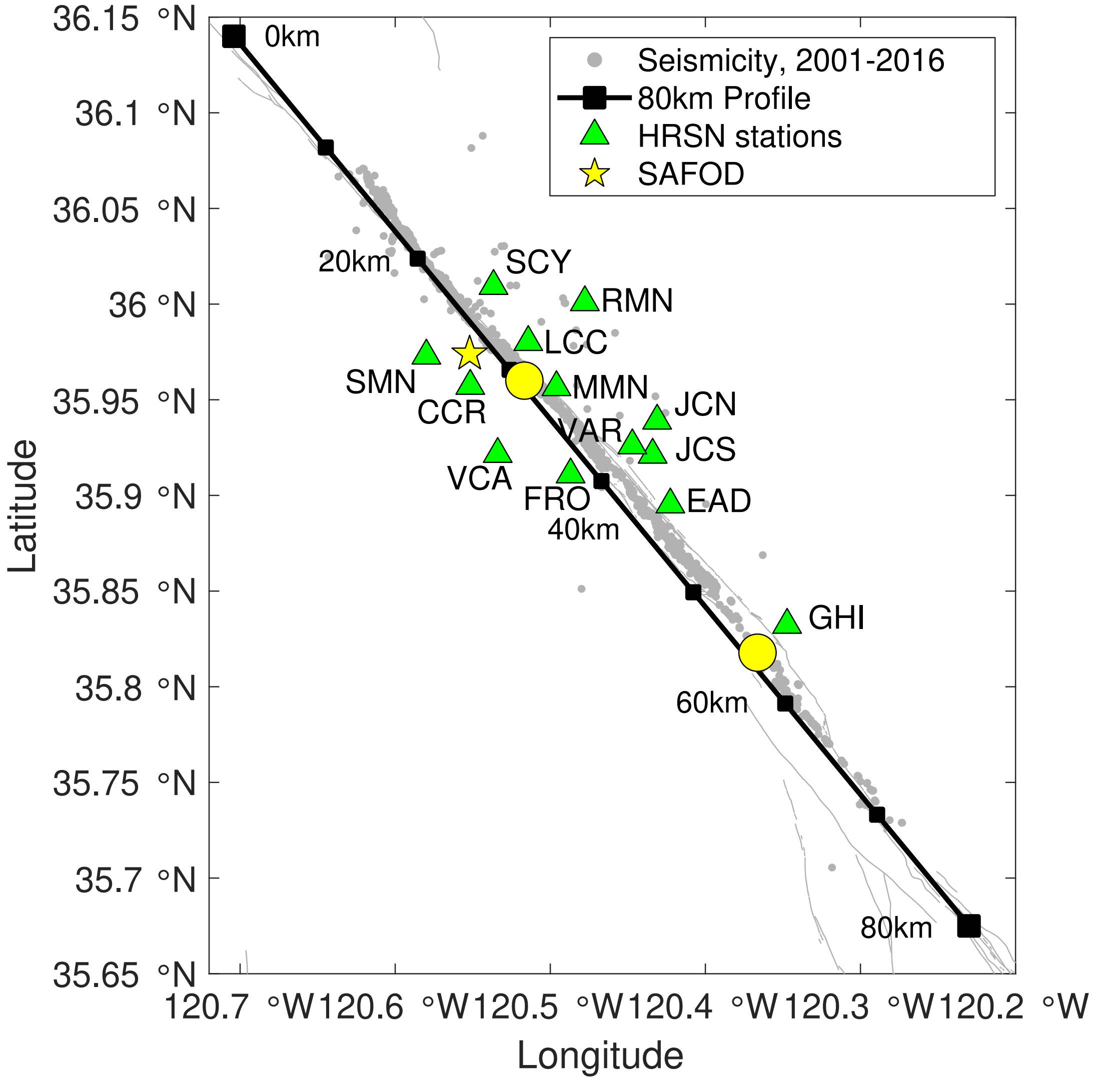

Figure 2.1: Seismicity map of research area. Fault lines are from USGS website (*Dibblee, 1971*), and event locations follow the double-difference catalog by *Waldhauser & Schaff (2008).*

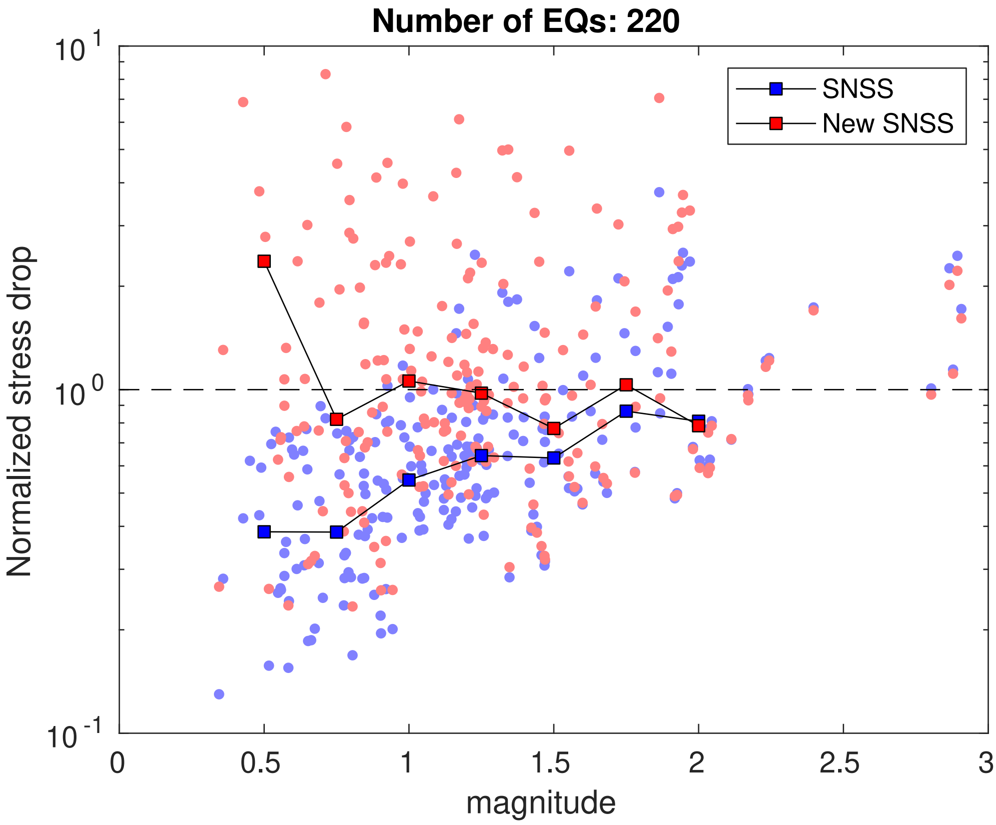

Figure 2.2: Comparison between the SNSS method (blue) and the new hybrid SNSS method (red) in terms of magnitude dependence using 220 earthquakes selected from depth between 4-5km depth and 30-40km from NW end of SAF profile. Y-axis represents the ‘normalized stress drop’ which is calculated by dividing the per-event individual stress drops by the median of stress drop of M>1.5 events. The square lines show the median of normalized stress drop in magnitude bins [0.5:0.25:3] with the bin size of 0.5 from the corresponding methods.

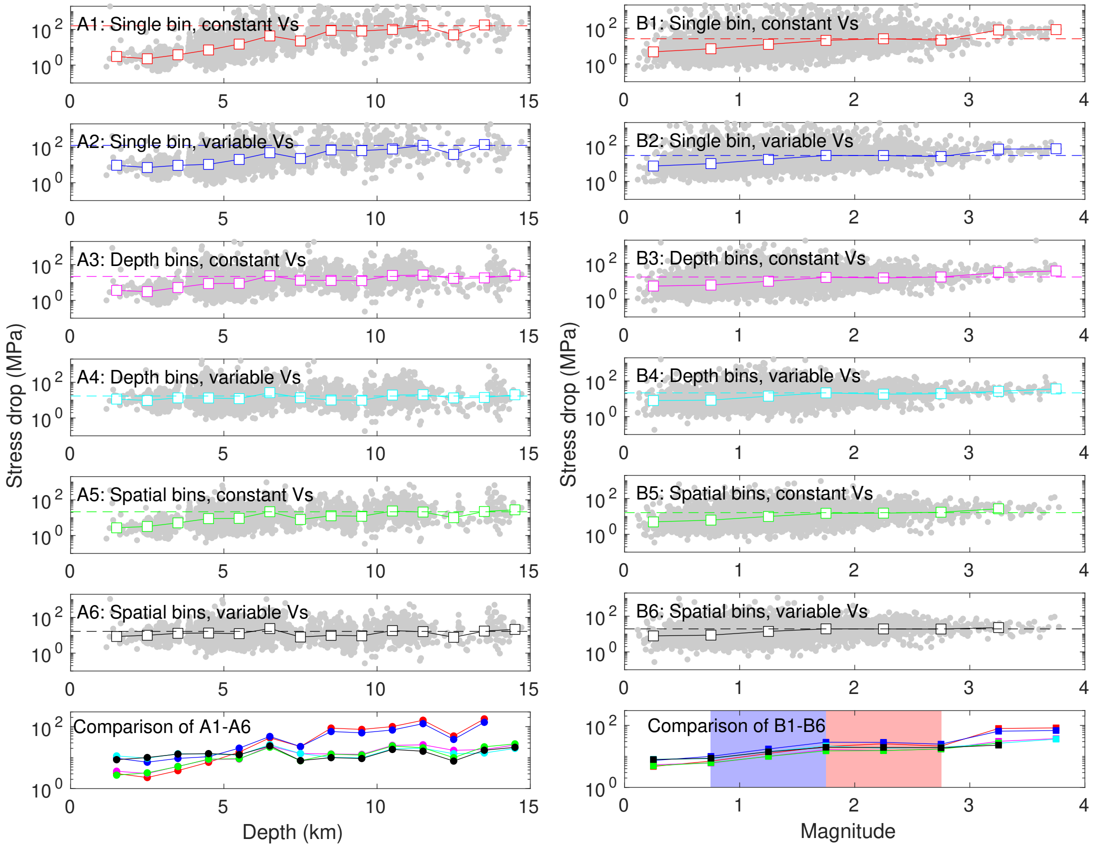

Figure 2.3: Complete comparison among different strategies for stress drop depth dependence (A1-A6) and magnitude dependence (B1-B6). Black is the strategy that is finally applied. The gray dots represent the stress drop measurements and the squares are the median values calculated in 1km depth bin for depth dependence (A1-A6) and M0.5 bin magnitude dependence (B1-B6). Magnitude range marked by light blue area the bottom right panel shows where magnitude scaling is observed, and oppositely for that marked as light red.

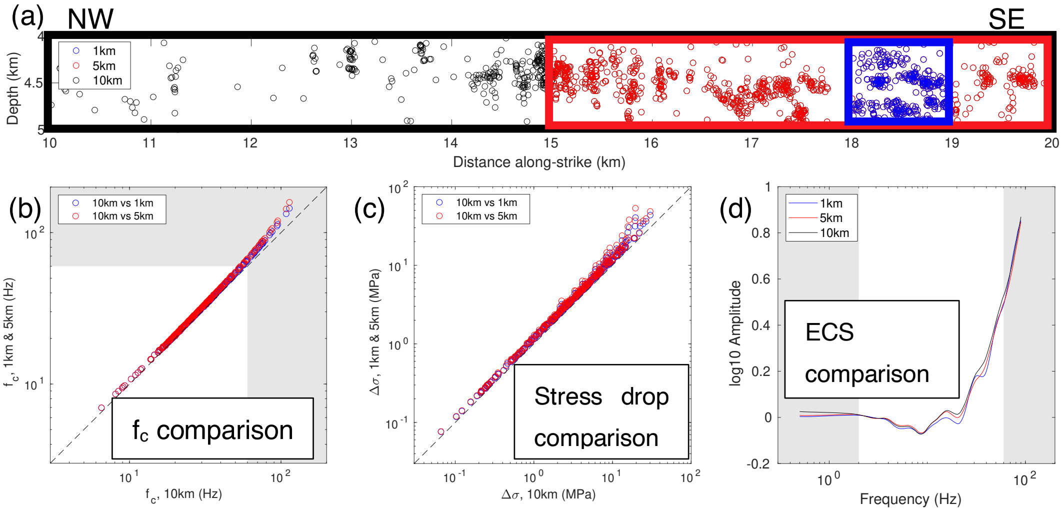

Figure 2.4: (a) Bin size selection, 1km VS 5km VS 10km along strike and 1km depth range. (b) corner frequency comparison between 10km bin and 1km (blue) and 5km (red) bin, (c) stress drop comparison between 10km bin and 1km (blue) and 5km (red) bin, and (d) the ECSs solved from each bin size. Shadow areas represent frequency band out of fitting range (lower than 2Hz and higher than 60Hz), and black dashed lines point out the identical value. The 10km-by-1km area is selected for this test because of its high event density, and is highlighted in Figure 2.6(a) as a black box.

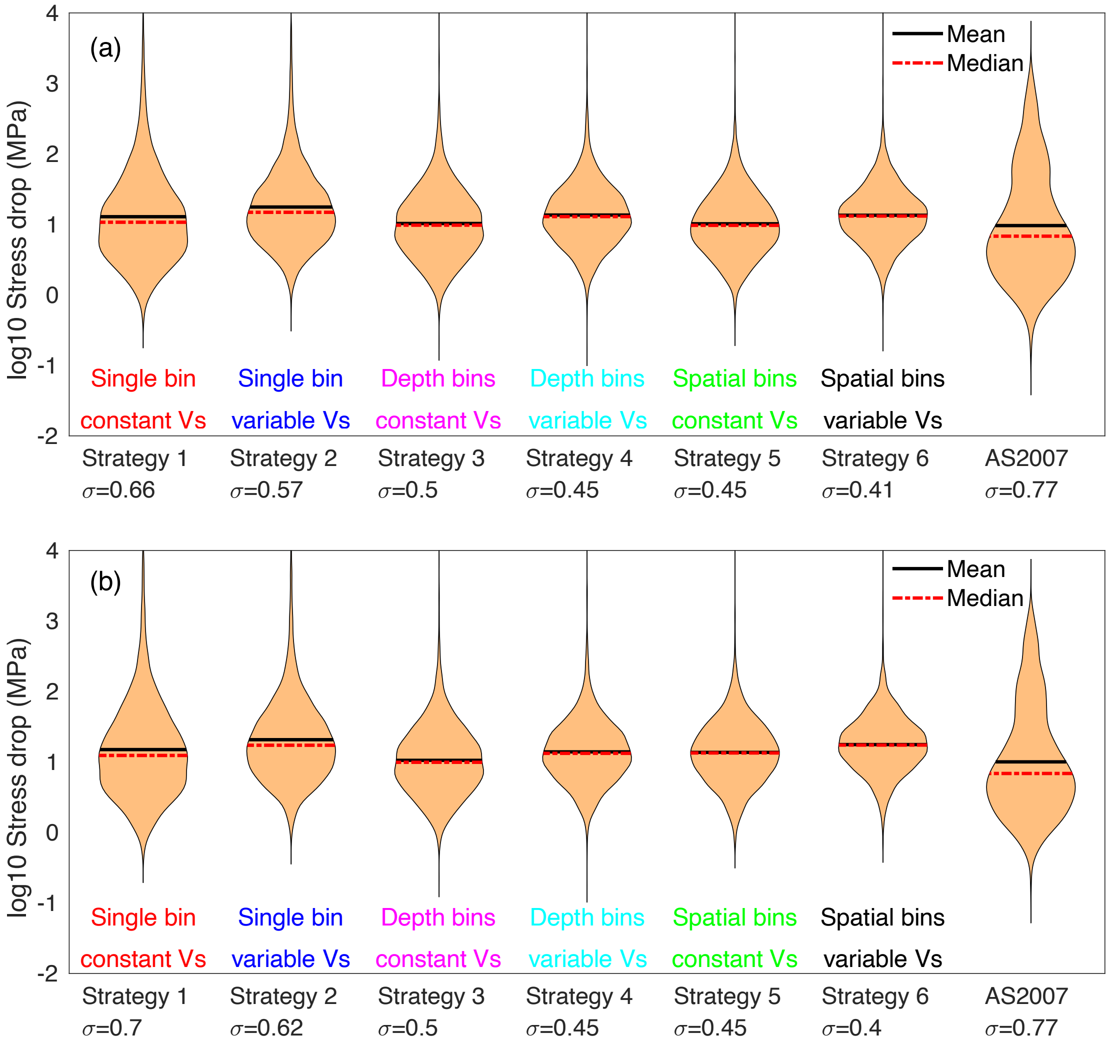

Figure 2.5: Histogram of stress drop estimates (a) before and (b) after temporal correction, per strategy and AS2007, and the standard deviation of log10 stress drops in each case. The black and red dashed bars represent mean and median log10 stress drops.

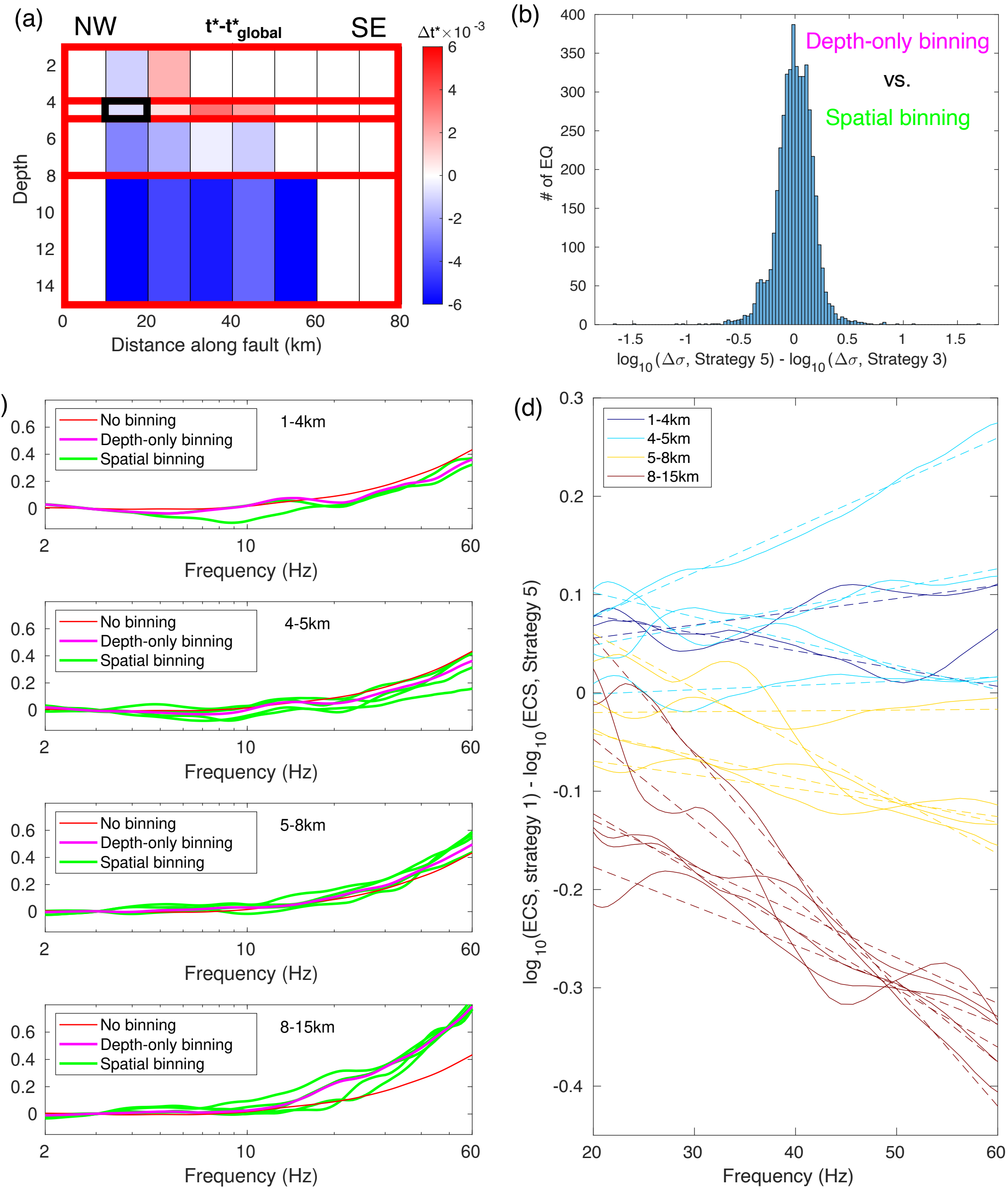

Figure 2.6: (a) t* variability among both the horizontal and vertical bins, showing the layered distribution. The exact values are from the slope derived from the linear fitting of the difference between ECSs in all the bins from Strategy 5 and the ECS from Strategy 1. Thick black box indicates the spatial bin used in test shown in Figure 4. (b) histogram of log10 stress drop difference of individual earthquakes between Strategy 3 and 5. (c) ECSs from different Strategies in different horizontal bins, by depth ranges (Red: Strategy 1 with no spatial binning which is identical in different depths, Magenta: Strategy 3 with depth-only binning, Green: Strategy 5 with spatial binning). (d) Strategy 5 ECSs subtracted by Strategy 1 ECS, different colors distinguish depth bins, and the multiple curves with the same color come from different horizontal bins in the same depth bin. Dashed lines are linear fit to the solid curves between 20Hz and 60Hz, and their slopes are used to evaluate t* variation over space in (a).

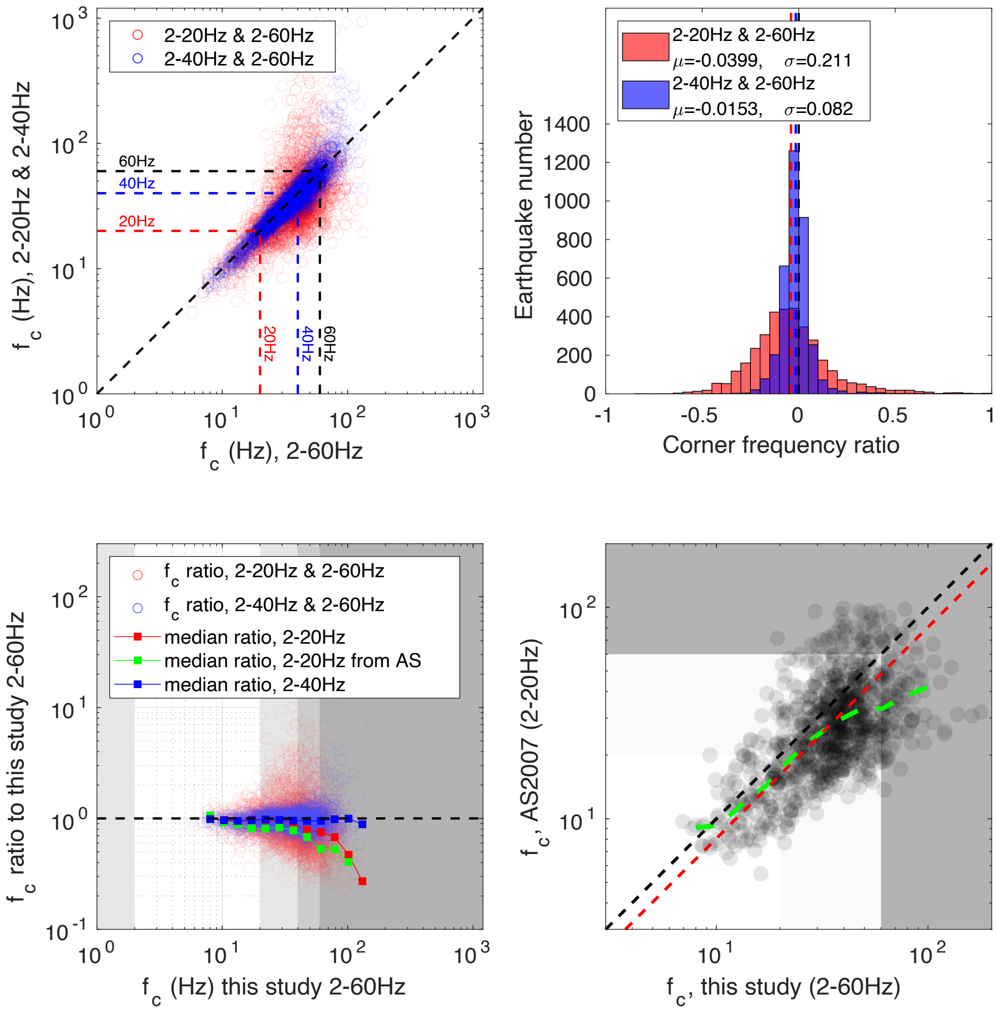

Figure 2.7: Real data test, using different frequency ranges (2-20Hz, 2-40Hz and 2-60Hz) for corner frequency inversion. (a) 1-to-1 comparison between frequency ranges. Horizontal and vertical dashed lines point out the upper limits of frequency ranges, and the diagonal dashed line is where fc estimates are identical. (b) Histogram of log10 corner frequency ratio between 2-20Hz, 2-40Hz and 2-60Hz. Red and blue vertical dashed lines respectively show the mean values of both cases, and the black vertical dashed line is zero point. (c) Corner frequency ratio between 2-20Hz and 2-60Hz, and between 2-40Hz and 2-60Hz, median (red and blue squares) is calculated from the individual ratios between two adjacent squares with minimum of 5 earthquakes. Green squares are the median if the 2-20Hz results is replaced with AS2007. Black horizontal dashed line indicates where the results are the same. Areas with different darkness represent the corner frequency band outside of 2-20Hz, 2-40Hz and 2-60Hz. (d) Comparison of individual earthquake corner frequencies between this study and AS2007 (transparent black circles). Black dashed line represents where two studies are consistent and red represents where corner frequencies are 1.5 times of those in AS2007. The white area stands for the frequency limit in AS2007 (20Hz), the light gray area

between the frequency limits of AS2007 (20Hz) and this study (60Hz), and the dark gray area higher than the frequency limit in this study (60Hz). The green dashed curve is the median of corner frequencies of AS2007 relative to those in this study.

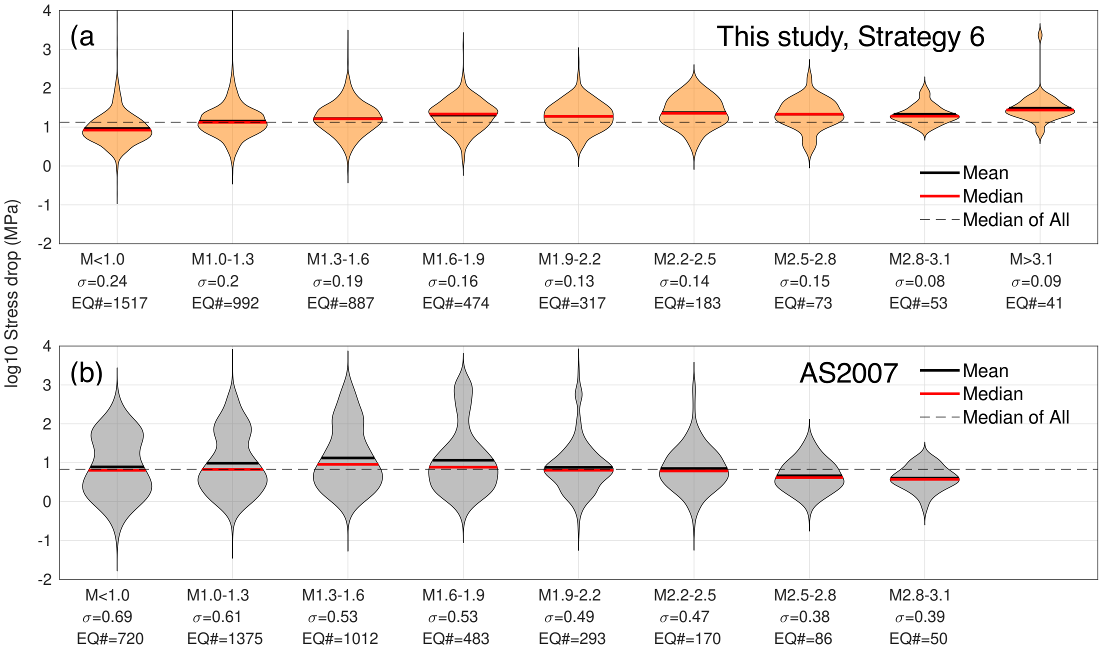

Figure 2.8: Violin plot of stress drops by magnitude for this study using Strategy 6 (a, yellow) and AS2007 (b, grey). Black and red bars represent mean and median values in each magnitude range. The horizontal dashed lines are showing the median values for all the stress drops in both studies

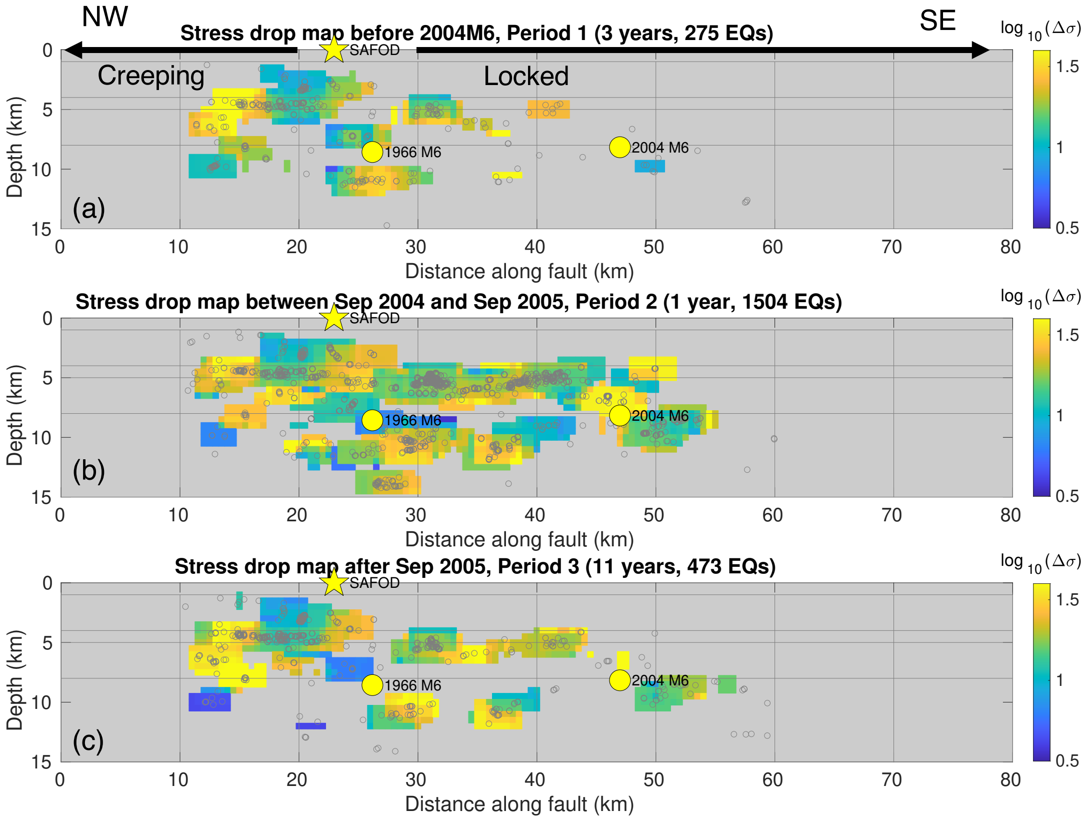

Figure 2.9: Spatial distribution of stress drop in the 3 time periods shown in Figure S8 with **only Mw>1.1 earthquakes**. The color is coded by the log10 stress drop values in every 4km-by-2km block with moving interval of 0.5km both horizontally and vertically. The yellow star is the location of SAFOD, and yellow circles are the locations of the 1996 M6 and 2004 M6 earthquakes. The gray open circles are the seismicity included in this study.

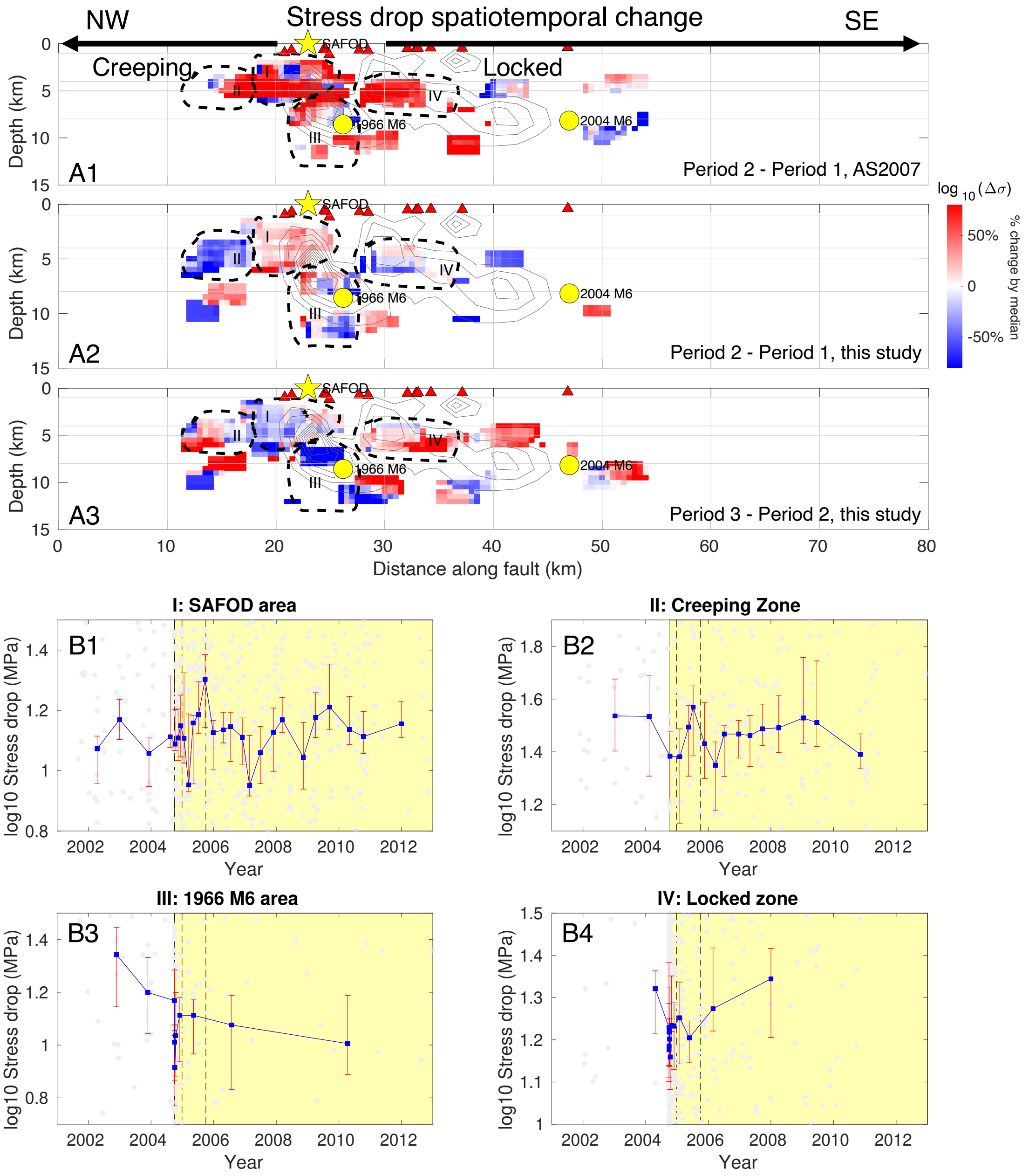

Figure 2.10: Stress drop change among the 3 time periods indicated in Figure 10 using only Mw>1.1 earthquakes. (A1) difference between pre-Sep 2004 and Sep 2004-Sep 2005 using AS2007 results for comparison with A2, (A2) difference between pre-Sep 2004 and Sep-2004 and Sep-2005 from this study, (A3) difference between Sep 2004-Sep 2005 and post-Sep 2005 from this study. Color represents the percentage of log10 stress drop difference to the over stress drop standard deviation to describe how much change of stress drop over time and space. (B1-B4) Stress drop temporal change in the circled zone in dashed curves: I. SAFOD area, II. Creeping Zone, III. 1966 M6 area, IV. Locked zone, where the blue line is the median stress drop curve over time calculated from the stress drops of the nearest certain earthquakes, and the red error bars describe the range of median stress drops defined by 30 times of bootstrapping medians from the 70% among the nearest earthquakes for each blue dot. Two vertical dashed lines mark the 3-month and 1-year time point after 2004 M6 earthquake.

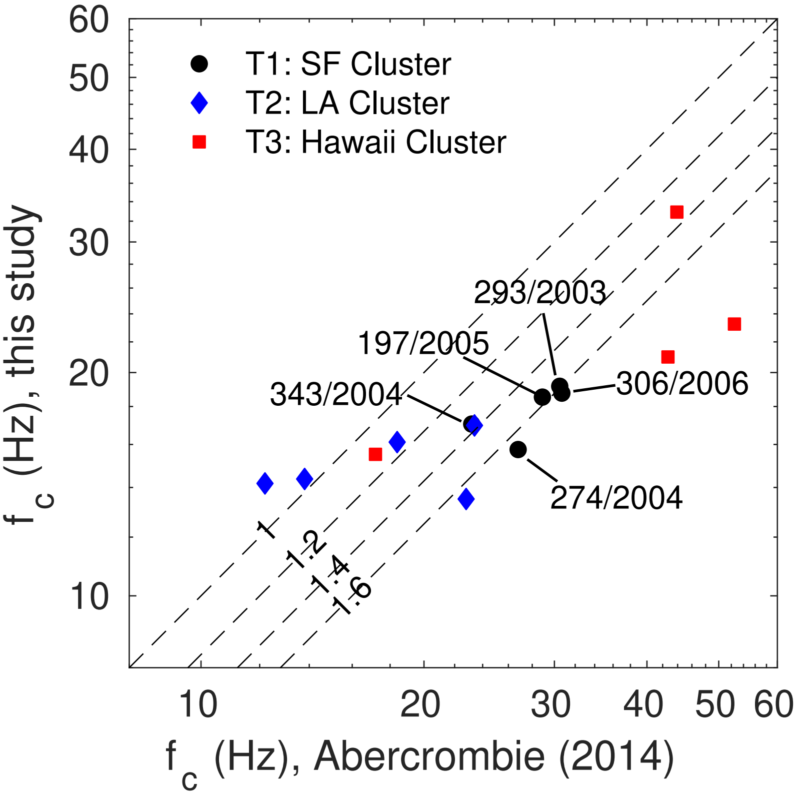

Figure 2.11: Comparison of individual corner frequencies in this study and those in Abercrombie (2014). Different colors and markers shown in the legend represent different SAFOD targeted clusters. Different dashed lines indicate the factor (numbers on the lines) corresponding constant shift from the diagonal aka. identical values. The Julian days of the events in cluster T1 are marked in the figure; for reference, the 2004 Parkfield M6 occurred on 272/2004.

Appendix

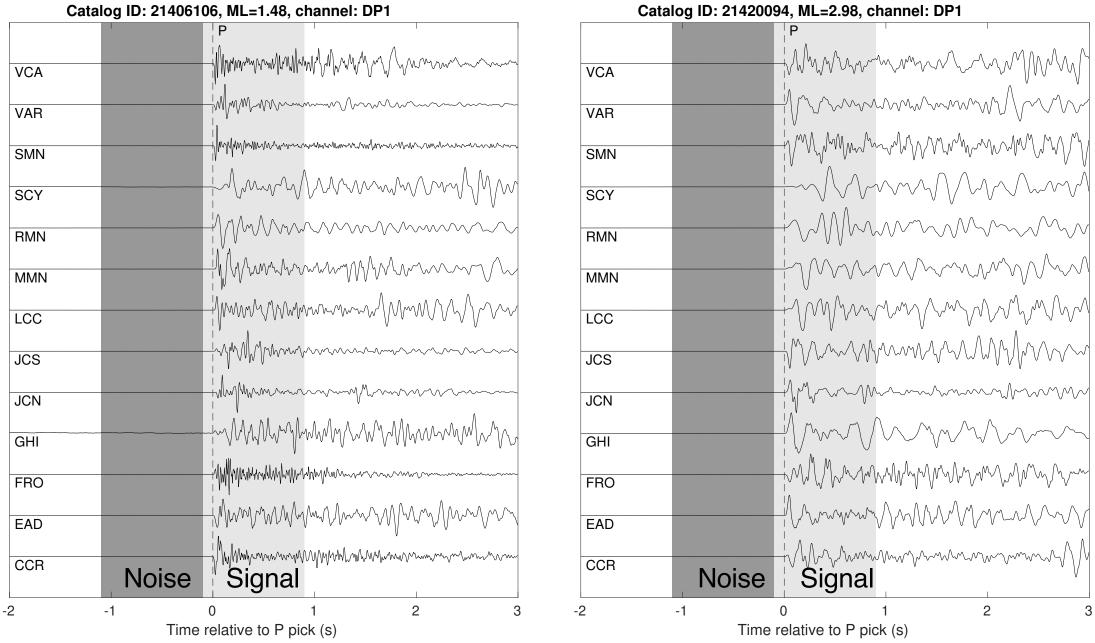

Figure S2.1: Example waveforms of two earthquakes recorded at HRSN stations with different magnitudes used in the stress drop estimation. Waveforms are aligned by P arrival picks at the stations. Dark and light gray areas represent the P noise (1s) and signal (1s) windows for spectrum computation. The signal window starts from -0.1s of the P arrivals and ends at 0.9s after the P arrivals.

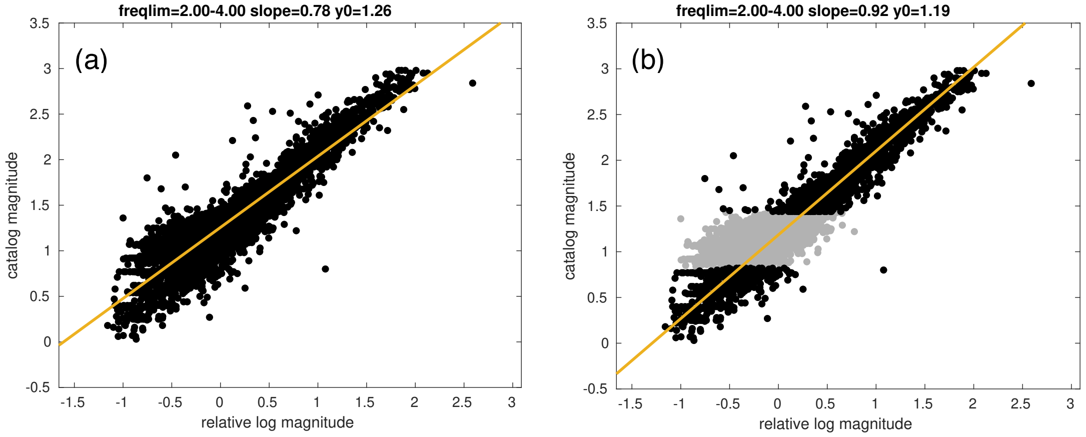

Figure S2.2: Magnitude calibration, individual earthquakes are shown as black dots. (a) the abnormal amplitudes at around M1 result in biased linear fitting (slope=0.78). (b) after removing M0.83-M1.40 earthquakes (gray dots) ONLY in the calibration, we obtain slope=0.92 and linear fitting is more reasonable. The removed earthquakes are still involved in the following spectral analysis.

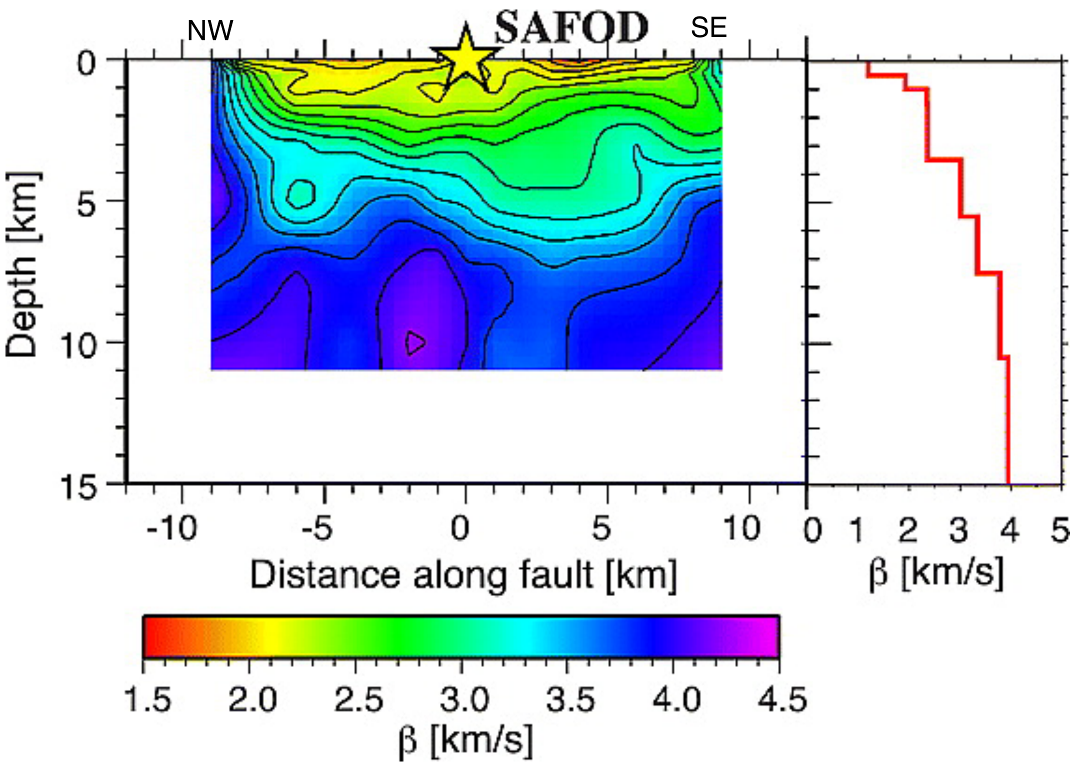

Figure S2.3: Velocity model for depth-varying rupture velocity (*Allmann and Shearer, 2007*, Figure 5). Within the scale of 10km, the velocity variation along strike similar to that in the scale of 1km over depth, and vertically the velocity model shows significant velocity contrast. The velocity model validates our spatial bin size selection as in Figure S5.

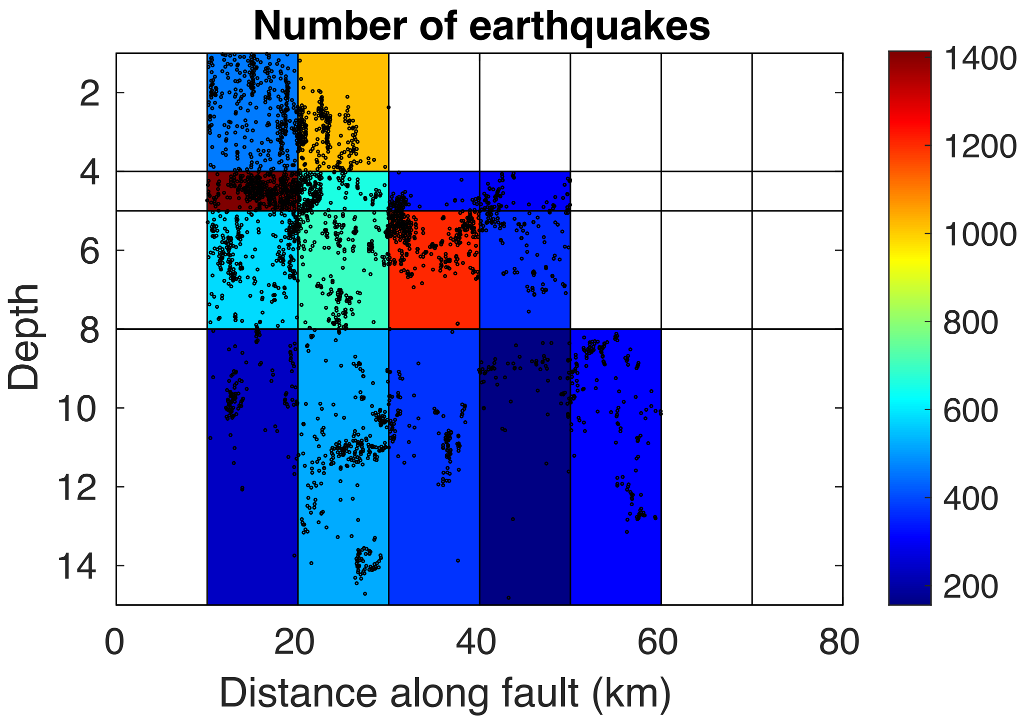

Figure S2.4: Spatial bins setup, totally 32 bins and 15 bins with earthquakes more than 200 to ensure SNSS method stability. Color indicates the number of earthquakes in each bin.

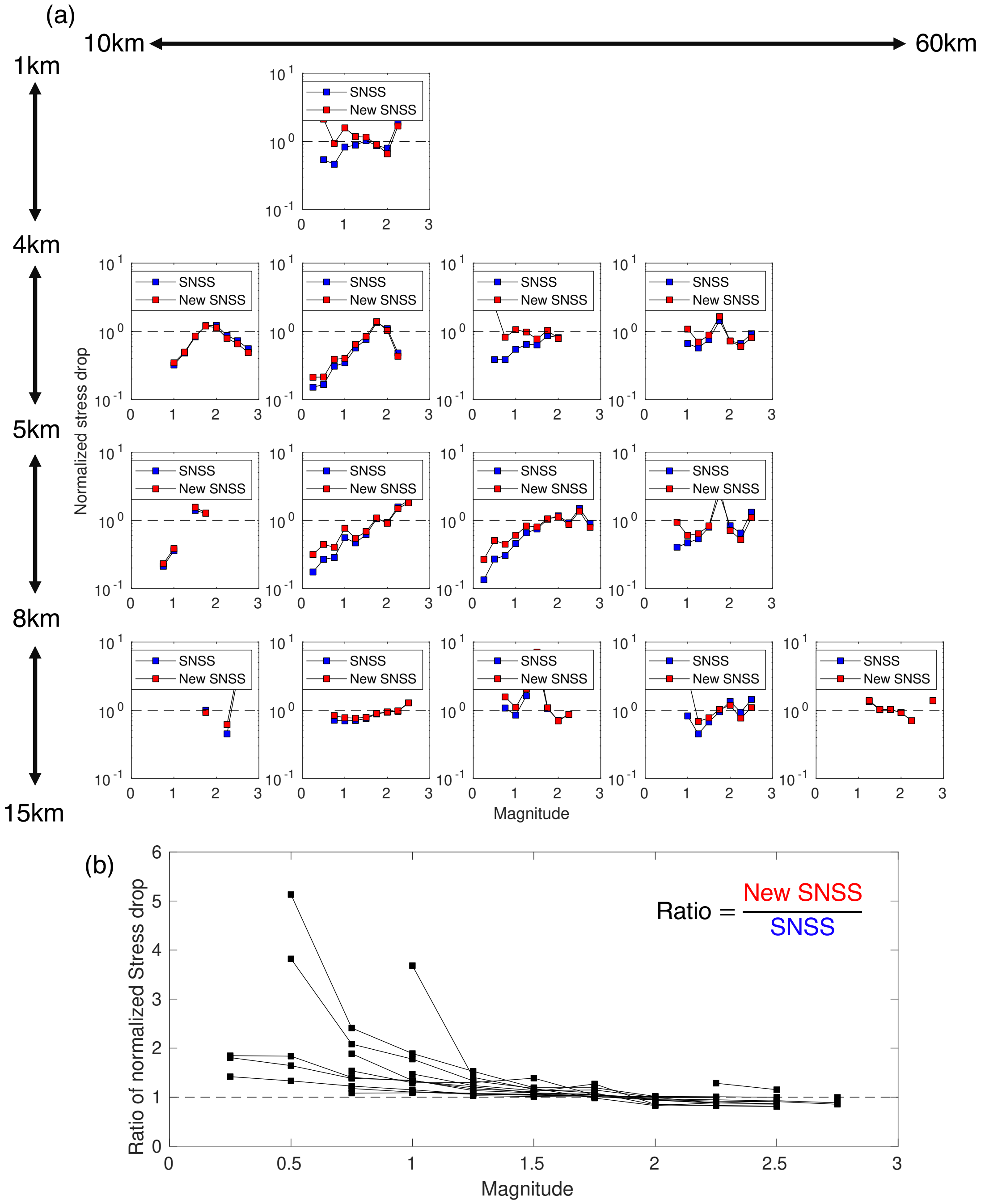

Figure S2.5: (a) Per spatial bin, normalized stress drop (by median of stress drop for M>1.5) VS magnitude between the new SNSS method (blue) and the old SNSS method (red). Squares are the median values calculated in 0.25 length magnitude windows. (b) Compiled results of Hybrid SNSS results (red) divided by SNSS (blue) in different spatial bins in the top panel.

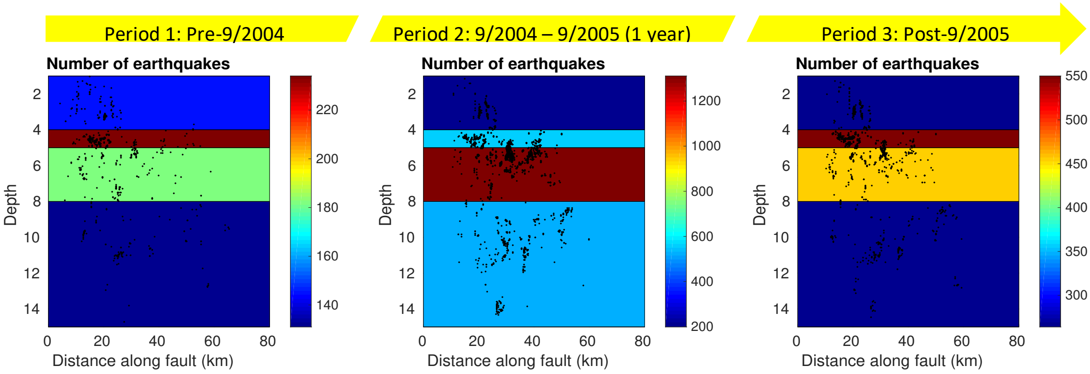

Figure S2.6: 3 time periods and the earthquake distribution in the layered bins accounting for temporal attenuation variations (Period 1: pre-2004 M6, Period 2: one-year period after 2004 M6, Period 3: After the one-year period). Only depth bins are applied with colors showing the number of earthquakes in the bins.

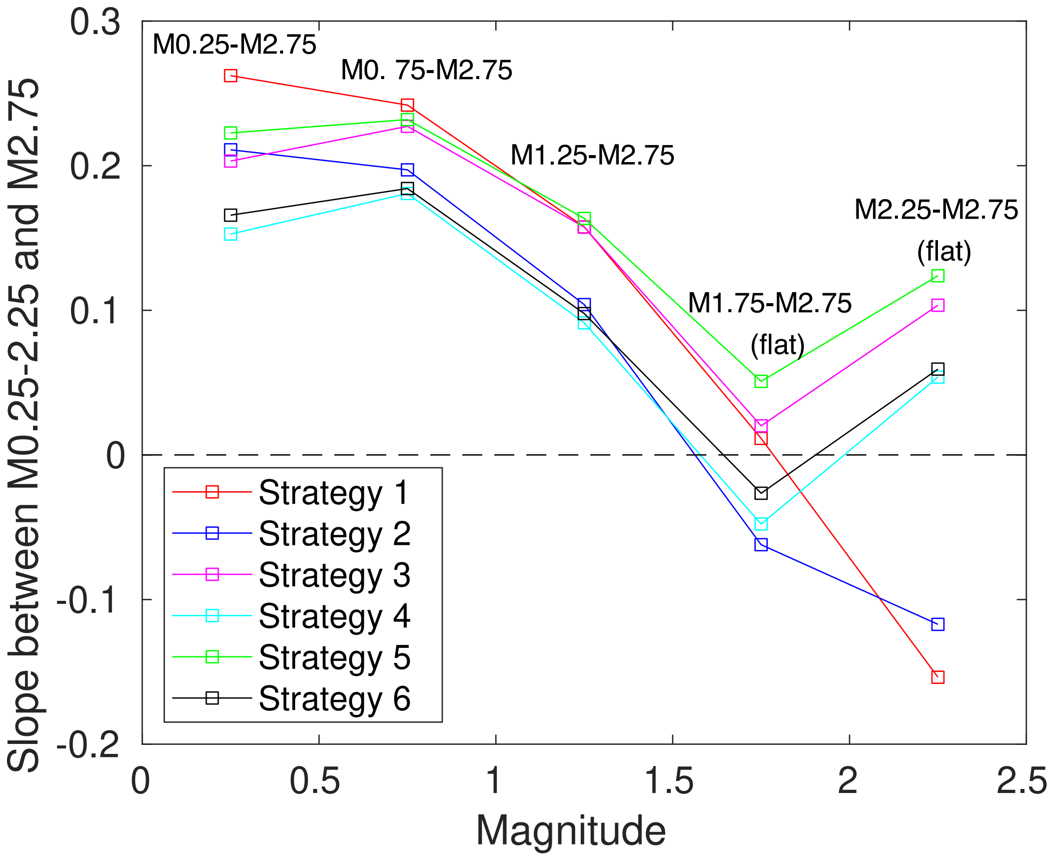

Figure S2.7: After temporal attenuation correction, calculation of slope between M0.25/0.75/1.25/1.75/2.25 and M2.75 to examine where the magnitude scaling of stress drop starts to appear (with temporal correction of attenuation). Different colors represent Strategies from 1 to 6. A slope close to 0 means there is no scaling between a certain magnitude and M2.75.

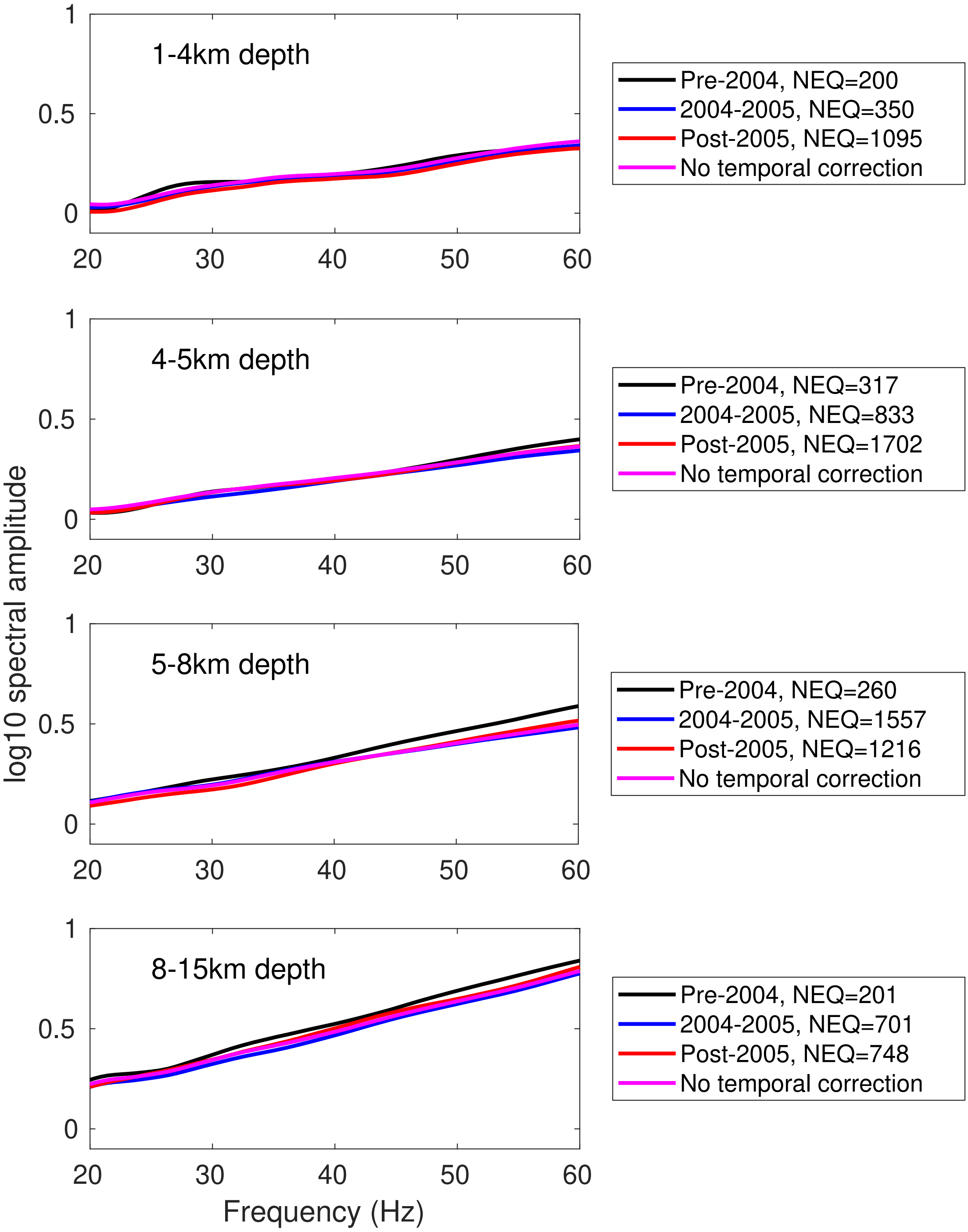

Figure S2.8: ECS temporal change in different depth ranges (Black: before Sep. 2004, Blue: Sep. 2004 - Sep. 2005, Red: after Sep. 2005) when only considering depth binning. This is to show the potential attenuation change over time at different depths.

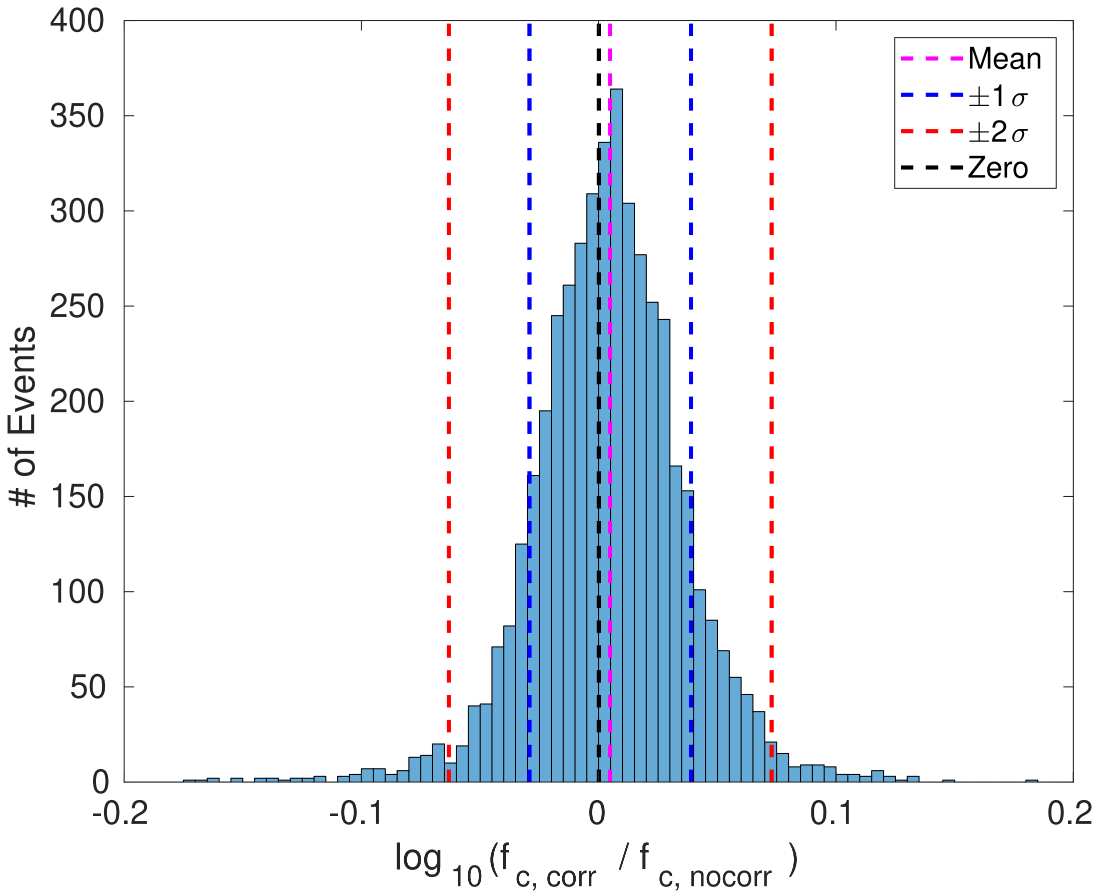

Figure S2.9: Difference of corner frequencies of Individual events between temporal correction and non-temporal correction. The difference is measured by the log10 of ratio between the individual corner frequencies for individual events in the two cases. The average of difference *m* is 0.0048 (1.011 times of difference) shown as magenta dashed line in comparison to consistency in black dashed line, and the standard deviation *s* is 0.034 with blue dashed lines showing *m* ± *s* (76.3% of total events) and red dashed lines showing *m* ± 2*s* (95.2% of total events).

(a)

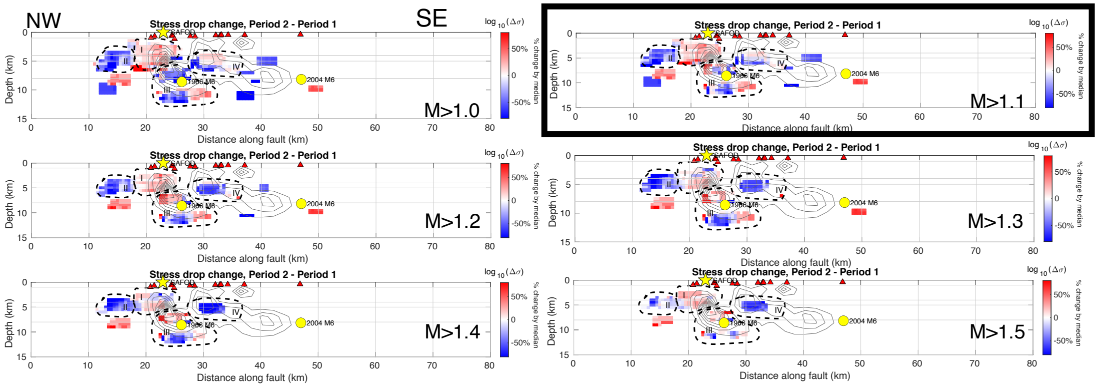

(b)

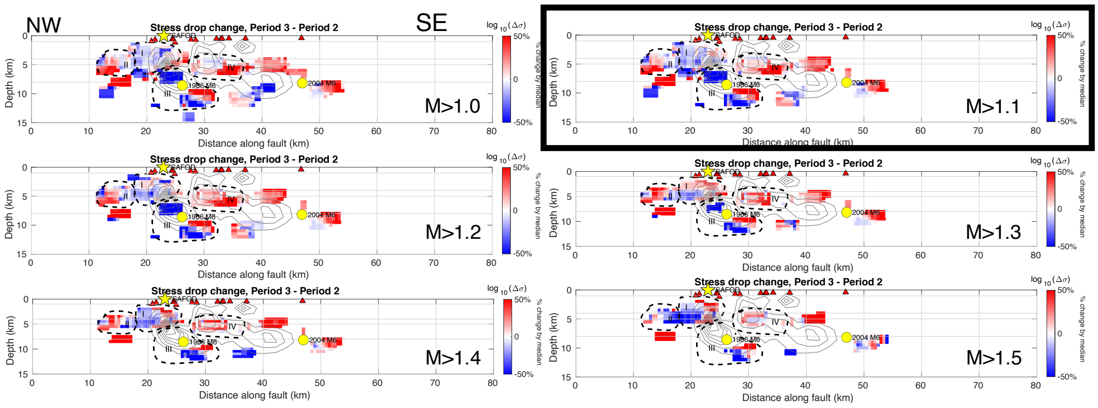

(Continued in the next page)

(Continued)

(c)

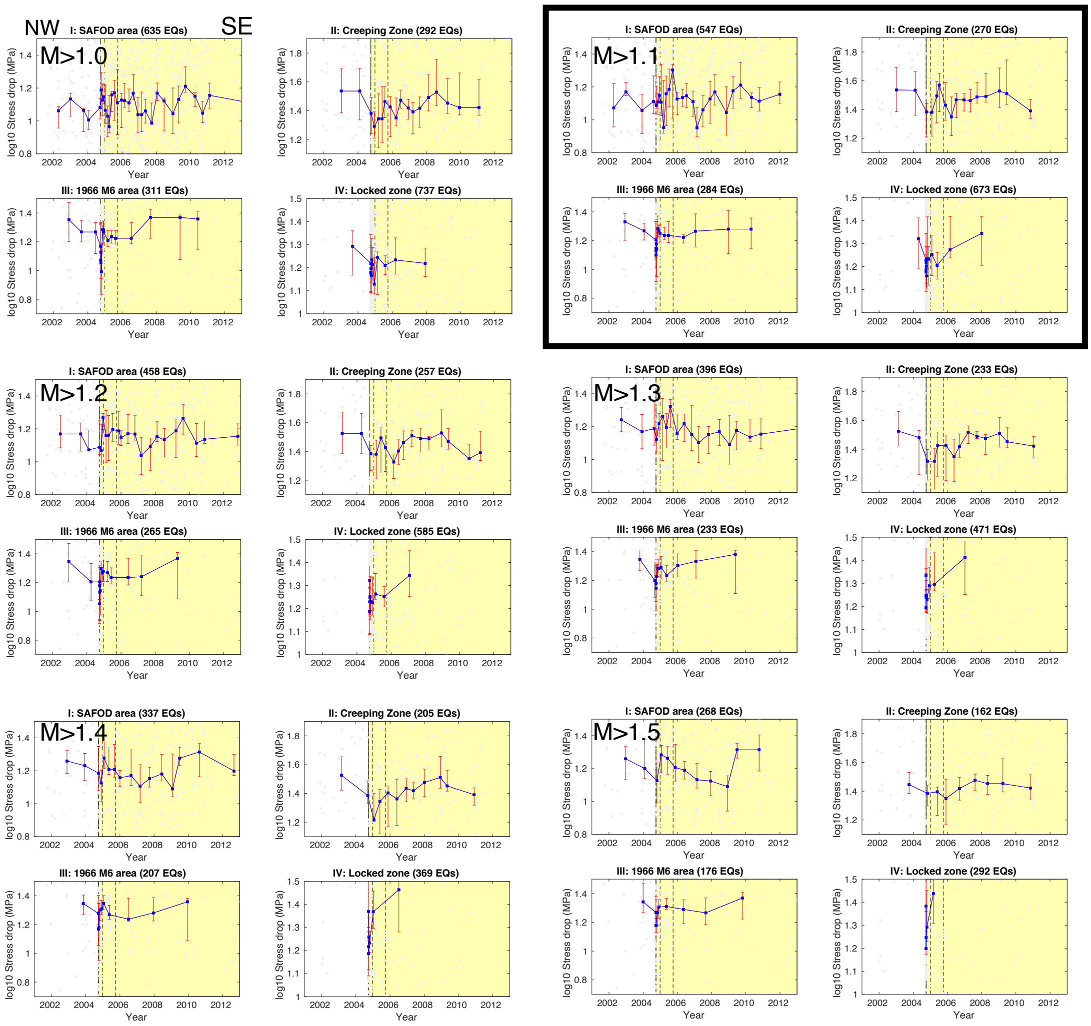

Figure S2.10: A demonstration of how magnitude threshold affects stress drop change over time. (a) difference between pre-Sep 2004 and Sep 2004-Sep 2005, with different magnitude thresholds, (b) Difference between Sep 2004-Sep 2005 and post-Sep 2005, and (c) the detailed temporal change within the 1966 M6 slip patch marked with black dashed lines for different magnitude thresholds. All the items in this figure share the same meanings as those in Figure 11. Black squares point out the threshold used for final results. In each panel above, only the first subplot has NW and SE marks indicating the direction of the section on the SAF, and all the other subplots follow the same direction.

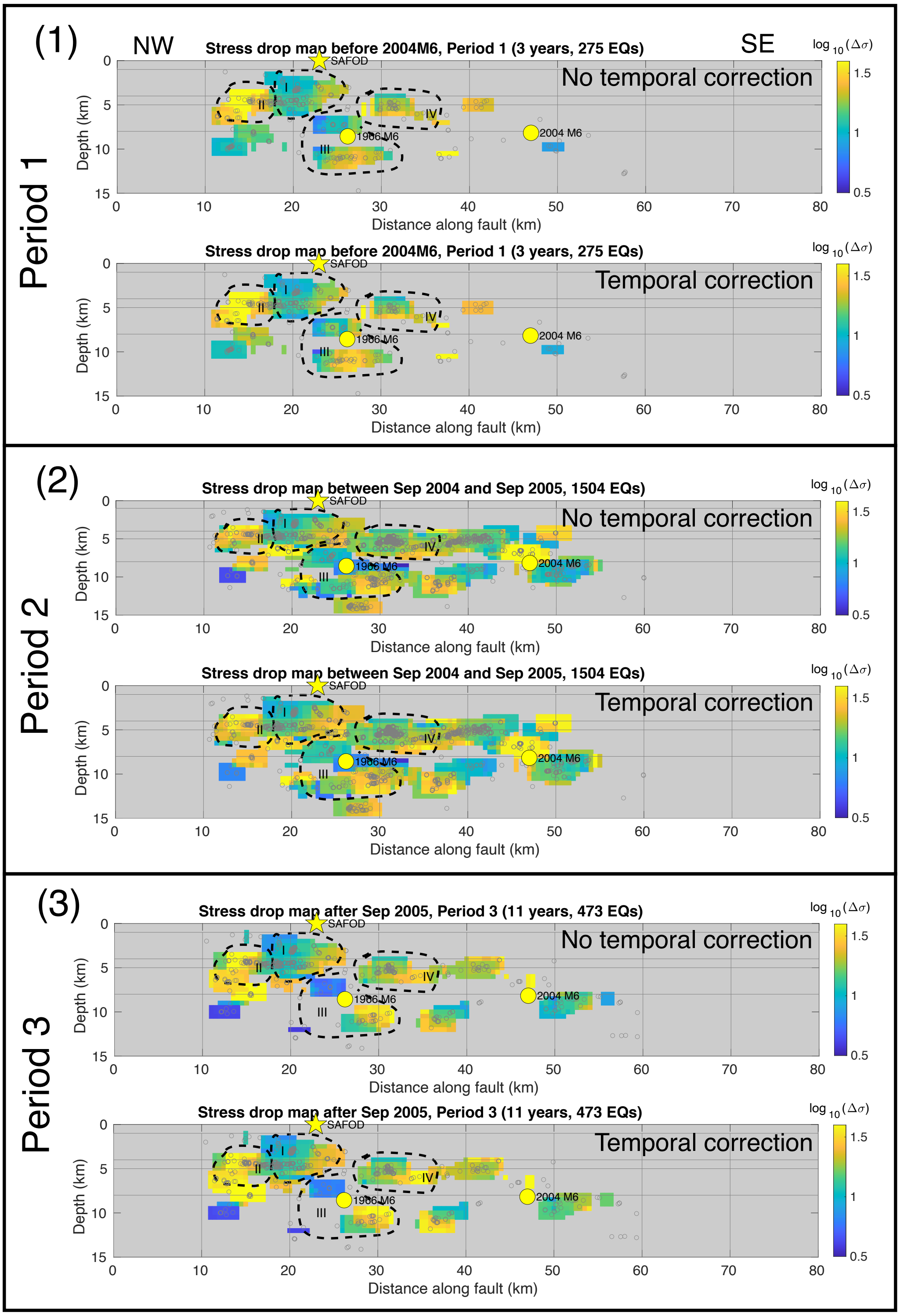

Figure S2.11: Comparison of spatial patterns of stress drop before and after temporal attenuation correction. The spatial distributions are remarkably similar, indicating the influence of temporal attenuation is minimal. Only Mw>1.1 earthquakes are included. (1-3) represent the comparison in 3 different time periods described in the texts.

Strategy name	Data organization	Shear velocity
Strategy 1	No binning	Constant
Strategy 2	No binning	Depth-varying
Strategy 3	Depth binning	Constant
Strategy 4	Depth binning	Depth-varying
Strategy 5	Spatial binning	Constant
Strategy 6	Spatial binning	Depth-varying

Table 2.1: Strategy name and how data and parameters are organized and selected in each strategy.

Strategies		Magnitude dependence				Depth dependence			
		*0.75-1.75		1.75-2.75		1.5-6.5km		6.5-11.5km	
		Slope	R^2	Slope	R^2	Slope	R^2	Slope	R^2
No temporal correction	1. Single Bin, constant Vs	0.499	0.999	0.055	0.479	0.221	0.855	0.156	0.717
	2. Single bin, variable Vs	0.460	0.999	0.024	0.774	0.118	0.674	0.124	0.648
	3. Depth bins, constant Vs	0.428	0.999	0.022	0.149	0.173	0.886	0.023	0.080
	4. Depth bins, variable Vs	0.404	0.997	-0.050	0.391	0.070	0.632	-0.008	0.008
	5. Spatial Bins, constant Vs	0.384	0.998	0.059	0.823	0.174	0.952	0.037	0.141
	6. Spatial Bins, variable Vs	0.354	0.989	-0.012	0.997	0.072	0.780	0.006	0.003
Temporal correction	1. Single Bin, constant Vs	0.504	0.998	0.041	0.167	0.230	0.869	0.145	0.749
	2. Single bin, variable Vs	0.478	0.998	-0.038	0.570	0.128	0.715	0.116	0.657
	3. Depth bins, constant Vs	0.434	1.000	0.020	0.149	0.163	0.880	0.028	0.117
	4. Depth bins, variable Vs	0.409	1.000	-0.048	0.399	0.060	0.561	-0.004	0.002
	5**. Spatial Bins, constant Vs	0.413	0.999	0.051	0.593	0.170	0.930	0.042	0.201
	6**. Spatial Bins, variable Vs	0.395	0.995	-0.026	0.222	0.068	0.691	0.010	0.012
Slope change percentage after temporal correction.	1. Single Bin, constant Vs	1.00%		-		4.07%		-	
	2. Single bin, variable Vs	3.91%		-		8.47%		-	
	3. Depth bins, constant Vs	1.40%		-		-0.58%		-	
	4. Depth bins, variable Vs	1.24%		-		-14.29%		-	
	5**. Spatial Bins, constant Vs	7.55%		-		-2.30%		-	
	6**. Spatial Bins, variable Vs	11.58%		-		-5.56%		-	

Table 2.2: Linear regression results to estimate stress drop dependence on magnitude and depth with different Strategies and temporal correction options. Both magnitude and depth are separated into two ranges with and without apparent scaling (Scaling: Mw0.75-1.75, Non-scaling: Mw1.75-2.75). An example to calculate slope change percentage: for Strategy 4, 11.58%=(0.395-0.354)/0.354*100%. *The magnitude scaling range is determined in Figure S6 by calculating the slope between a certain magnitude and Mw2.75. When Mw>1.75, such slopes become centered at 0 for most of the Strategies, meaning the flat part starts from around Mw1.75. **Note that for 5 and 6, the ECSs for each spatial bin is corrected using the ECSs from depth-binning only in Strategy 3 from corresponding time periods.

Chapter 3 Evaluating source parameters resolution of small earthquakes from multiple factors – an example at Parkfield, California

3.1 Abstract

Uncertainties in source parameter estimation such as corner frequency and stress drop can be caused by multiple factors, such as different parameter selection, instruments and methods. Large uncertainties can bias our interpretation of the earthquake source processes, therefore it is important to understand the source and degree of uncertainties. We apply multiple methods to solve for small earthquake source parameters in Parkfield area using different frequency bands and seismic networks (lower sampling rate surface network and higher sampling rate borehole network). Using the multi-scale approach, we evaluate the influence of different factors on the corner frequency resolution. We find that with sufficient bandwidth, different methods can obtain similar results. When bandwidth is insufficient, corner frequencies above the resolution limit can have very different results depending on different methods. Corner frequencies that are within resolution limits tend to be similar across different methods. Our results suggest that consistency across multiple methods indicates the corner frequency is well resolved.

3.2 Introduction

Earthquake source parameters, including corner frequency and stress drop, are important for understanding the earthquake source process and high-frequency ground motion. Source parameters can be obtained by estimating corner frequencies from the

Brune-type source model (*Brune, 1970*) from P and S wave source spectra. However, although they are very simple to estimate, they are usually subject to large uncertainties, especially for small earthquakes (such as Mw<3).

Waveforms of earthquakes are often recorded on multiple seismic networks with different setups and instrument responses. The waveforms are converted to displacement or velocity spectra using Fourier Transform that will be used to obtain source spectra and estimate corner frequencies, thus corner frequency uncertainties can be affected by seismic data selection and processing using these networks. More specifically, waveforms on surface networks (e.g. Northern California Seismic Network) are usually coupled with site amplification (*Bard & Bouchon, 1985*) and corner frequency may be biased due to the bump in spectra at certain frequency bands. Different networks generally use different types of instruments, and may have different sampling rates, which could affect the available bandwidth for spectral analysis. Moreover, intrinsic attenuation of waveform during propagation can be related to the depth of station (*Abercrombie, 2000*), meaning waveforms recorded by surface and borehole (e.g. High-Resolution Seismic Network at Parkfield, California, abbr. HRSN) networks may have different attenuation problems. To mitigate the uncertainties in corner frequencies, appropriate instrument or attenuation corrections are needed.

Frequency band selection is another significant factor that contributes to the uncertainties in the corner frequency estimation process. To estimate Brune stress drop, we fit source spectra to the Brune-type source model in a certain frequency band to find the best-fit corner frequency. It has been found that a wide frequency band is important to minimize the uncertainties in corner frequency estimates, and a limited bandwidth with a low upper bound may lead to source parameter underestimation (*Ide & Beroza, 2001, Abercrombie, 2021; Zhang et al., 2019*). *Chen & Abercrombie (2020)* quantified the resolvable corner frequency range given a certain upper bound, concluding that the resolvable range is between 40% and 80% of the upper limit is averaged from multiple stations. *Viegas et al. (2010)* showed a limited bandwidth can cause corner frequency underestimation when solving for attenuation Q value. The available bandwidth is sometimes limited by the available dynamic range of instruments as well as noise level, therefore seismic stations with low sampling rate are not capable of resolving high corner frequencies that may exceed their upper limits.

The chosen method to solve for earthquake corner frequency also has an impact on the accuracy. Popular methods include the Spectral Decomposition and Stacking method (*Shearer et al., 2006a*) and Spectral Ratio method (e.g. *Abercrombie, 2014; Ruhl et al., 2017*). The Spectral Ratio method can remove the path/site term by taking the spectral ratio between a larger target earthquake and a collocated smaller event as Empirical Green's function (EGF) recorded on the same station, the selection of EGF event can greatly influence corner frequency estimation of the target earthquake (e.g. *Abercrombie, 2015*). The Spectral Decomposition and Stacking method and its variants (e.g., *Trugman & Shearer, 2017; Chen & Abercrombie, 2020*) iteratively solve for earthquake source spectra and use a stacking-based approach to solve for a global Empirical Correction Spectrum (ECS) to estimate individual earthquake corner frequencies. Sometimes assumption of magnitude dependence is required, which is usually unknown and a topic to study; the event spectra stacking process helps obtain a smooth overall ECS, but the stacking process itself may cause biased spectrum shape, and site/path information may be absorbed into source term that can be difficult to remove.

In this study, we aim at evaluating the corner frequency resolution by comparing the corner frequency and stress drop estimates of individual earthquakes using different seismic networks, frequency bands and methods. We choose to use Parkfield earthquakes near San Andreas Fault Observatory at Depth (SAFOD) due to the accumulated knowledge on the earthquake source properties in this area. We attempt to use different frequency bandwidths for different seismic networks, and also develop a new method based on the original Spectral Decomposition and Stacking method developed by *Shearer et al., (2006a)* and modified by *Chen & Abecrombie (2020)*. The new method in this study attempts to mitigate the bias during the stacking process. We compare the performance of the new method and previous stacking method.

3.3 Data

We select the Parkfield area in California, USA, a tectonically active zone with abundant small earthquakes (see Figure 3.1 for details). This area includes a ‘creeping zone’ to the northwest of Parkfield and a ‘locked zone’ to the southeast of Parkfield separated by the Middle Mountain Asperities (*Harris & Segall, 1987*). Multiple major earthquakes occurred in this area, such as 1966 M6 earthquake and 2004 M6 earthquake. We use data from the High-Resolution Seismic Network (HRSN), which is a local borehole network at several hundreds of meters deep with 250Hz sampling rate, and the Northern California Seismic Network (NCSN), which is a surface network with mostly 100 Hz sampling rate. The earthquakes are selected from a double-difference relocation catalog (WNC, *Waldhauser & Schaff, 2008; Waldhauser, 2009*) from the Northern California Earthquake Data Center (NCEDC), and these earthquakes were recorded by HRSN during 2001-2016 and by NCSN during 1984-2016 in our database. We choose an area with the highest event density along the SAF segment, which is located near the 1966 M6 hypocenter and SAFOD. The area is 20 km along-strike and 2-5 km in depth (dark green block in Figure 3.1(1), details in Figure 3.1(2)). We only include events that are recorded by both the HRSN and NCSN networks to ensure consistency of the comparison. We also only use a portion of the entire NCSN network, so the station azimuthal coverage and station numbers are comparable (18 NCSN and 13 HRSN stations are included). Due to potential clipping issue, we limit the magnitude range to Mw0 to Mw4.

We first calculate the P-wave velocity spectra of the selected earthquakes recorded by HRSN and NCSN networks, respectively, in a one-second window around the P-arrivals on the stations (0.1s before arrival and 0.9s after arrival) using a multi-taper method, then convert the velocity spectra to displacement spectra. Noise spectra are also calculated but in the one-second window before the arrival, and signal-to-noise ratio (SNR) per frequency sampling point can be evaluated. We only choose earthquakes with minimum SNR of 10 between 2-60Hz for HRSN and 2.5 between 2-20Hz for NCSN, and these earthquakes need to be recorded on at least 5 stations in each network. Then the source parameters will be estimated inside the same networks (e.g., HRSN only and NCSN only) so that there is no necessity to remove the instrument response, because it can be removed during the spectral decomposition process. After data selection, we have 465 earthquakes that meet the data selection criteria from both networks.

3.4 Method

3.4.1 Estimating corner frequency and calculate stress drop from source spectra

We assume the earthquake source spectra can be approximated with Brune-type shape (*Brune, 1970*):

$$s(f) = \frac{\mathrm{M}_0}{1 + \left(\frac{f}{f_c}\right)^n} \tag{3.1}$$

where f_c is the corner frequency, and n is the high-frequency fall-off rate and set to 2 (ω^{-2} model). For small earthquakes, we assume simple circular rupture, and source radius r can be connected to corner frequency according to *Brune (1970)* and *Madariaga (1976)*:

$$r = k\frac{\beta}{f_c} \tag{3.2}$$

where β represents the shear velocity, and k is a constant that depends on model assumptions, such as the source geometry, and rupture velocity (*Kaneko & Shearer, 2014; 2015*). We choose k=0.32 for P wave from *Madariaga (1976)* to keep consistency with *Allmann & Shearer (2007)*, which will be discussed in the following section. Then we follow *Eshelby (1957)* to calculate stress drop $\Delta\sigma$ from seismic moment (M_0) and source radius:

$$\Delta\sigma = \frac{7}{16}\left(\frac{M_0}{r^3}\right) = M_0\left(\frac{f_c}{0.42\beta}\right)^3 \tag{3.3}$$

Here we use a constant rupture velocity β =3.464km/s (same as *Allmann & Shearer, 2007*) because the area is compact, and we assume the rupture velocity is consistent everywhere inside.

3.4.2 Approaches to solve for the source parameters

We involve multiple approaches to estimate source parameters, in which some are estimated in this study and others are from previously published results. There are roughly two types of methods: 1. Spectral Decomposition and Stacking, and 2. Spectral Ratio.

3.4.2.1 Spectra Decomposition and Stacking:

1) Stacking-Self-Similarity (SSS): this method has been applied to solve for stress drop and corner frequency in a variety of studies (*Shearer et al., 2006a; Allmann & Shearer, 2007; Chen & Shearer, 2013*). It first uses an iterative method to separate source, path and station terms in the frequency domain, then stack the source term of earthquakes in different magnitude bins to obtain smoothed spectra. Assuming constant stress drop for different magnitudes bins, an ECS to correct the stacked spectra to Brune shape is obtained by minimizing the difference between theoretical Brune-shape spectra and stacked source spectra in magnitude bins. A stress drop value is associated with this ECS and describes the average stress drop in the area. It has the advantage of solving for stress drops for numerous earthquakes efficiently, but the constant stress drop assumption may be questionable and whether stress drop scales with magnitude is still under debate. We use *Allmann & Shearer (2007)* results, which we call AS2007 in the following contents, for the representative of the SSS method.

2) Stacking-No-Self-Similarity (SNSS): this is a very similar method to the SSS method developed in *Chen & Abercrombie (2020)*, while it does not assume self-similarity, generate an ECS from a reference bin, and minimize the difference between ECS corrected spectra and Brune-shape spectra in all other available magnitude bins (Figure 3.2(1)). This does not rely on constant stress drop assumption, and will be used in our own source parameter analysis.

3) Global-Optimization-based Spectral Correction (GOSC, Figure S3.1): this is a new method proposed in this study, which takes the advantage of a global optimization algorithm named Differential Evolution (*Storn & Price, 1997*) to look for the best set of stress drops for all the magnitude bins instead of assuming any magnitude scaling relationship of stress drop. Different bins can have their own ECSs, while they are required to be as similar to each other as possible. For each magnitude bin, source terms are not stacked to avoid potential underestimation of stress drop (see Figure S3.2) (Figure 3.2(2)). The proposed method will be a reference for the results from all the other methods and studies included.

3.4.2.2 Spectral Ratio

The spectral ratio method solves for corner frequency of an earthquake by: first, calculating the ratio between the source terms of the target earthquake and an EGF event which should have a similar focal mechanism to the target (similar radiation pattern and being spatially close) and reasonably lower magnitude, then fitting the ratio to the ratio of Brune-shape source models between the target and EGF to obtain the corner frequency for both. The ratio is calculated using the spectra recorded on the same station, thus the path station information coupled in the recorded spectra is automatically canceled. Despite this, the stability of the method still relies on careful parameters and EGF selection. We use *Abercrombie (2014)* results of SAFOD targeted repeating clusters for comparison.

In the following analysis, we will comprehensively compare the performance of different methods using two types of seismic network data and frequency bands mentioned above to solve for both corner frequency and stress drop estimates. We will analyze individual earthquake estimates comparison, as well as the source parameters' scaling relationship to the magnitude.

3.5 Results

In this section, we solve for corner frequencies and stress drops of selected earthquakes with different combinations of seismic networks, methods and frequency bandwidths shown in Table 3.1. The frequency bandwidth for HRSN network is determined by the noise level criteria (2-60Hz with SNR>10), and for NCSN is consistent with AS2007 (2-20Hz). These results will be compared with AS2007, and *Abercrombie (2014)* who uses a wider frequency band than 2-60Hz.

3.5.1 Corner frequency

3.5.1.1 Magnitude dependence (scaling relationship)

The magnitude dependence of individual earthquake corner frequencies is displayed in Figure 3.3. For GOSC method, the median corner frequencies with different network and frequency band selection are generally higher than those from SNSS method (Table 3.1). Specifically, for 2-20Hz bandwidth cases, SNSS corner frequencies show a cutoff when they are inside the range of 80%-100% of the upper bound 20Hz, while the GOSC corner frequencies do not. Unlike the 2-20Hz bandwidth cases, 2-60Hz bandwidth exhibits high consistency between the SNSS and GOSC method though the GOSC median corner frequency is 1.12 times higher. We also do not observe obvious corner frequency cap for 2-60Hz bandwidth cases, but the scaling becomes weaker when the corner frequencies are close or higher than 40% of the upper bound.

3.5.1.2 Individual earthquake comparison

Another comparison focuses on individual earthquake corner frequencies among different networks, methods, bandwidths, and studies (Figure 3.4). Figure 3.4(1) shows that using SNSS method with 2-20Hz bandwidth, the HRSN corner frequencies are slightly higher than NCSN ones with a difference of a nearly constant factor (1.36 times according to Table 3.1), while in Figure 3.4(2) GOSC method leads to much less difference (1.13 times according to Table 3.1) and high consistency between the two networks. If we compare the corner frequencies using the same network (HRSN) and bandwidth (2-60Hz) but different methods (Figure 3.4(3)), there is a nearly perfect match for these common earthquakes with a small difference in absolute values (around 1.12 times according to Table 3.1), and the difference only enlarges for higher corner frequencies (>30Hz). In Figure 3.4(4), we use HRSN/GOSC/2-60Hz combination (#4) as a reference, and visualize the corner frequency ratio between other cases & studies and this combination. For HRSN/SNSS/2-20Hz (Combination #1) shown in blue squares, the corner frequency ratio is seemingly dropping when corner frequency exceeds 20Hz, while the GOSC case keeps a constant trend (red squares); AS2007 using SSS method seems to match the reference results, but their estimates become unstable when larger than 20Hz. As for the repeating clusters (T1: 5 earthquakes, T2: 5 earthquakes, T3: 4 earthquakes, totally 14 earthquakes) from Abercrombie (2014) using spectral ratio method (shown as non-square marks), the overall corner frequency is higher (2-3 times) than the reference case, which appears to be a constant factor of difference.

3.5.2 Stress drop

3.5.2.1 Magnitude dependence

Similar to 3.5.1.1, we investigate stress drop scaling with magnitude for common events in different cases, and attempt to calculate a scaling factor using a least-square-based linear fit approach (Figure 3.5). In order to show the change in the scaling relationship over magnitude, we calculate the scaling factor in different magnitude ranges (k1 for all earthquakes, k2 for Mw≥1.5 and k3 for Mw≥2.0). We do observe significant decrease in scaling when we use an Mw1.5 threshold comparing to that using no threshold for all the cases; comparing SNSS and GOSC methods, magnitude scaling relationship is much weaker for GOSC, and using 2-20Hz with GOSC results in almost no scaling with an Mw1.5 threshold (when Mw2.0 threshold is applied the scaling factor k2 becomes negative, which is caused by high scattering in a narrow magnitude range). For 2-60Hz cases, the scaling factors with different magnitude thresholds are highly similar, agreeing with the observation on corner frequencies.

3.5.2.2 Stress drop statistics

Stress drop measurements are usually very scattered due to uncertainties from many aspects, thus we display our stress drop scattering in different cases with the aforementioned 3 magnitude thresholds. Due to some extraordinarily high stress drop values, we apply a data quality threshold ($<10^6$ MPa) and limit the number of earthquakes from 465 to 409. Overall, it seems the absolute stress drop level does not vary over magnitude threshold selection (higher stress drops from GOSC method than SNSS method), but in the Mw1.5 threshold case the stress drops in these cases are closer to normal distribution than those using Mw2.0 threshold and no threshold. Moreover, the threshold selection does not change the scattering significantly: 2-20Hz cases have significantly larger standard deviation (STD) than 2-60Hz cases, and the GOSC method similarly shows higher scattering than the SNSS method.

3.6 Discussion

3.6.1 Selection of datasets, different seismic networks

Figure 3.4(1) and 3.4(2) have demonstrated the consistency of corner frequencies between HRSN and NCSN whichever method is applied in this study. Since the corner frequencies are solely resolved from the source term of earthquakes, whether the decomposition process can completely isolate the source term from other terms is a significant factor determining the uncertainties in the corner frequencies. It is known that the path and station terms can be inevitably absorbed into the source term (*Shearer et al., 2006a; Chen & Abercrombie, 2020*), which means that for different networks the source terms can be 'contaminated' by different information: HRSN are shallow borehole stations that avoid the sedimentary attenuation on the seismic wave ray paths and amplification at station locations, while NCSN stations contain both. Since the attenuation is very path-relying and site amplification is location-relying, for the NCSN the source term may contain more information in the path and station terms after spectral decomposition than the HRSN, and we could expect difference of source parameter estimation between the two networks. However, selecting a small fault patch and a small-aperture network can theoretically mitigate the bias on the NCSN, which potentially explains why the results from the two networks show general consistency in this study.

3.6.2 Selection of frequency bandwidths

Frequency bandwidth is an important factor that directly affects corner frequency uncertainties. Bandwidth is usually limited by the type of instruments and noise level. AS2007 only uses 1-20Hz considering the significant noise at higher frequencies from the sediment scattering, though the Nyquist sampling rate is 50Hz. The HRSN has 125Hz Nyquist, though our bandwidth ends at 60Hz due to the very strict SNR screening. This remarkably affects the resolvable magnitude range, since smaller earthquakes usually have higher corner frequencies.

Figure 3.3(A2) and 3.3(B2) show consistency in corner frequency patterns using 2-60Hz for HRSN, and magnitude scaling appears at around 40% (24Hz) of upper bound (around Mw2 in Figure 3.5) agreeing with *Chen & Abercrombie (2020)*. However, by using 2-20Hz, we do not observe a similar scaling pattern lower than the upper bound of 20Hz. This may suggest that the resolvability of corner frequencies is not necessarily limited to a small percentage of the upper bound, but can be extended to the upper bound, which is found in *Zhang et al. (2019)* using the same method. However, it should still be emphasized that corner frequencies larger than 20Hz can be better resolved using a 2-60Hz band than a 2-20Hz band, which is reflected in the magnitude scaling in Figure 3.5 (HRSN, SNSS, 2-20Hz vs 2-60Hz). In fact, the frequency bandwidth issue is partially due to the trade-off effect between corner frequency and attenuation as discussed in *Chen & Abercrombie (2020)*; another reason is that the real source spectra are not strictly Brune-shaped, and a narrow frequency band may magnify the difference between real spectra and Brune-shape spectra, causing corner frequency underestimation.

3.6.3 Selection of methods

The corner frequency estimates are obtained in different ways with different methods. In the Spectral Decomposition and Stacking based methods, they fundamentally rely on the ECS; the high one-to-one consistency of corner frequencies in Figure 3.4(3) suggests that using the same dataset and frequency bandwidth but different (though similar) methods may result in different ECSs, but do not actually contribute to any scattering in these estimates. However, the difference in ECSs will lead to inconsistent scaling relationship (Figure 3.4(4), Figure 3.5). Comparing the spectral decomposition and stacking method and spectral ratio method, we find significant difference on the corner frequency estimates of the SAFOD targeted clusters; a similar phenomenon was observed by *Shearer et al., (2019)* who compared spectral ratio and spectral decomposition and stacking methods in terms of individual corner frequencies, finding that Boatwright's source model outperforms than Brune's source model in spectral fitting. Boatright's model has a larger fall-off speed near corner frequency than Brune's model, and considering that the stacking process can smoothen the source spectra, Boatright's model may be more advantageous fitting to individual spectra while the Brune's model could be more suitable for stacking-based methods. It is also important to note that the comparison here not only involves the difference in the method basis, but also the difference in the frequency bandwidth.

As mentioned above, the GOSC method is introduced to avoid stacking process that may introduce artificial underestimation (Figure S3.2); however, its performance with 2-20Hz bandwidth is subject to discussion. In Figure 3.3(B1) and (B3) most of the corner frequencies have exceeded the upper bound of bandwidth and eventually lowered the Mw<1.5 magnitude scaling in Figure 3.5, while the SNSS method limits a large portion of corner frequencies to lower than the upper bound (Figure 3.3(A1) and (A3)). A possible explanation is that the SNSS method relies on the reference bin stress drop to control the ECS, and a lower stress drop can bring the overall stress drop level lower so that the stacked spectra can better fit to Brune model; in the GOSC method, stress drops in different magnitude bins are free to change as long as the ECSs in different bins are similar, therefore lower magnitude bins do not need to compensate for the misfits in larger magnitude bins causing overestimated low-magnitude stress drops. Both methods can still be further improved.

3.7 Conclusions

In this study, we design a series of tests on real data recorded by Parkfield local/regional networks with different methods and frequency bandwidth selections to investigate the uncertainties in the source parameters including corner frequency and stress drop.

1) We find that in real data situations, a wider frequency bandwidth can mitigate the uncertainties in the source parameters, and corner frequencies are thought resolvable as long as they are lower than the given upper bound;

2) Source parameters estimated using different seismic networks can show consistency with careful data selection, while the scattering cannot be remedied due to the discrepancies in attenuation and azimuths between the borehole and surface networks;

3) Different methods may show consistent source parameter estimates using a wider frequency bandwidth, but may also show disagreement when bandwidth is insufficient for resolving high corner frequencies; the Spectral ratio method may introduce higher corner frequencies than stacking-based methods.

3.8 Acknowledgement

We thank the USGS/HRSN/NCSN personnel who collect and distribute Parkfield dataset online for public use (visit the USGS at https://usgs.gov for further details). Data for this study come from the High-Resolution Seismic Network (HRSN) (doi:10.7932/HRSN, operated by the UC Berkeley Seismological Laboratory), and Northern California Seismic Network (contributed by U.S. Geological Survey) which

is archived at the Northern California Earthquake Data Center (NCEDC), doi:10.7932/NCEDC. Waveform data, metadata, or data products for this study were accessed through the Northern California Earthquake Data Center (NCEDC), doi:10.7932/NCEDC.

References

Abercrombie, R. E. (2000). Crustal attenuation and site effects at Parkfield, California. *Journal of Geophysical Research: Solid Earth*, *105*(3), 6277–6286. https://doi.org/10.1029/1999jb900425

Abercrombie, Rachel E. (2014). Stress drops of repeating earthquakes on the San Andreas Fault at Parkfield. *Geophysical Research Letters*, *41*(24), 8784–8791. https://doi.org/10.1002/2014GL062079

Abercrombie, Rachel E. (2015). Investigating uncertainties in empirical Green's function analysis of earthquake source parameters. *Journal of Geophysical Research: Solid Earth*, *120*(6), 4263–4277. https://doi.org/10.1002/2015JB011984

Allmann, B. P., & Shearer, P. M. (2007). Spatial and temporal stress drop variations in small earthquakes near Parkfield, California. *Journal of Geophysical Research: Solid Earth*, *112*(4), 1–17. https://doi.org/10.1029/2006JB004395

Bard, P.-Y., & Bouchon, M. (1985). The two-dimensional resonance of sediment-filled valleys. *Bulletin of the Seismological Society of America*, *75*(2), 519–541. https://doi.org/10.1785/BSSA0750020519

Brune, J. N. (1970). Tectonic stress and the spectra of seismic shear waves from earthquakes. *Journal of Geophysical Research*, *75*(26), 4997–5009. https://doi.org/10.1029/JB075i026p04997

Chen, X., & Abercrombie, R. E. (2020). Improved approach for stress drop estimation and its application to an induced earthquake sequence in Oklahoma. *Geophysical Journal International*, *223*(1), 233–253. https://doi.org/10.1093/gji/ggaa316

Chen, X., & Shearer, P. M. (2013). California foreshock sequences suggest aseismic triggering process. *Geophysical Research Letters*, *40*(11), 2602–2607. https://doi.org/10.1002/grl.50444

Eshelby JD. (1957). The determination of the elastic field of an ellipsoidal inclusion, and related problems. *Proceedings of the Royal Society of London. Series A. Mathematical and Physical Sciences*, *241*(1226), 376–396. https://doi.org/10.1098/rspa.1957.0133

Harris, R. A., & Segall, P. (1987). Detection of a locked zone at depth on the Parkfield, California, segment of the San Andreas fault (USA). *Journal of Geophysical Research*, *92*(B8), 7945–7962. https://doi.org/10.1029/JB092iB08p07945

Ide, S., & Beroza, G. C. (2001). Does apparent stress vary with earthquake size? *Geophysical Research Letters*, *28*(17), 3349–3352. https://doi.org/10.1029/2001GL013106

Kaneko, Y., & Shearer, P. M. (2014). Seismic source spectra and estimated stress drop derived from cohesive-zone models of circular subshear rupture. *Geophysical Journal International*, *197*(2), 1002–1015. https://doi.org/10.1093/gji/ggu030

Kaneko, Y., & Shearer, P. M. (2015). Variability of seismic source spectra, estimated stress drop, and radiated energy, derived from cohesive-zone models of symmetrical and asymmetrical circular and elliptical ruptures. *Journal of Geophysical Research: Solid Earth*, *120*(2), 1053–1079. https://doi.org/10.1002/2014JB011642

Madariaga, R. (1976). Dynamics of an expanding circular fault. *Bulletin of the Seismological Society of America*, *66*(3), 639–666. Retrieved from http://bssa.geoscienceworld.org/content/66/3/639.abstract

Ruhl, C. J., Abercrombie, R. E., & Smith, K. D. (2017). Spatiotemporal Variation of Stress Drop During the 2008 Mogul, Nevada, Earthquake Swarm. *Journal of Geophysical Research: Solid Earth*, *122*(10), 8163–8180. https://doi.org/10.1002/2017JB014601

Shearer, P. M., Prieto, G. A., & Hauksson, E. (2006). Comprehensive analysis of earthquake source spectra in southern California. *Journal of Geophysical Research: Solid Earth*, *111*(6), 1–21. https://doi.org/10.1029/2005JB003979

Shearer, P. M., Abercrombie, R. E., Trugman, D. T., & Wang, W. (2019). Comparing EGF Methods for Estimating Corner Frequency and Stress Drop From P Wave Spectra. *Journal of Geophysical Research: Solid Earth*, *124*(4). https://doi.org/10.1029/2018JB016957

Storn, R., & Price, K. (1997). Differential Evolution – A Simple and Efficient Heuristic for global Optimization over Continuous Spaces. *Journal of Global Optimization*, *11*(4), 341–359. https://doi.org/10.1023/A:1008202821328

Trugman, D. T., & Shearer, P. M. (2017). Application of an improved spectral decomposition method to examine earthquake source scaling in Southern California. *Journal of Geophysical Research: Solid Earth*, *122*(4), 2890–2910. https://doi.org/10.1002/2017JB013971

Viegas, G., Abercrombie, R. E., & Kim, W. Y. (2010). The 2002 M5 Au Sable Forks, NY, earthquake sequence: Source scaling relationships and energy budget. *Journal of Geophysical Research: Solid Earth*, *115*(7), 1–20. https://doi.org/10.1029/2009JB006799

Waldhauser, F. (2009). Near-real-time double-difference event location using long-term seismic archives, with application to northern California. *Bulletin of the Seismological Society of America*, *99*(5), 2736–2748. https://doi.org/10.1785/0120080294

Waldhauser, F., & Schaff, D. P. (2008). Large-scale relocation of two decades of Northern California seismicity using cross-correlation and double-difference methods. *Journal of Geophysical Research: Solid Earth*, *113*(8), 1–15. https://doi.org/10.1029/2007JB005479

Zhang, J., Chen, X., & Abercrombie, R. E. (2019). Resolving the spatiotemporal variability of small earthquake source parameters at Parkfield and their relationship with 2004M6 Parkfield earthquake. In *AGU Fall Meeting Abstracts* (Vol. 2019, pp. S52C-05).

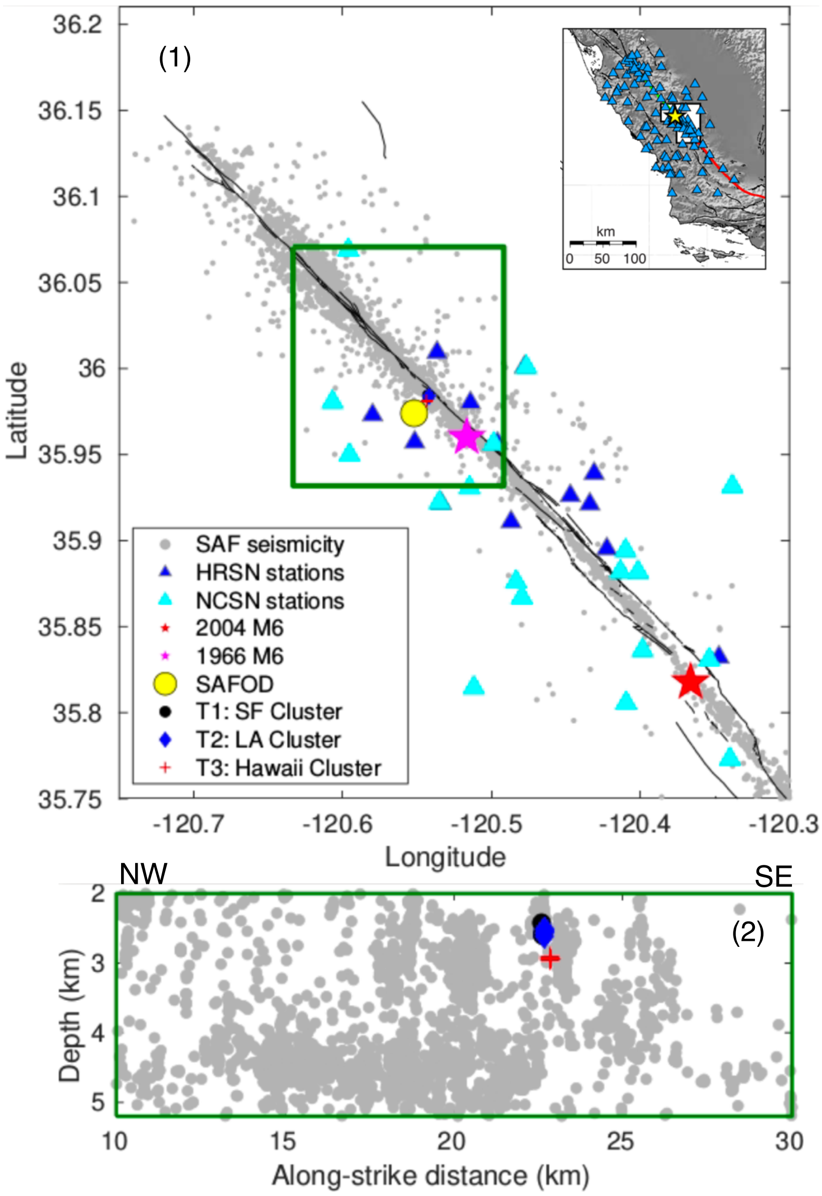

Figure 3.1: Geometry of studied area. (1): Map view. Grey dots show total seismicity in the Parkfield area Double-Difference catalog (WNC catalog), magenta/red stars are the 1966 M6/2004 M6 earthquakes, yellow circle shows the location of SAFOD, and dark blue/light blue represent HRSN stations and NCSN stations USED in this study, respectively. Dark green block marks the events used in this study covering ~20km along the SAF at Parkfield and ~3.2km in depth. Mini-plot is from *Allmann and Shearer (2007)* showing all NCSN stations (Blue). (2) Cross-section view of earthquakes in the dark green area along SAF. Blue circles, blue diamonds and red pluses represent SAFOD targeted clusters T1, T2 and T3.

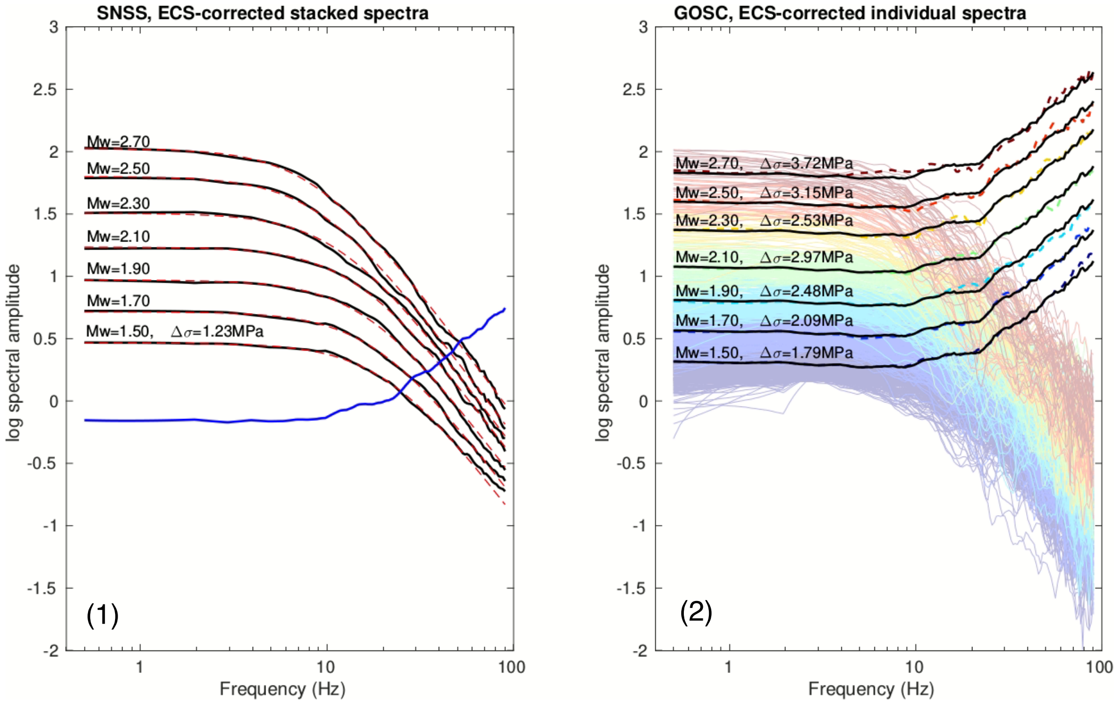

Figure 3.2: ECS-corrected spectra from SNSS and GOSC methods, HRSN network with 2-60Hz frequency band. (1) ECS-corrected stacked spectra shown as black solid curve in each magnitude bin, and Brune-fitting shown in red dashed curve in each magnitude bin. Blue curve represents the ECS; (2) ECS-corrected individual spectra shown in rainbow colors (blue-red: Mw1.50-Mw2.70). Rainbow dashed curves are the median ECSs in different bins, and the black curves are the median of rainbow ECSs and are identical (for comparison with per-bin ECSs).

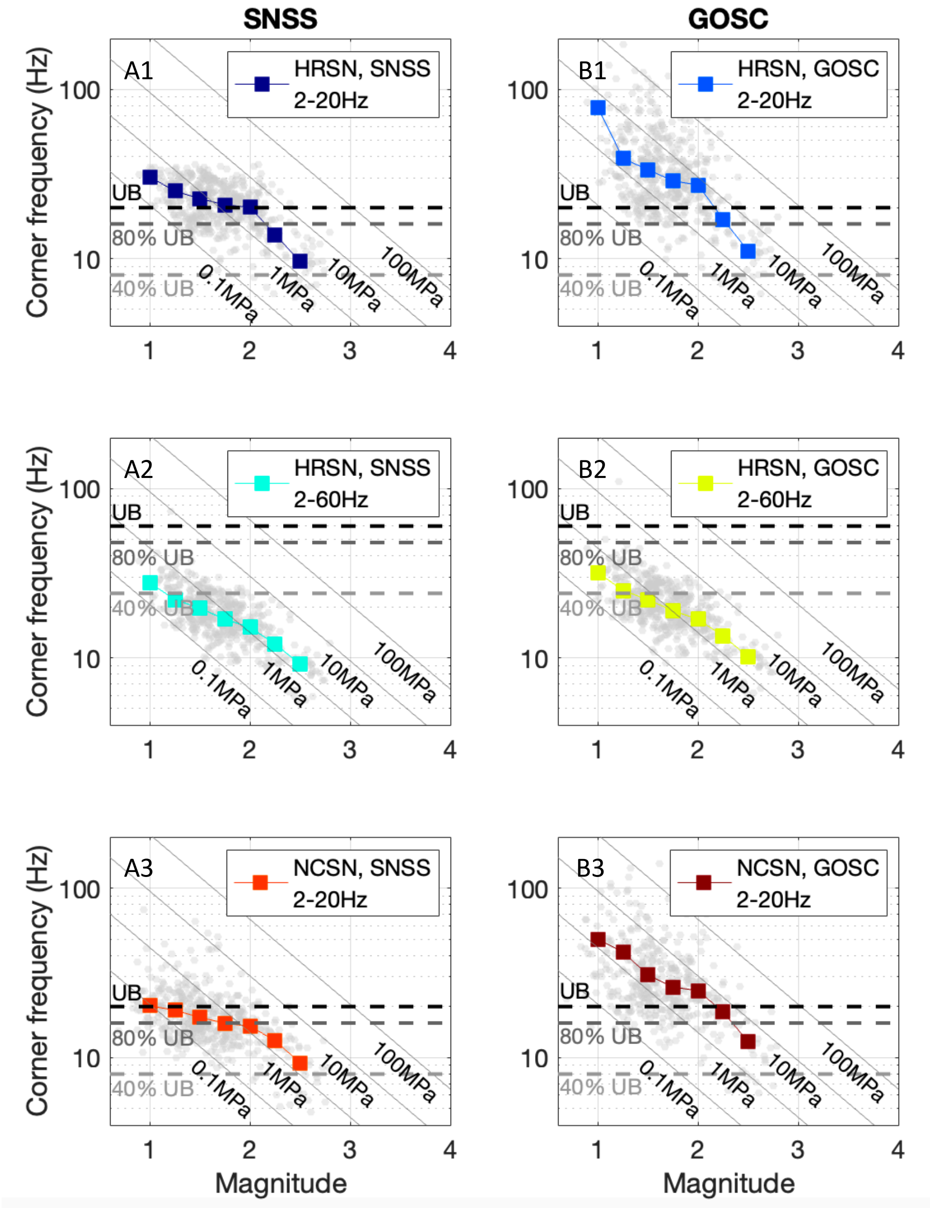

Figure 3.3: Corner frequency versus magnitude for different fc bands, methods and datasets. A1-A3: SNSS results, using HRSN & 2-20Hz, HRSN & 2-60Hz and NCSN & 2-20Hz, respectively. B1-B3: GOSC results, using HRSN & 2-20Hz, HRSN & 2-60Hz and NCSN & 2-20Hz, respectively. Grey dots represent individual event results and colored blocks stand for the median of corner frequency calculated in magnitude windows of [-0.25,0.25] every 0.25 from 1 to 2.5. Dashed black horizontal line in each subplot represents the upper frequency bound (UB) in each case (20Hz for row 1&3 and 60Hz for row 2). Shallower grey dashed lines represent 80% and 40% of upper bound in each case according to resolvable corner frequency range in *Chen & Abercrombie (2020)*.

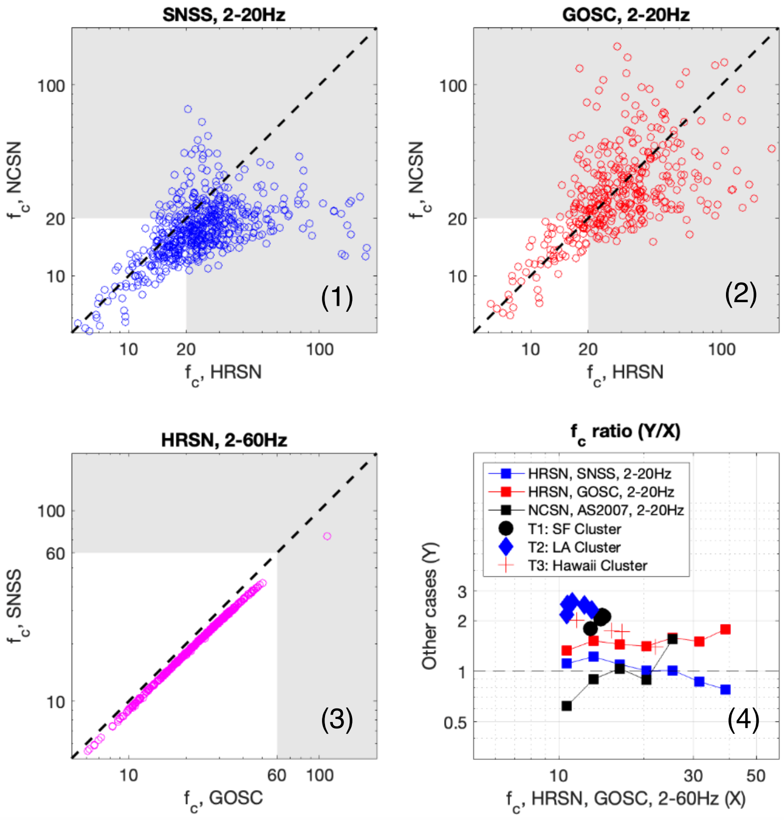

Figure 3.4: One-to-one corner frequency comparison between studies using different datasets and methods. (1) This study, SNSS method, HRSN 2-20Hz versus NCSN 2-20Hz (blue dots), dashed line shows where the two results have the same corner frequencies; (2) This study, GOSC, HRSN 2-20Hz versus NCSN 2-20Hz, dashed line showing the same as (1); (3) This study, HRSN, GOSC 2-60Hz versus SNSS 2-60Hz, dashed line showing the same as (1); (4) Corner frequency ratio between this study HRSN, GOSC 2-60Hz and: 1. This study HRSN, SNSS 2-20Hz (blue square), 2. This study, HRSN, GOSC 2-20Hz, 3. NCSN, SSS 2-20Hz, and 4. *Abercrombie (2014)*, Spectral Ratio, SAFOD targeted repeating sequences T1 (black circles), T2 (blue diamonds) and T3 (red pluses). Dashed line indicates where the ratio is 1. Squares are calculated as median values of individual earthquake ratios in log corner frequency windows of X-axis values.

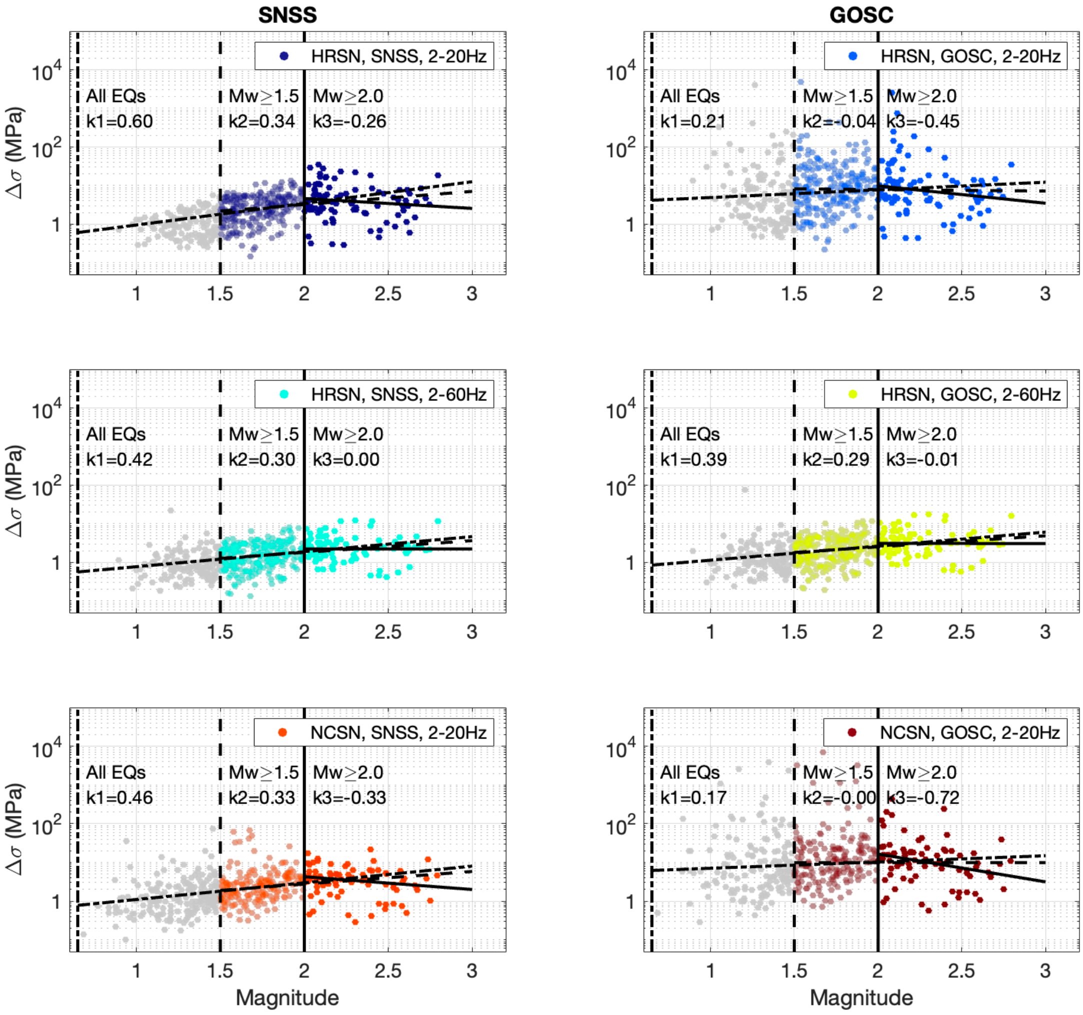

Figure 3.5: Stress drop magnitude scaling for all cases. In each case, grey dots are the results of all events, while the transparent colored dots show Mw≥1.5 events and solid-color dots show Mw≥2.0 events. The black dash-dot line is the linear fit to the grey dots (all events) with slope k1, the black dashed line is the linear fit to the transparent-color dots (M≥1.5 events) with slope k2, and the black solid line is the linear fit to the solid-color dots (M≥2 events) with slope k3.

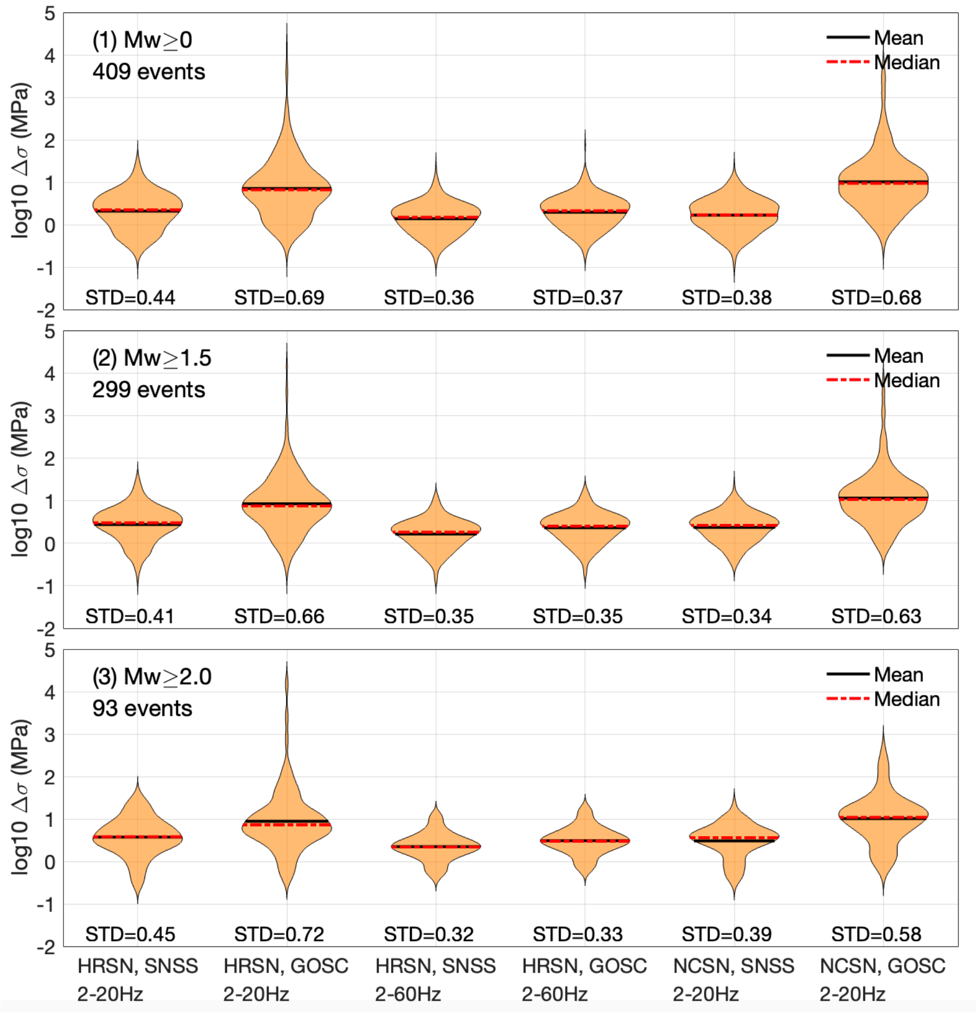

Figure 3.6: Violin plots showing log10 stress drop distribution for each case after removing extreme outliers (stress drop larger than 106 MPa). Black bars and red dashed lines represent the mean and median log10 stress drop in each case. (1), (2) and (3) show the stress drop distribution when a magnitude threshold is placed (1: All earthquakes, 2: Mw ≥ 1.5, 3: Mw ≥ 2.0).

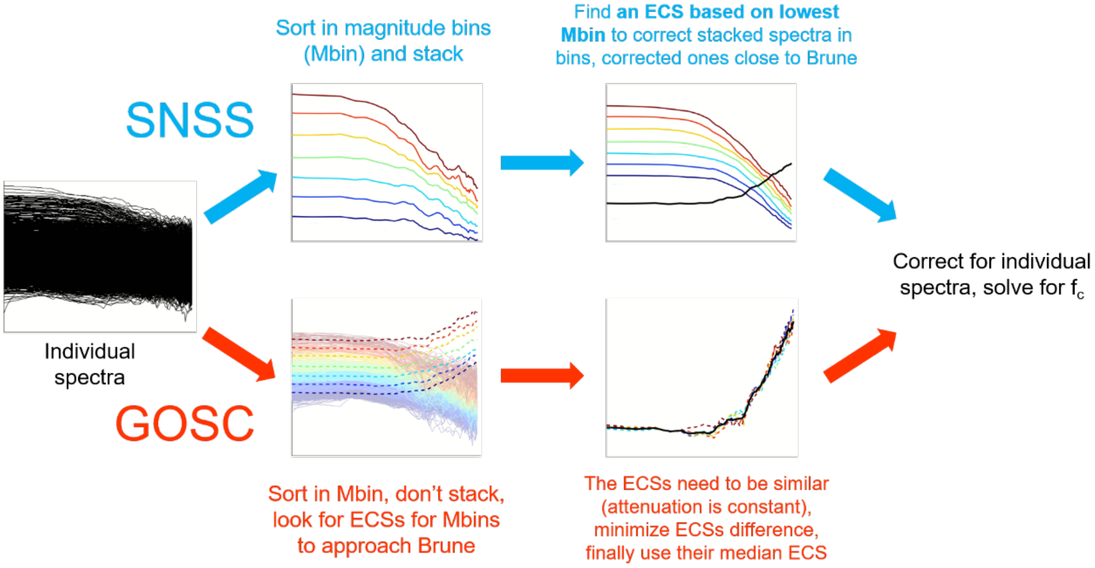

Figure S3.1: Workflow comparison between SNSS and GOSC methods. The difference is how the ECS is generated.

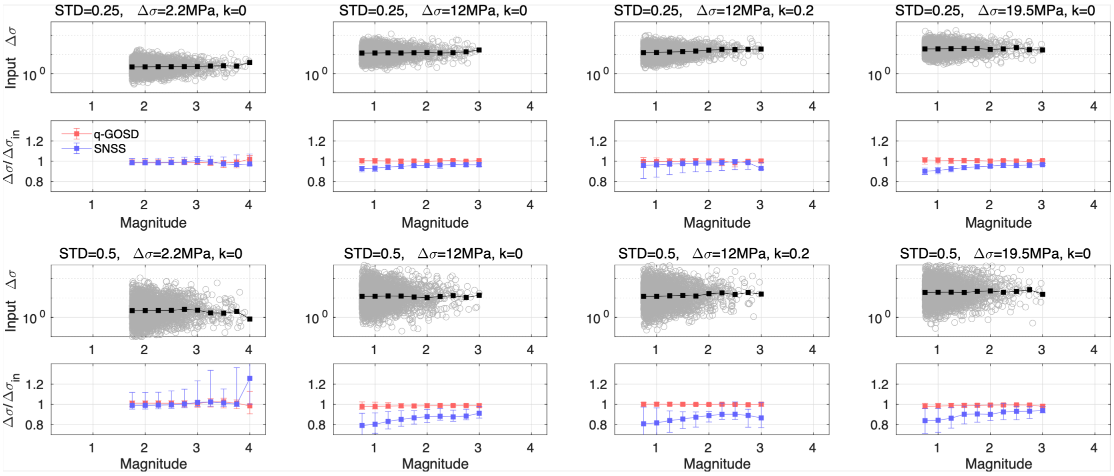

Figure S3.2: Synthetic tests with different input stress drop levels and different stress drop scattering levels (standard deviation, STD), similar to that in *Chen & Abercrombie (2020)*. Columns represent different cases: Column 1. Low stress drop (2.2MPa), no input magnitude scaling; Column 2. Intermediate stress drop (12MPa), no input magnitude scaling; 3. Intermediate stress drop (12MPa), with input magnitude scaling k=0.2; 4. High stress drop (19.5MPa), no input magnitude scaling. For each case, 200 earthquakes are randomly generated with magnitude following G-R law and Brune-shape spectra; inversion is performed 20 times and 200 earthquakes parameters are different in each repetition, therefore totally 4000 earthquakes are included for the statistics. Odd rows show input stress drops VS. magnitude for the 4000 earthquakes, and even rows show the median stress drop recovery from input to output using the GOSC (red) and SNSS (blue) methods. Row 1 and 2 use low stress drop scattering (STD=0.25) while row 3 and 4 use higher scattering (STD=0.5). The synthetic test shows that for large stress drops and large scattering input, there is artificial stress drop underestimation using the SNSS method compared to GOSC method that nearly perfectly recovered the stress drops.

Combination #	Seismic network	Method	Frequency bandwidth	Median f_c (Hz)	Median $\Delta\sigma$ (MPa)
1	HRSN	SNSS	2-20Hz	24.57	3.39
2	HRSN	GOSC	2-20Hz	38.17	13.42
3	HRSN	SNSS	2-60Hz	20.67	1.44
4	HRSN	GOSC	2-60Hz	23.24	2.02
5	NCSN	SNSS	2-20Hz	18.04	1.96
6	NCSN	GOSC	2-20Hz	33.73	16.62

Table 3.1: Combination of seismic network, method, and frequency bandwidth to solve for individual earthquake source parameters.

Chapter 4 High-resolution source mechanism analysis of microseismicity during hydraulic fracturing

4.1 Abstract

Understanding the triggering and source processes of microseismic events is important for unconventional oil & gas production and assessing the potential hazard. We develop a workflow to detect/locate microseismicity, obtain source parameters, and analyze their spatiotemporal patterns to better understand the source mechanism. We apply a double-difference based method to obtain high-resolution event locations, and introduce an improved spectral decomposition and stacking approach to solve for the corner frequency and source radius of the microseismic events, and attempt to measure the relative stress change associated with these events. Our results find that the source radii of these microseismic events are nearly independent of event size, which differs from natural earthquakes, suggesting different source mechanisms. We observe spatial migration patterns of microseismic events away from the fracturing points with diffusivity of 0.6-0.8 m^2/s, and gradual change of event magnitude and stress change with distance from fracturing point. These observations suggest the influence of fluid on event occurrence and source processes during hydraulic fracturing.

4.2 Introduction

During unconventional oil & gas exploration, such as shale gas exploration, monitoring the microseismicity produced from hydraulic fracturing is important for production rate control and safety assessment, because these microseismic events provide an effective approach to delineate the spatiotemporal fracture development *(Fischer et al., 2008; Maxwell et al., 2010; Sasaki, 1998)*. To study the microseismicity, accurate detection and location of microseismic events during the fracturing stages are required. Since the locations of microseismic events are determined from the observed arrival times on downhole geophones, an accurate velocity model is important for the final locations *(Thurber, 1985)*. The velocity model can be obtained from sonic log data and calibrated by the perforation shot information including locations and arrival times *(Pei et al., 2009; Warpinski et al., 2003; Zhang et al., 2016)*. The calibrated velocity model from perforation shots can help improve the location of microseismic events *(Bardainne & Gaucher, 2010)*.

For microseismic events, it has long been concerned whether they are self-similar (whether stress drop is magnitude independent) *(Aki, 1967)*. Self-similarity has been found among natural earthquakes (e.g., *Allmann & Shearer, 2009*) and induced earthquakes (e.g., *Wu et al., 2018*), while microseismic events with much lower magnitudes (usually below Mw0), are mostly found to be non-self-similar (e.g., *Urbancic & Young, 1993; Viegas et al., 2015*). It remains unclear whether the inconsistency is from the difference in faulting mechanism: natural or induced earthquakes are mostly shear failure, while the microseismic events are a combination of tensile and shear failure *(van der Baan et al., 2013; Maxwell, 2011)*. The tensile failure events, generally associated with non-Double-Couple mechanism, are often observed during hydraulic fracturing *(Baig & Urbancic, 2010; Song & Toksöz, 2011; Vavryčuk, 2001)*. Based on the far-field spectrum of tensile failure source derived by

Walter & Brune (1993), *Eaton et al. (2014)* obtained non-self-similar relationship between source radius and seismic moment. These may suggest that the source process of microseismic events differs from natural and induced earthquakes.

In this study, we aim at estimating source parameters (e.g., corner frequency and source radius) of microseismic events that occurred during hydraulic fracturing in a shale gas exploration project located in Texas, USA, facilitated by very-high sampling rate downhole geophone seismic data. To study the spatiotemporal variation of source parameters, following the detailed workflow in Figure 4.1, we detect microseismic events from raw seismic data, derive a P-wave velocity model for the studied area following *Zhang et al. (2016)*, and locate the detected events with a double-difference based approach. Then we perform detailed source parameter analysis based on an improved approach. Finally, we discuss and interpret the magnitude dependence and spatiotemporal patterns of source parameters.

4.3 Data and survey information

The hydraulic fracturing survey consists of multiple treatment wells and monitoring wells for fracture stimulation and microseismic monitoring. The survey area is approximately 5km by 2.5km, and is surrounded by numerous logging wells with sonic logs (Figure 4.2). In this research, the available dataset includes complete waveform data and metadata for 1 treatment wells (well A) and 4 monitoring wells (wells B & C are vertical wells, and D & E are horizontal wells).

4.3.1 Operation and observation system

The treatment well includes multiple completion/production stages (each with a perforation stage and a fracturing stage) lasting over a week and progressively moving along the horizontal part of the well. For each stage, multiple explosive shots are performed in less than 10 minutes during a perforation stage, followed by a fracturing stage where liquid is continuously pumped into perforated rock for less than 2 hours.

The monitoring wells include downhole geophone arrays to monitor both the perforation stages and the fracturing stages continuously. Each well contains a downhole array with either 12 (horizontal) or 20 (vertical) sensors at 2000Hz sampling rates. Our dataset includes 4 fracturing and perforation stages (Stage S1/S2/S3/S4); only Stage S4 is recorded by all 4 monitoring wells, and Stage S1/S2/S3 are only recorded by monitoring wells D and E. Stage S4 has 20 perforation shots, with 11 having visible P wave arrivals. The whole observatory system covers a depth range of around 1500-3100 meters.

4.3.2 Logging well and 1D velocity model building

Location of detected microseismic events requires an accurate velocity model. Shale formation can be approximated with a 1-D velocity model (e.g., *Warpinski et al., 2003*); a rough 1-D velocity model can be first calculated from sonic velocity measured in logging wells, then calibrated using perforation shot arrival times and location via travel-time based inversion approaches (*Zhang et al., 2016).* Since we only observe arrival time instead of travel time, the origin time of perforation shot is required; however, the listed origin time is usually inaccurate because the actual event does not coincide with the explosive shot. *Guo & Zhang (2017)* and *Zhang et al. (2016)* use station pairs to cancel out the origin time of events to mitigate uncertainties in the inversion problem. The optimal velocity model should be associated with minimized misfits between theoretical and observed station-pair travel time differences. The 1D velocity inversion problem is usually high-dimensional and almost impossible to be solved by grid-search, therefore, global optimization methods such as Simulated Annealing (SA) algorithm *(Pei et al., 2009)* and Differential Evolution (DE) algorithm *(Zhang et al., 2016)* are used to obtain a multi-layer 1D velocity model by minimizing the misfits.

In this study, the logging wells are distributed in a larger area than the survey area, and well 4 is in closest vicinity (Figure 4.1a). Ideally, well 4 is the best candidate to build the initial model; however, its sonic log is incomplete in the targeted depth range, therefore we utilize the nearest 4 logging wells (wells 2/4/5/15) and apply distance-dependent averaging of sonic velocities in these wells weighted by reciprocal of distance to obtain an initial 1D velocity model (Figure 4.1b). We follow the practice of *Zhang et al. (2016)* to calibrate the initial 1D model using perforation shots during stage S4 (the only stage recorded by all four monitoring wells): we first pick the arrival times of 11 perforation shots and calculate the theoretical P wave travel time differences between sensor pairs in each monitoring well, then we utilize the initial velocity model to invert for a P wave velocity model with DE method (Figure 4.3). To ensure the stability of the inversion process, we run the DE inversion 10 times with the same input data, and obtain the final velocity model using the median of the models from the 10 runs. We also reduce the number of perforation shots used in the inversion to 4/6/8 shots and check if the inverted model changes significantly, Figure S4.1 shows that reduced number of perforation shots obtain very similar outcomes, indicating the inverted velocity model is robust. The derived model preserves a lower P velocity (2.2 km/s) at the shale depth in the initial model from sonic logs. The inverted value (~2.2 km/s) is lower than the starting value at the shale depth range (~ 4km/s), but it is within the P wave velocity of shale layer (between 2 and 3.8 km/s) (*Awang et al., 2017)*, and the shale velocity in the initial model is closer to the P wave velocity of sandstone (>4.0km/s). It should be mentioned that the derived velocity model is subject to uncertainties related to anisotropy, which has been observed and estimated inside shale *(Wang & Li, 2017)*, and we do not consider a tilted 1-D model.

4.4 Microseismic event detection and location

We first detect microseismic events from the raw seismic data for fracturing Stages S1/S2/S3/S4; then the inverted velocity model in Figure 4.3 is applied to microseismic location with a double-difference based approach.

4.4.1 Microseismic event detection

The Short-Time Averaging and Long-Time Averaging ratio (STA/LTA) method *(Allen, 1978, 1982)* has been widely applied to detecting earthquake phases from continuous seismic waveforms with improvements *(Ross & Ben-Zion, 2014; Song et al., 2010; Vaezi & van der Baan, 2015; Withers et al., 1998)*. Several parameters control the performance of the algorithm: long-time and short-time window length, triggering threshold, detriggering threshold and minimum event duration, which need to be carefully chosen *(Trnkoczy, 2002)*. Besides, band-pass filtering (or low-pass) needs to be applied to raw waveforms to remove high-frequency spikes that can cause fake detection.

In this survey, we apply the STA/LTA method to detect microseismic events from the raw seismic data of the 4 stages recorded by sensor arrays in the 4 monitoring wells. Figure S4.2 shows an example of raw waveforms with visible high Signal-to-Noise Ratio (SNR) events. Considering the high-frequency contents of microseismic events, we set the parameters as:

- short-time window length: 0.01s
- long-time window length: 0.1s
- triggering threshold: 3
- detriggering threshold: 1.5
- minimum event duration: 0.02s

To associate detections on different sensors to individual events and remove false detections, we use a moving window (0.1s long, with 0.05s interval) to scan detections from all traces, and use the following criteria to retain valid detections:

1. Detections are found on at least 7 traces in each monitoring well;
2. Detections are found from at least 2 monitoring wells (each with more than 7 traces);
3. Within each monitoring well, the median cross-correlation coefficient for the same event between different sensor pairs is larger than 0.85, considering sensors are closely located and waveforms of the same event should be similar.

To choose an appropriate band-pass filter, we first perform detection to raw data and obtained some preliminary events, then visualize their frequency contents via spectrograms (Figure S4.3). It is found that most energy is approximately distributed between 20Hz and 90Hz for the majority of the detections, so we apply a 20-90 Hz bandpass filter for the detection.

With these criteria, we detect 354/158/146/536 events with P wave phases in Stage S1/S2/S3/S4, respectively. We also detect other events outside these four stages, which may belong to other completion/production stages that we do not have relevant metadata information. It is important to note that some smaller events may be missed during the detection process.

4.4.2 Microseismic event location

The waveforms of microseismic events can be backpropagated to their source locations with the inverted velocity model. This process requires joint inversion of the origin time of the microseismic events, which trades off with the actual event locations and further introduces uncertainties. An inaccurate velocity model can also lead to errors in event locations. The traditional Double-difference (DD) approach *(Waldhauser & Ellsworth, 2000; Zhang & Thurber, 2003)* pairs collocated events in space to mitigate the uncertainties introduced by velocity model. The Double-pair Double-difference method (Double-pair DD, *Guo & Zhang, 2017*), developed based on the traditional DD method, further pairs stations to remove the origin time of events to improve the accuracy of event location and velocity tomography.

The double-pair approach is implemented using the arrival time differences between stations for each event. We obtain the arrival time differences by cross-correlating (CC) event waveforms recorded on station pairs, and only pairs with CC>0.6 are used. As a comparison, we also calculate arrival time differences from manual picks of the events. Figure S4.4 shows an example of waveform difference between a station pair. Both datasets (CC and manual picking-derived differential times) are inverted for event locations. Figure S4.5 clearly shows that the CC locations are more spatially compact than those from manual picks, therefore CC locations are preferred.

The double-pair location is performed for all the 4 stages (Table 1), and the spatial distribution of microseismic events colored by event origin time are shown in Figure 4.4. We do not obtain locations for all events due to data quality. Table 1 shows that stage S4 has the largest number of double pairs, while stages S1 and S2 have much fewer available double pairs. Stages S1 and S2 are located outside the array aperture of the monitoring wells, while stages S3 and S4 have better coverage. Stage S4 is the only stage recorded by all the four monitoring wells. Events in Stage S1 and S2 are less compact compared to those in Stage S3 and S4, which is likely because of the bad azimuthal coverage. The biased azimuths, combined with limited depth coverage of stations (most stations are at the depth of or shallower than the microseismic events), also cause large uncertainties in depth location for the Stage S1 and S2 than Stage S3 and S4. Events from stage S4 are symmetrically distributed around the treatment well, potentially benefitting from good station coverage.

4.5 Microseismic source properties

Due to lack of instrument gain information, we cannot obtain absolute seismic moments for individual events, and can only obtain relative magnitudes/seismic moments. Since the stress drops will be computed using relative moments, they do not represent the real stress drops; instead, we name them 'relative stress change' ($\Delta\sigma_r$). Our focus is the relative spatiotemporal evolutions of source parameters (source radius, relative stress change), and the scaling relationship between source parameters and relative magnitude.

4.5.1 Methods

Microseismic source radius is related to the corner frequency f_c of an event through *(Brune, 1970; Madariaga, 1976)*:

$$r = k\frac{\beta}{f_c} \tag{4.1}$$

where β is shear wave velocity (assumed proportional to rupture velocity) and *k* is a constant that depends on rupture model assumptions. We apply a commonly used *k* value of 0.32 (*Abercrombie, 1995; Shearer et al., 2006a; Allmann and Shearer, 2007; Abercrombie, 2014; Chen and Abercrombie, 2020*) assuming circular crack model, in which rupture velocity is 0.9 times of shear velocity *(Madariaga, 1976)*. Corner frequency can be estimated by fitting the source spectrum of an event to the widely used Brune's source model *(Brune, 1970)*:

$$s(f) = \frac{\mathrm{M_{0r}}}{1+\left(\frac{f}{f_c}\right)^n} \tag{4.2}$$

where *n* is the high-frequency fall-off rate, and we use *n=2* (ω^{-2} model); M_{0r} represents the relative seismic moment. The relative earthquake stress drop ($\Delta\sigma_r$) can then be calculated from the seismic moment and the source radius following *(Eshelby, 1957)*:

$$\Delta\sigma_r = \frac{7}{16}\left(\frac{M_{0\mathrm{r}}}{r^3}\right) = M_{0\mathrm{r}}\left(\frac{f_c}{0.42\beta}\right)^3 \tag{4.3}$$

For source parameter analysis, we only use S-wave displacement spectra with minimum SNR>2 between 80Hz and 700Hz. Each event included in the spectral analysis should be recorded by at least 5 sensors. The shear velocity is calculated from the final P-wave velocity model with a constant Vp/Vs ratio of 1.7 *(Qin, 2013; Sondergeld et al., 2000)*. The relative magnitudes are calculated from 80-120Hz average (low-frequency plateau that is proportional to seismic moment) of S-wave displacement spectra.

To get source spectra for microseismic events, the first step is to use the Spectral Decomposition method *(Shearer et al., 2006)* to iteratively separate source, propagation and instrument/site terms denoted in *Aki and Richards (1980)*. A homogeneous attenuation structure is assumed during this process. The propagation term includes distance-based attenuation. During the decomposition process, common propagation terms to all the events can be absorbed into source term.

The second step is to correct for common propagation terms to all events from the source term. Different methods have been proposed to obtain an Empirical Correction Spectrum (ECS). *Shearer et al. (2006a)* obtained the ECS by minimizing the difference between stacked source terms for different magnitude bins and predicted Brune-shape spectra assuming the same average stress drop (self-similarity). A similar practice is used by *Trugman & Shearer (2017)*, who simultaneously solve for a scaling factor of stress drop with magnitude to obtain the ECS using stacked spectra for different magnitude bins. *Chen & Abercrombie (2020)* found that assumptions of stress drop scaling can lead to biases in ECS, and developed an approach that does not make any assumptions of stress drop scaling.

In this study, we further improve the method in *Chen & Abercrombie (2020)*: we first sort events into magnitude bins and assume the stress drops for events in a single magnitude bin are the same, but different magnitude bins can have different stress drops and different events can have different ECSs; then we apply the Differential Evolution method *(Storn & Price, 1997)*, which is a global optimization approach, to solve for best-fitting stress drops for all magnitude bins by minimizing the difference among ECSs for different events (we assume the ECS should be similar among different events due to the small survey area).

After obtaining the ECS, the last step is to remove ECS from individual source terms, and obtain corner frequency (and source radius) estimates by fitting the Brune model (equation 4.2). Since these methods rely on the quantity of data, we process events in all the four stages together, therefore, temporal changes of attenuation are not considered. Based on previous studies, temporal changes of attenuation usually have very small influence on source parameter estimations *(Ruhl et al., 2017; Uchide et al., 2014)*. For stage S4, we compare these results with source parameters from inverting only this stage, and do not see systematic biases (Figure S4.6).

The seismic moment is proportional to low-frequency amplitude of source spectrum. We obtain the relative magnitude M_r and relative seismic moment (M_{0r}) based on the average low-frequency amplitudes of event spectra (Figure S4.7) between 80Hz and 120Hz (the influence of attenuation is negligible at this frequency band for these microseismic events). After obtaining the relative seismic moment, we use equation 4.3 to calculate relative stress change ($\Delta\sigma_r$) based on corner frequency and relative moment.

4.5.2 Source parameter results

We obtain source parameters results such as relative magnitude, corner frequency and source radius for 1018 events from all the four stages. We analyze the magnitude statistics, spatial distribution of magnitude and source radius, as well as magnitude dependence of corner frequency, in order to understand the mechanism of hydraulic-fracturing-related microseismic events.

4.5.2.1 Magnitude statistics and spatial dependence of source parameters

We set the lowest relative magnitude as 0, and obtain relative magnitudes for events of all the 4 stages, which range from 0 to 2.72 with a median value of 1.06 (Figure S4.8). Figure 4.5 shows an overview of the source parameter results. Based on the magnitude histograms, only stage S1 and S4 shows some agreement with Gutenberg-Richter law (GR), while the other two stages show deviation from GR relationship. Deviations from GR relationship has been reported for some induced sequences (e.g., *Skoumal et al., 2015*), however, this could also be due to incomplete detection as a result of azimuthal coverage. All four stages have similar maximum relative magnitude, $max(M_r)$~2.5. The source radius has a median value of 1.28 m with 25th and 75th percentiles of 0.92m and 1.58m, which is consistent with the range of source radius for microseismic events during hydraulic fracturing (e.g., *Huang et al., 2017; Urbancic & Young, 1993*). Based on the source radius, the absolute magnitude of these events likely falls within Mw of -2.3 to -1.4 *(Urbancic & Young, 1993)*, however, due to lack of instrument information, we cannot verify the absolute magnitude range.

There are no clear spatial patterns of relative magnitude and source radius for stages S1 and S2. For stage S3 and S4, there is a tendency for lower magnitude and smaller source radius events to cluster near the injection point, and relatively larger events tend to occur further away (Figure 4.6). Such a trend has been reported in previous studies on microseismic events, which is interpreted to be related to stress distributions in the injection zone *(Yu et al., 2020)*. On the other hand, attenuation could change with distance from the fracking point (e.g., *Barthwal et al., 2019*). Since the source radius is calculated from corner frequency, which could tradeoff with attenuation, the spatial patterns of source radius could be influenced by attenuation.

4.5.2.2 Magnitude dependence of source parameters

We evaluate the corner frequencies and source radii, and their dependence on the relative magnitudes (Figure 4.7). The events with corner frequencies outside the [80,700]Hz frequency band (78/1018, 7.7%) are removed in the magnitude dependence analysis, because these corner frequencies are likely biased due to bandwidth limitations *(Abercrombie, 2021; Shearer et al., 2019)*. Based on synthetic experiments in *Chen & Abercrombie (2020)*, the maximum resolvable corner frequencies should be below 80% of the maximum usable frequency, which is 560 Hz in this case, therefore, the majority of the corner frequencies here are considered resolvable. The median of corner frequencies and radii after removal are 318.56Hz and 1.28m, respectively.

We obtain the median source parameters within each moving window of 0.2 relative magnitude from M_r0.5 to M_r1.9, and only use windows with at least 30 events. Then we analyze the relationship between median source parameters and relative magnitude. Figure 4.7 shows that there is a tendency for corner frequencies to gradually decrease with relative magnitude, however, the slope (-0.008 between corner frequency and relative moment in log scale) is significantly shallower than the expected decrease trend for self-similar scaling observed for natural earthquakes (should be -1/3) *(*e.g., *Abercrombie, 1995; Prieto et al., 2004; Uchide et al., 2014)*. Similarly, for source radius, the radius is nearly independent of magnitude, and only slightly increases with magnitude (scaling factor of 0.047 between radius and relative moment in log scale), which significantly deviates from the trend observed for natural earthquakes (e.g., *Abercrombie, 1995; Mooney, 1989*).

4.6 Discussion

4.6.1 Are microseismic events self-similar?

For self-similar earthquakes, stress drops are independent of magnitude, and corner frequencies should be reciprocally proportional to the cubic root of the seismic moment (Figure 4.7, green dashed lines) *(Eshelby, 1957)*. For natural earthquakes and relatively larger induced earthquakes, there is overwhelming evidence of self-similarity (e.g., *Allmann & Shearer, 2007, 2009, 2011; Huang et al., 2017; Imanishi & Ellsworth, 2006; Uchide et al., 2014; Wu et al., 2018*). The significant deviation between our observed scaling and the predicted self-similar scaling of corner frequency/source radius suggests that these microseismic events are not self-similar.

The stress drop dependence with magnitude can be quantified with a scaling factor *(Chen & Abercrombie, 2020; Trugman & Shearer, 2017)*. For self-similar earthquakes, the scale factor is 0. In this case, we quantify the scale factor between log10 of relative stress change (note that we do not have absolute seismic moments) and relative magnitude. Because the scaling only concerns the relative relationship between stress drop and seismic moment, the lack of absolute magnitude does not affect the relative slope in log domain. The scale factor we obtain is 1.29 (between log10 relative stress change and relative magnitude), significantly larger than most previous studies.

Bandwidth limitations could lead to biased scaling results *(Abercrombie, 2014; Shearer et al., 2019)*, however, this should not be a significant factor for the microseismic events here, given that the majority of corner frequencies are within a resolvable range based on the available bandwidth *(Chen & Abercrombie, 2020)*. *Chen & Abercrombie (2020)* found that wave type and signal-to-noise ratio could lead to different scaling. Assumptions in data processing can also lead to artificial scaling due to tradeoff between parameters *(Shearer et al., 2019)*. However, the observed scale factors due to biases or tradeoffs in data processing are generally weak (scale factors generally lower than 0.5) (e.g., *Zhang et al., 2019*), much lower than the observed scaling factor here.

The non-self-similarity of microseismic events is also reported by multiple studies. *Viegas et al. (2015)* found for events between Mw-1.8 and Mw-0.8, both static and dynamic stress drops increase with seismic moment. *Chen et al., (2021)* reported a large scaling factor of 0.47 for 59 microseismic events. From the aspect of source radius, the non-self-similarity was confirmed by *Chen et al. (2021)* with a factor of 0.18 and *Eaton et al. (2014)* with a factor of 0.47, while *Urbancic and Young (1993)* reported relatively weak scaling for some microseismic events.

Using the tensile-failure source model in *Walter & Brune (1993), Eaton et al. (2014)* suggested that tensile failure events may be associated with S/P wave amplitudes lower than 5. The observed S/P amplitude ratio in Figure S4.9 suggests that most of the detected microseismic events are tensile-failure or mixed tensile-shear failure events. *Eaton et al. (2014)* derived scaling relationship of source radius with magnitude for tensile-failure events. Although our observed scaling relationship differs from the prediction in *Eaton et al. (2014)*, and the S/P ratio indicates a mixture of tensile/shear events, our results further confirm that the microseismic events have different source processes from the shear-failure-dominant natural and induced earthquakes, and have different scaling relationships with magnitude.

4.6.2 Earthquake migration and diffusion

Hydraulic fracturing related microseismicity often exhibits spatial migrations due to fluid diffusion *(Birdsell et al., 2015; Shapiro & Dinske, 2009)*. Based on the final locations, we examine the spatiotemporal evolution pattern of the microseismicity. We focus on stages S3 and S4, because stages S1 and S2 are located outside the array coverage and likely have lower location resolution. Because we have relatively lower depth resolution of the microseismic events, we focus on 2D migration in the horizontal plane. We calculate the 2D distance between each microseismic event and the average location of the first 10% of events in each stage. Then we examine a range of diffusivities to fit a diffusion curve to the microseismicity time-distance evolution:

$$R = \sqrt{4\pi D t} \tag{4.4}$$

where R is horizontal distance, D is liquid diffusivity and t is the time from the first events.

Figure 4.8 (A1, A2) shows that for Stage S3 and S4, D=0.8m^2/s and D=0.6m^2/s match the microseismic event spatial migration pattern well. As a comparison, these diffusivity values are close to that estimated for the tight sand at Barnett Shale of 0.71m^2/s *(Shapiro et al., 2005)*, while another study indicates much larger diffusivity of about 1.6m^2/s at Cotton Valley *(Shapiro & Dinske, 2009)*. The relative stress change dependence on distance is also displayed along with the distance-time distribution (Figure 4.8, B1, B2). In Stages S3 and S4, $\Delta\sigma_r$ steadily increases with microseismic events migrating farther, similar to the distance dependence of relative magnitude and source radius. Increase of $\Delta\sigma_r$ in Stage S2 can also be found during migration, but its migration rate may be more biased because of the azimuthal problem in locations. Also note that the distance-increasing relative stress change is combined with distance-increasing relative moment and distance-increasing source radius (decreasing corner frequency), and these dependence relationships could reflect potentially different source process of microseismic events from tectonic earthquakes. Similar spatial pattern of $\Delta\sigma_r$ has been found for induced earthquakes from injection activities (e.g., *Allmann et al., 2011*); the low $\Delta\sigma_r$ near injection spot compared to those farther could be linked with pore pressure decreasing with distance *(Zoback, 2010)*. These observations suggest that the presence of fluid may influence stress distributions in the subsurface, which is reflected on the spectral content of the seismic sources, and the measured stress changes.

It should be noted that fluid injection may cause different spatial patterns of event types, for example, tensile failure related microseismic events are associated with self-popping or wedging open of natural fractures, and tend to occur closer to the injection points, while microseismic events at distance are often with shear dominated mechanism *(van der Baan et al., 2013; Maxwell, 2011)*. The spatial pattern of source parameters could reflect changes in event type.

4.6.3 Limitation of this study

In this study, we applied a detailed workflow to a microseismic dataset recorded during hydraulic fracturing. The analyses showed spatiotemporal migration patterns that are similar to other observed induced seismicity, indicating possible influence of pore pressure on event occurrence and stress changes. We also find differing magnitude scaling relationships between these microseismic events and other larger natural or induced earthquakes. The observed scaling relationship suggests that the source radius is nearly constant with magnitude, and stress change increases with magnitude.

While we have carefully considered the possible influences of azimuthal coverage and frequency bandwidth on the interpretation, the potential temporal changes in the underground medium due to fracturing are not considered. Ideally, we should invert for velocity models during each stage only using corresponding perforation shots, however, this is difficult given the lower signal-to-noise ratio of the perforation shots. Similarly, attenuation could be different at different stages, which may cause uncertainties in event terms from the joint spectral decomposition of all stages. As shown in Figure S4.6, we notice differences in corner frequencies between processing all stages and only using stage S4, however, the median values are approximately consistent, suggesting no systematic biases.

Moreover, since our study focused on S-waves due to higher signal-to-noise ratio than P-wave, the auxiliary parameters proposed by *Walter & Brune (1993)*, such as the seismic efficiency, the ratio of P/S corner frequencies, are not analyzed in this study. Our stacking analysis smooths the event source spectra by averaging from multiple stations, so the oscillation due to opening/closing is not clearly observed (e.g., those reported in *Eaton et al., 2014*). Therefore, our analysis could not fully distinguish the influence of event type on source processes in the hydraulic fracking experiment.

4.7 Conclusions

We build a calibrated 1D velocity model using well log and perforation shots, and detect/locate microseismic events from raw downhole geophone array during hydraulic fracturing. We perform a detailed analysis of the spatiotemporal evolution of microseismic source parameters as well as their magnitude dependence. The results show that these microseismic events exhibit clear diffusive migration patterns in space and time, and source parameters show gradual changes with distance from injection source, suggesting an influence of fluid on event occurrence and source processes. The microseismic events are found to be non-self-similar, with nearly constant source radius/corner frequency with magnitude, and relative stress changes increase with magnitude. Such behaviors differ from natural/induced earthquakes that are dominated by shear failure along faults, but are consistent with other microseismic studies that may feature more tensile-failure events, suggesting possibly different rupture processes.

4.8 Acknowledgement

We thank Chesapeake Energy Corporation for providing the microseismic data for this research. Part of the analysis performed in this study is facilitated by OU Supercomputing Center for Education & Research (OSCER) at the University of Oklahoma (OU). The research is supported by McCoy grant from MCEE (Mewbourne College of Earth and Energy) at OU.

References

Abercrombie, R. E. (1995). Earthquake source scaling relationships from −1 to 5 ML using seismograms recorded at 2.5-km depth. *Journal of Geophysical Research*, *100*(B12), 24015–24036.

Abercrombie, Rachel E. (2014). Stress drops of repeating earthquakes on the San Andreas Fault at Parkfield. *Geophysical Research Letters*, *41*(24), 8784–8791. https://doi.org/10.1002/2014GL062079

Abercrombie, Rachel E. (2021). Resolution and uncertainties in estimates of earthquake stress drop and energy release. *Philosophical Transactions of the Royal Society A: Mathematical, Physical and Engineering Sciences* (Vol. 379). https://doi.org/10.1098/rsta.2020.0131

Aki, K. (1967). Scaling law of seismic spectrum. *Journal of Geophysical Research*, *72*(4), 1217–1231. https://doi.org/10.1029/JZ072i004p01217

Aki, K., & Richards, P. G. (1980). Quantative seismology: Theory and methods. *Quantative Seismology: Theory and Methods. by K. Aki and PG Richards. San Francisco: Freeman.*

Allen, R. (1982). Automatic phase pickers: Their present use and future prospects. *Bulletin of the Seismological Society of America*, *72*(6B), S225–S242. https://doi.org/10.1785/BSSA07206B0225

Allen, R. V. (1978). Automatic earthquake recognition and timing from single traces. *Bulletin of the Seismological Society of America*, *68*(5), 1521–1532.

Allmann, B. P., & Shearer, P. M. (2007). Spatial and temporal stress drop variations in small earthquakes near Parkfield, California. *Journal of Geophysical Research: Solid Earth*, *112*(4), 1–17. https://doi.org/10.1029/2006JB004395

Allmann, B. P., & Shearer, P. M. (2009). Global variations of stress drop for moderate to large earthquakes. *Journal of Geophysical Research: Solid Earth*, *114*(1), 1–22. https://doi.org/10.1029/2008JB005821

Awang, H., Ahmad Rashidi, N. R., Yusof, M., & Mohammad, K. (2017). Correlation between P-wave Velocity and Strength Index for Shale to Predict Uniaxial Compressive Strength Value. *MATEC Web of Conferences*, *103*, 1–8. https://doi.org/10.1051/matecconf/201710307017

van der Baan, M., Eaton, D., & Dusseault, M. (2013). Microseismic monitoring developments in hydraulic fracture stimulation. *ISRM International Conference for Effective and Sustainable Hydraulic Fracturing 2013*, 439–466. https://doi.org/10.5772/56444

Baig, A., & Urbancic, T. (2010). Microseismic moment tensors: A path to understanding frac growth. *The Leading Edge*, *29*(3), 320–324. https://doi.org/10.1190/1.3353729

Bardainne, T., & Gaucher, E. (2010). Constrained tomography of realistic velocity models in microseismic monitoring using calibration shots. *Geophysical Prospecting*, *58*(5), 739–753. https://doi.org/10.1111/j.1365-2478.2010.00912.x

Birdsell, D. T., Rajaram, H., Dempsey, D., & Viswanathan, H. S. (2015). Hydraulic fracturing fluid migration in the subsurface: A review and expanded modeling results. *Water Resources Research*, *51*(9), 7159–7188. https://doi.org/10.1002/2015WR017810

Brune, J. N. (1970). Tectonic stress and the spectra of seismic shear waves from earthquakes. *Journal of Geophysical Research*, *75*(26), 4997–5009. https://doi.org/10.1029/JB075i026p04997

Chen, D., Li, N., & Wang, E. yuan. (2021). Reliability Assessment of the Hydraulic Fracturing Process in Coal Mine Based on the Analysis of Micro-Seismic Source Parameters. *Natural Resources Research*, *30*(3), 2317–2332. https://doi.org/10.1007/s11053-021-09840-6

Chen, X., & Abercrombie, R. E. (2020). Improved approach for stress drop estimation and its application to an induced earthquake sequence in Oklahoma. *Geophysical Journal International*, *223*(1), 233–253. https://doi.org/10.1093/gji/ggaa316

Eaton, D. W., van der Baan, M., Birkelo, B., & Tary, J. B. (2014). Scaling relations and spectral characteristics of tensile microseisms: Evidence for opening/closing cracks during hydraulic fracturing. *Geophysical Journal International*, *196*(3), 1844–1857. https://doi.org/10.1093/gji/ggt498

Eshelby JD. (1957). The determination of the elastic field of an ellipsoidal inclusion, and related problems. *Proceedings of the Royal Society of London. Series A. Mathematical and Physical Sciences*, *241*(1226), 376–396. https://doi.org/10.1098/rspa.1957.0133

Fischer, T., Hainzl, S., Eisner, L., Shapiro, S. A., & Le Calvez, J. (2008). Microseismic signatures of hydraulic fracture growth in sediment formations: Observations and modeling. *Journal of Geophysical Research: Solid Earth*, *113*(2), 1–12. https://doi.org/10.1029/2007JB005070

Goertz-Allmann, B. P., Goertz, A., & Wiemer, S. (2011). Stress drop variations of induced earthquakes at the Basel geothermal site. *Geophysical Research Letters*, *38*(9), n/a-n/a. https://doi.org/10.1029/2011gl047498

Guo, H., & Zhang, H. (2017). Development of double-pair double difference earthquake location algorithm for improving earthquake locations. *Geophysical Journal International*, *208*(1), 333–348. https://doi.org/10.1093/gji/ggw397

Huang, Y., Ellsworth, W. L., & Beroza, G. C. (2017). Stress drops of induced and tectonic earthquakes in the central United States are indistinguishable. *Science Advances*, *3*(8), 1–8. https://doi.org/10.1126/sciadv.1700772

Imanishi, K., & Ellsworth, W. L. (2006). Source scaling relationships of microearthquakes at Parkfield, CA, determined using the SAFOD Pilot Hole Seismic Array (pp. 81–90). https://doi.org/10.1029/170GM10

Madariaga, R. (1976). Dynamics of an expanding circular fault. *Bulletin of the Seismological Society of America*, *66*(3), 639–666. Retrieved from http://bssa.geoscienceworld.org/content/66/3/639.abstract

Maxwell, S. (2011). Microseismic hydraulic fracture imaging: The path toward optimizing shale gas production. *The Leading Edge*, *30*(3), 340–346. https://doi.org/10.1190/1.3567266

Maxwell, S. C., Rutledge, J., Jones, R., & Fehler, M. (2010). Petroleum reservoir characterization using downhole microseismic monitoring. *Geophysics*, *75*(5).

https://doi.org/10.1190/1.3477966

Mooney, W. D. (1989). Chapter 2: Seismic methods for determining earthquake source parameters and lithospheric structure (pp. 11–34). https://doi.org/10.1130/MEM172-p11

Pei, D., Quirein, J. A., Cornish, B. E., Quinn, D., & Warpinski, N. R. (2009). Velocity calibration for microseismic monitoring: A very fast simulated annealing (VFSA) approach for joint-objective optimization. *Geophysics*, *74*(6). https://doi.org/10.1190/1.3238365

Prieto, G. A., Shearer, P. M., Vernon, F. L., & Kilb, D. (2004). Earthquake source scaling and self-similarity estimation from stacking P and S spectra. *Journal of Geophysical Research B: Solid Earth*, *109*(8). https://doi.org/10.1029/2004JB003084

Qin, X. (2013). Vp-Vs Relations of Organic-rich Shales. *Thesis*.

Ross, Z. E., & Ben-Zion, Y. (2014). Automatic picking of direct P, S seismic phases and fault zone head waves. *Geophysical Journal International*, *199*(1), 368–381. https://doi.org/10.1093/gji/ggu267

Ruhl, C. J., Abercrombie, R. E., & Smith, K. D. (2017). Spatiotemporal Variation of Stress Drop During the 2008 Mogul, Nevada, Earthquake Swarm. *Journal of Geophysical Research: Solid Earth*, *122*(10), 8163–8180. https://doi.org/10.1002/2017JB014601

Sasaki, S. (1998). Characteristics of microseismic events induced during hydraulic fracturing experiments at the Hijiori hot dry rock geothermal energy site, Yamagata, Japan. *Tectonophysics*, *289*(1–3), 171–188. https://doi.org/10.1016/S0040-1951(97)00314-4

Shapiro, S.A., & Dinske, C. (2009). Fluid-induced seismicity: Pressure diffusion and hydraulic fracturing. *Geophysical Prospecting*, *57*(2), 301–310. https://doi.org/10.1111/j.1365-2478.2008.00770.x

Shapiro, Serge A., Rentsch, S., & Rothert, E. (2005). Characterization of hydraulic properties of rocks using probability of fluid-induced microearthquakes. *Geophysics*, *70*(2), 27–33. https://doi.org/10.1190/1.1897030

Shearer, P. M., Prieto, G. A., & Hauksson, E. (2006). Comprehensive analysis of earthquake source spectra in southern California. *Journal of Geophysical Research: Solid Earth*. https://doi.org/10.1029/2005JB003979

Shearer, P. M., Abercrombie, R. E., Trugman, D. T., & Wang, W. (2019). Comparing EGF Methods for Estimating Corner Frequency and Stress Drop From P Wave Spectra. *Journal of Geophysical Research: Solid Earth*, *124*(4). https://doi.org/10.1029/2018JB016957

Sondergeld, C. H., Rai, C. S., Margesson, R. W., & Whidden, K. J. (2000). Ultrasonic measurement of anisotropy on the Kimmeridge Shale. In *SEG Technical Program Expanded Abstracts 2000* (pp. 1858–1861). Society of Exploration Geophysicists. https://doi.org/10.1190/1.1815791

Song, F., & Toksöz, M. N. (2011). Full-waveform based complete moment tensor inversion and source parameter estimation from downhole microseismic data for hydrofracture monitoring. *Geophysics*, *76*(6). https://doi.org/10.1190/geo2011-

0027.1

Song, F., Kuleli, H. S., Toksöz, M. N., Ay, E., & Zhang, H. (2010). An improved method for hydrofracture-induced microseismic event detection and phase picking. *Geophysics*, *75*(6), 2–7. https://doi.org/10.1190/1.3484716

Thurber, C. H. (1985). Nonlinear earthquake location: Theory and examples. *Bulletin of the Seismological Society of America*, *75*(3), 779–790. https://doi.org/10.1785/BSSA0750030779

Trnkoczky A. (2002). Understanding and parameter setting of STA/LTA trigger algorithm. *New Manual of Seismological Observatory Practice* (NMSOP) (pp. 1-20). Deutsches GeoForschungsZentrum GFZ.

Trugman, D. T., & Shearer, P. M. (2017). Application of an improved spectral decomposition method to examine earthquake source scaling in Southern California. *Journal of Geophysical Research: Solid Earth*, *122*(4), 2890–2910. https://doi.org/10.1002/2017JB013971

Uchide, T., Shearer, P. M., & Imanishi, K. (2014). Stress drop variations among small earthquakes before the 2011 Tohoku-oki, Japan, earthquake and implications for the main shock. *Journal of Geophysical Research: Solid Earth*, *119*(9), 7164–7174. https://doi.org/10.1002/2014JB010943

Urbancic, T. I., & Young, R. P. (1993). Space-time variations in source parameters of mining-induced seismic events with M < 0. *Bulletin - Seismological Society of America*, *83*(2), 378–397.

Vaezi, Y., & van der Baan, M. (2015). Comparison of the STA/LTA and power spectral density methods for microseismic event detection. *Geophysical Journal International*, *203*(3), 1896–1908. https://doi.org/10.1093/gji/ggv419

Vavryčuk, V. (2001). Inversion for parameters of tensile earthquakes. *Journal of Geophysical Research: Solid Earth*, *106*(B8), 16339–16355. https://doi.org/10.1029/2001JB000372

Viegas, G., Urbancic, T., Baig, A., & Von Lunen, E. (2015). Rupture dynamics and source scaling relations of microseismic hydraulic fractures in shale reservoirs. *13th ISRM International Congress of Rock Mechanics*, *2015-MAY*(May), 1–10.

Waldhauser, F., & Ellsworth, W. L. (2000). A Double-difference Earthquake location algorithm: Method and application to the Northern Hayward Fault, California. *Bulletin of the Seismological Society of America*, *90*(6), 1353–1368. https://doi.org/10.1785/0120000006

Walter, W. R., & Brune, J. N. (1993). Spectra of seismic radiation from a tensile crack. *Journal of Geophysical Research: Solid Earth*, *98*(B3), 4449–4459. https://doi.org/10.1029/92JB02414

Wang, Q., & Li, R. (2017). Research status of shale gas: A review. *Renewable and Sustainable Energy Reviews*, *74*(March), 715–720. https://doi.org/10.1016/j.rser.2017.03.007

Warpinski, N. R., Sullivan, R. B., Uhl, J. E., Waltman, C. K., & Machovoe, S. R. (2003). Improved Microseismic Fracture Mapping Using Perforation Timing Measurements for Velocity Calibration. In *All Days* (Vol. 10, pp. 14–23). SPE. https://doi.org/10.2118/84488-MS

Withers, M., Aster, R., Young, C., Beiriger, J., Harris, M., Moore, S., & Trujillo, J. (1998). A comparison of select trigger algorithms for automated global seismic phase and event detection. *Bulletin of the Seismological Society of America*, *88*(1), 95–106.

Wu, Q., Chapman, M., & Chen, X. (2018). Stress-drop variations of induced earthquakes in Oklahoma. *Bulletin of the Seismological Society of America*, *108*(3), 1107–1123. https://doi.org/10.1785/0120170335

Yu, H., Harrington, R. M., Kao, H., Liu, Y., Abercrombie, R. E., & Wang, B. (2020). Well Proximity Governing Stress Drop Variation and Seismic Attenuation Associated With Hydraulic Fracturing Induced Earthquakes. *Journal of Geophysical Research: Solid Earth*, *125*(9), 1–17. https://doi.org/10.1029/2020JB020103

Zhang, H., & Thurber, C. H. (2003). Double-difference tomography: The method and its application to the Hayward Fault, California. *Bulletin of the Seismological Society of America*, *93*(5), 1875–1889. https://doi.org/10.1785/0120020190

Zhang, J., Chen, X., & Abercrombie, R. E. (2019). Resolving the spatiotemporal variability of small earthquake source parameters at Parkfield and their relationship with 2004M6 Parkfield earthquake. In *AGU Fall Meeting Abstracts* (Vol. 2019, pp. S52C-05).

Zhang, J., Zhang, H., Zhang, Y., & Liu, Q. (2016). Calibrating one-dimensional velocity model for downhole microseismic monitoring using station-pair differential arrival times based on the differential evolution method. *Physics of the Earth and Planetary Interiors*, *261*, 124–132. https://doi.org/10.1016/j.pepi.2016.06.003

Zoback, M. D. (2010). *Reservoir geomechanics*. Cambridge university press.

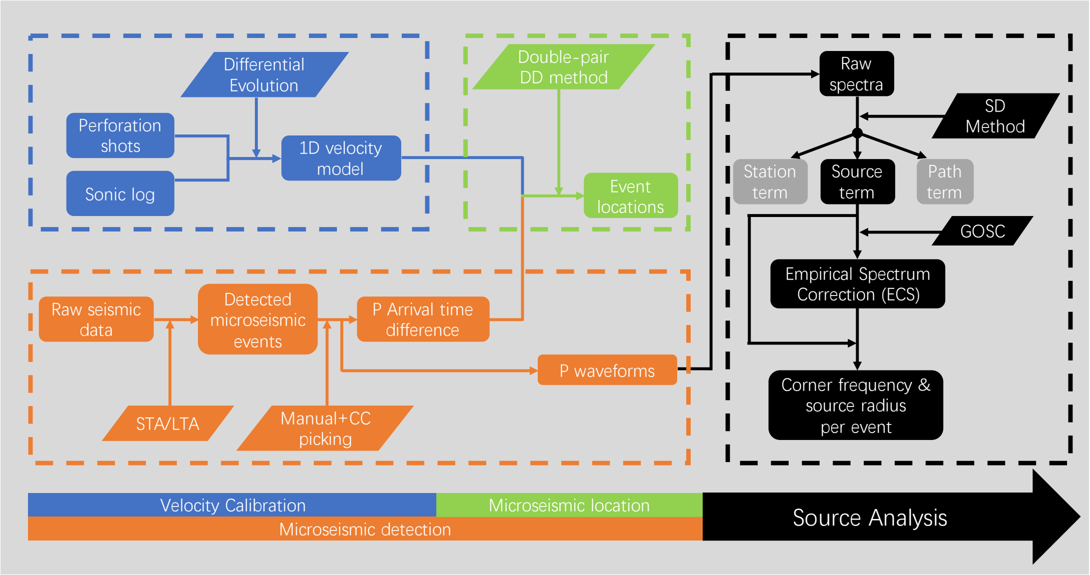

Figure 4.1: Workflow of the analyses. The whole study consists of four parts: Velocity calibration, microseismic detection, microseismic location and source analysis, marked with different colors.

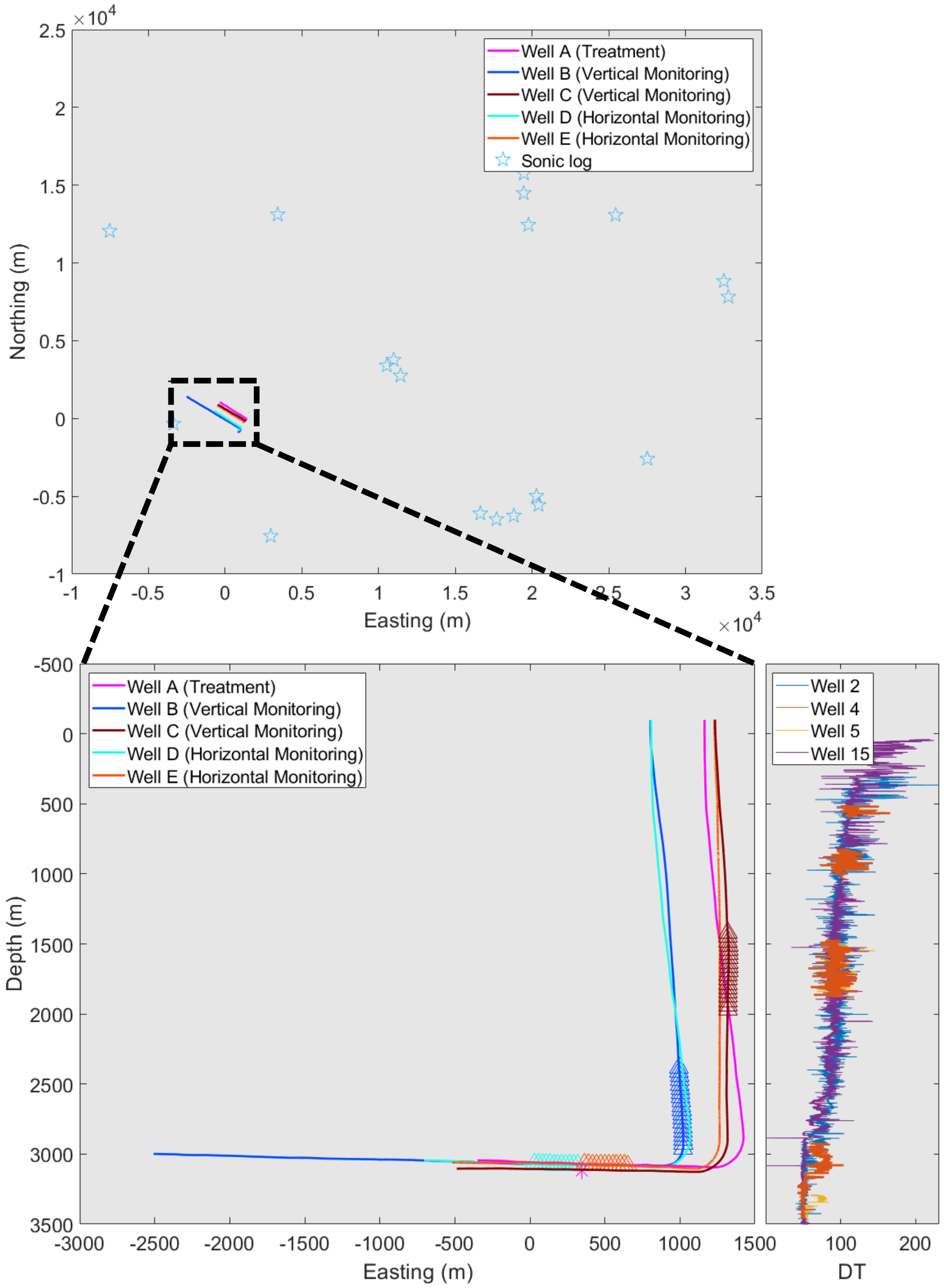

Figure 4.2: Geometry of the study area. Top: Map view of the whole area with well setup, light blue stars showing sonic log wells, and colored curves representing monitoring wells and treatment wells in the study area; Bottom: Left panel shows a zoom-in of study area in Top marked by black dashed rectangle with curves in the same color scheme, and Right panel shows sonic logs from the nearby four logging wells (2/4/5/15), where DT describes traveltime between two ends of the measuring bar down-hole and can be converted to sonic velocity. The origin location are the same for both the top and bottom panels, and will be frequently used later.

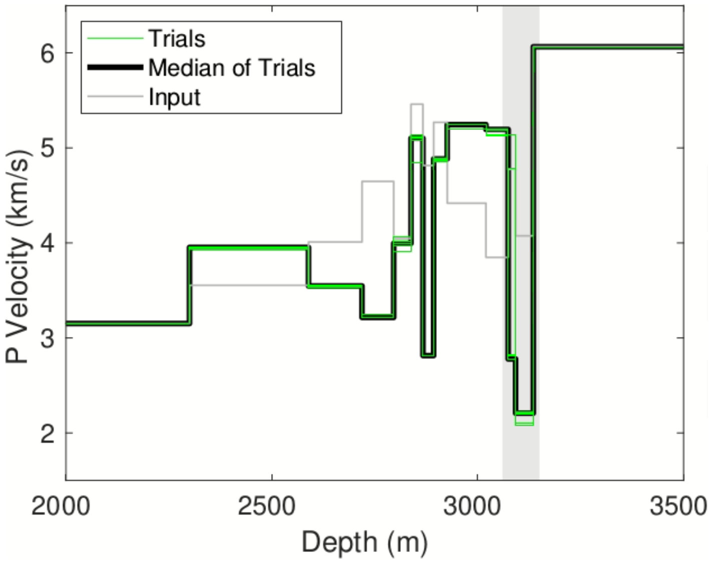

Figure 4.3: Velocity calibration results using all available perforation shots (11) from stage S4 compared to the initial model (thin black line) from sonic log. Green lines denote the 10 different trials of DE inversion, and the thick black line is the median of the green lines used as the finally calibrated 1D velocity model (see text for details).

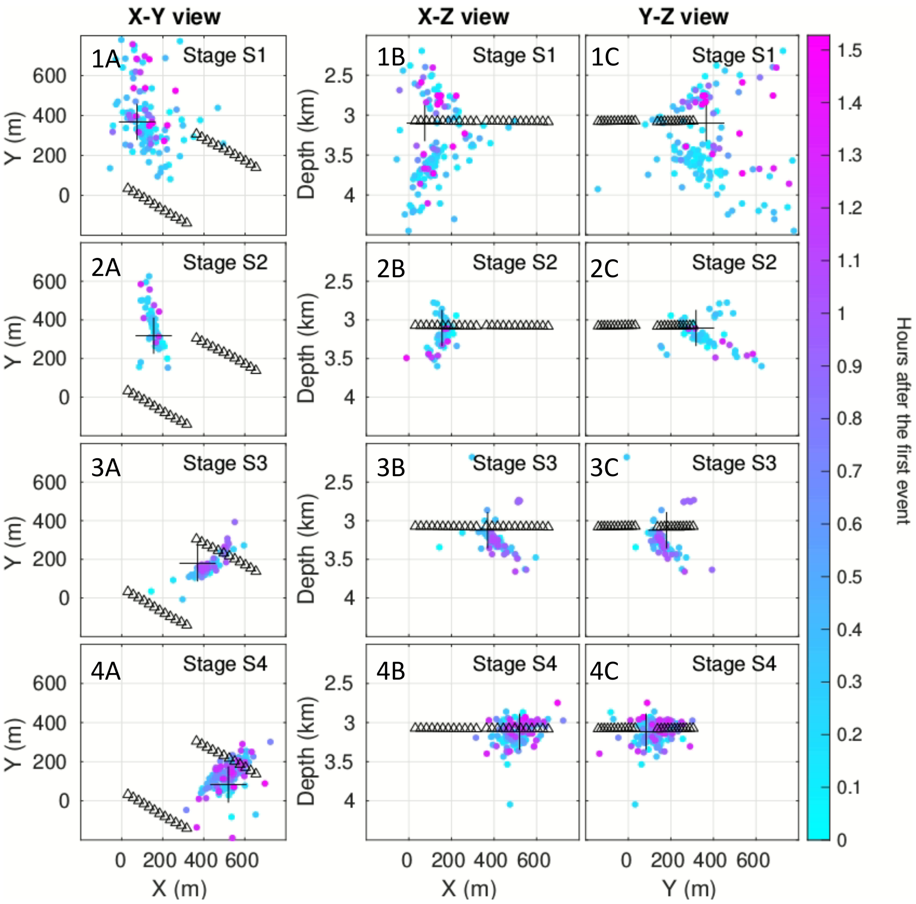

Figure 4.4: Location results of Stage S1 (1A-1C), Stage S2 (2A-2C), Stage S3 (3A-3C) and Stage S4 (4A-4C) using P wave. Dots are color-coded by start times of event waveforms. Plus '+' marks denote the location of perforation shots in the four stages, and they are also used as the initial location of event relocation for the corresponding stages.

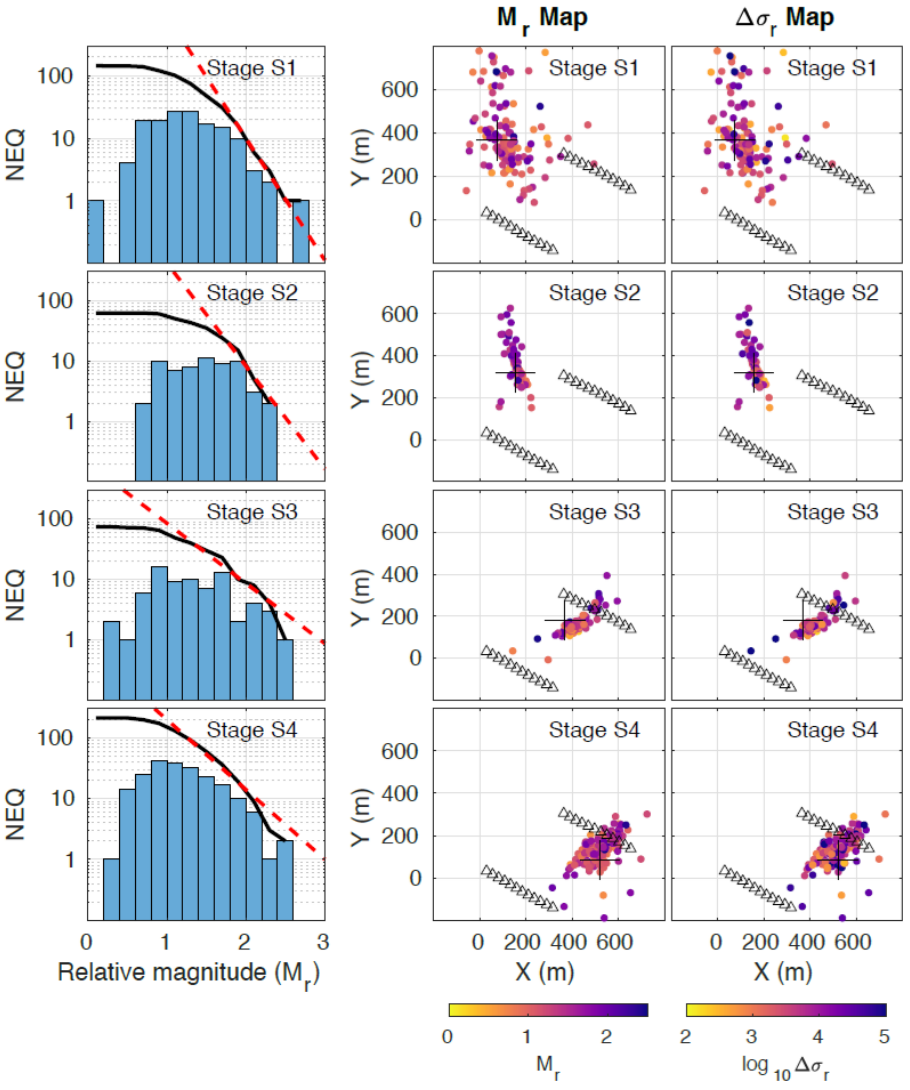

Figure 4.5: Source related information: statistics of magnitude (1A-4A), spatial distribution of relative magnitude (1B-4B) and relative stress change (1C-4C). Dots are color-coded by the corresponding values. In 1A-4A, black curves represent cumulative earthquake frequency number larger than a certain magnitude, and red dashed line represent the best-fit G-R relationship.

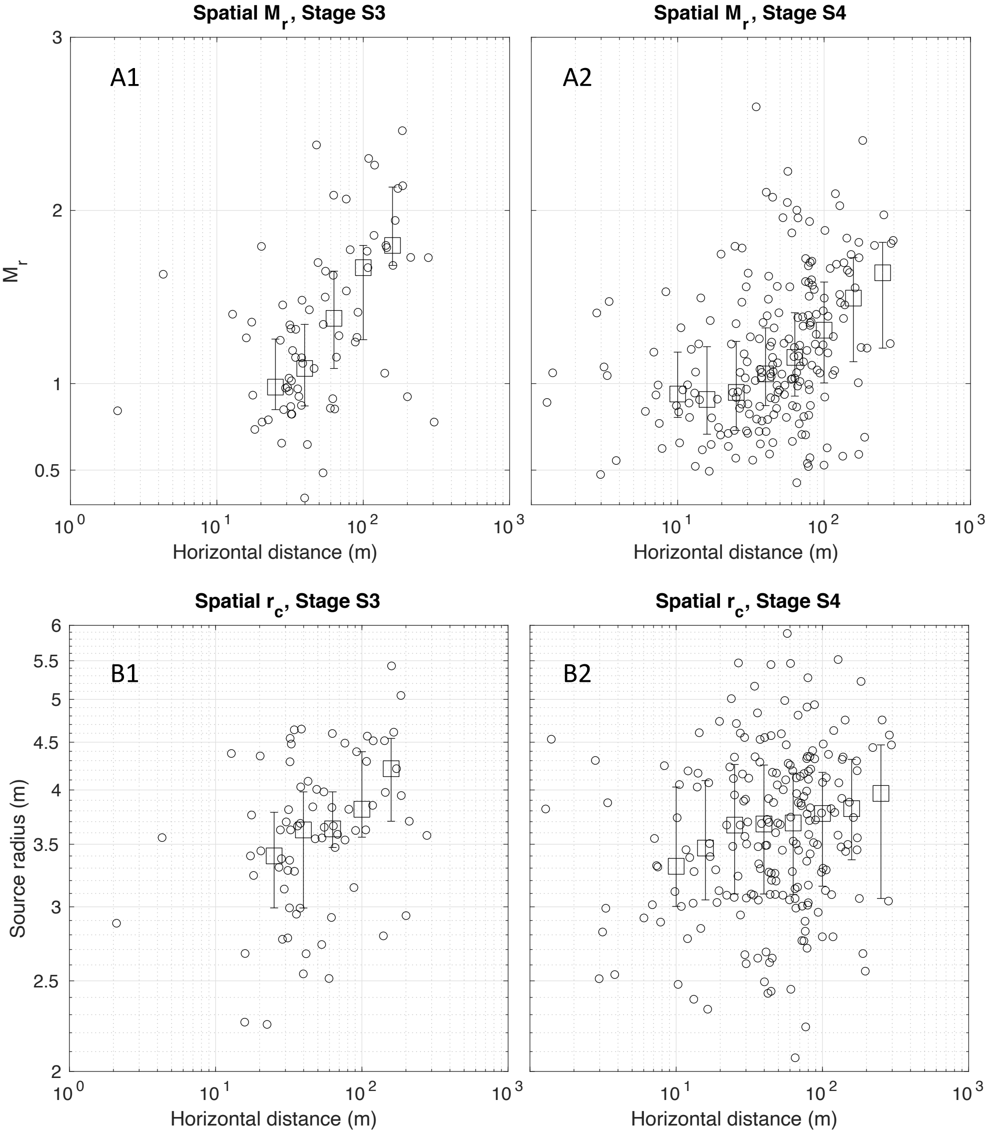

Figure 4.6: Relative magnitude dependence on horizontal distance (A1, A2) and source radius dependence on horizontal distance (B1, B2). Squares represent the median calculated over log horizontal distance windows, and vertical bars represent the 25th and 75th percentile of data in each distance bin.

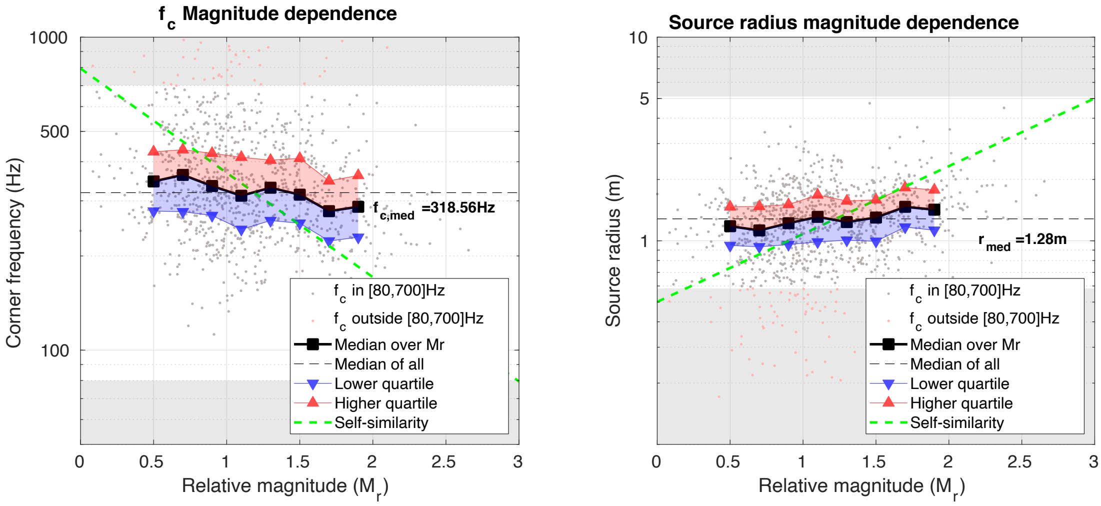

Figure 4.7: Magnitude dependence of corner frequency (left) and source radius (right). Black squares are the median values of corner frequency and source radius for each relative magnitude bin (size=0.2), and red and blue triangles denote the 25th and 75th percentile of data for each relative magnitude bin. Green line indicates expected scaling if events are self-similar (e.g., *Abercrombie, 2020*).

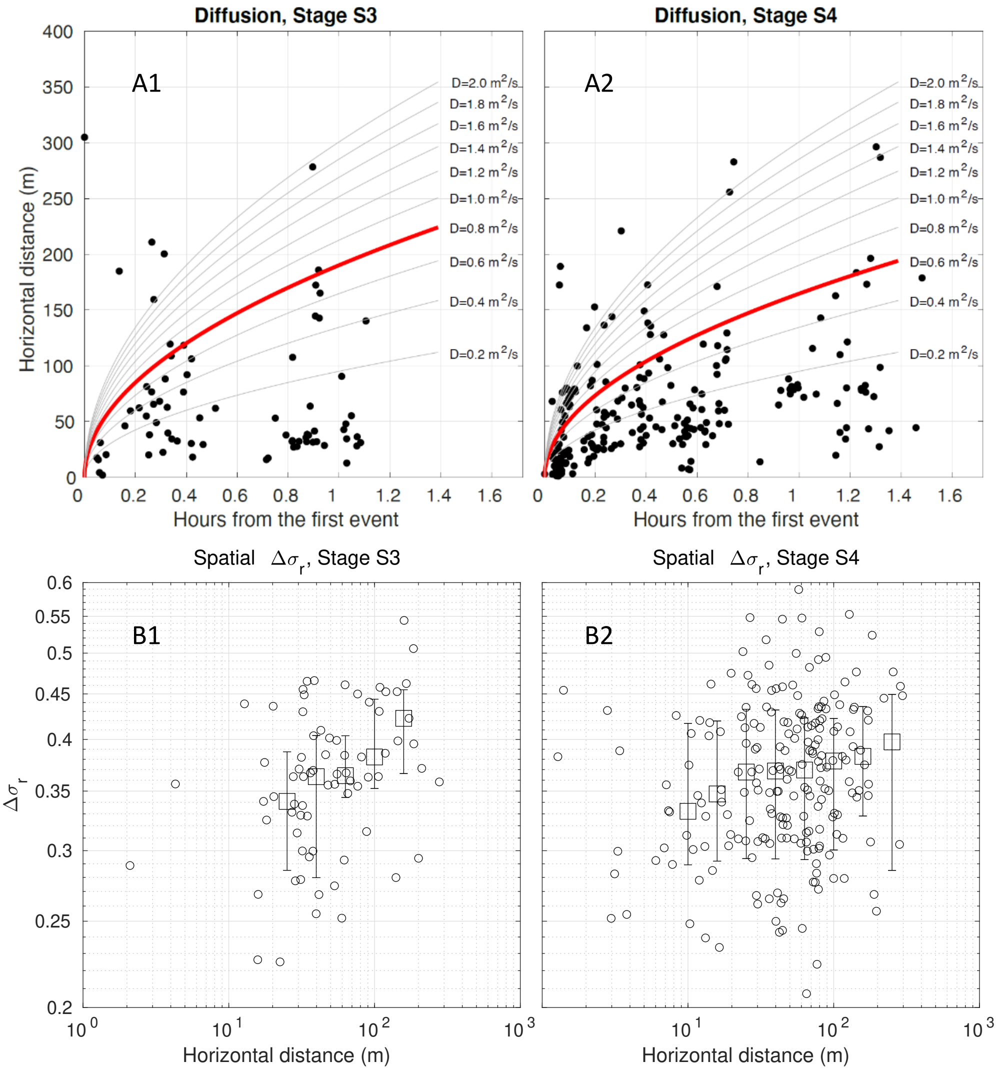

Figure 4.8: (A1, A2) Microseismic event migration over time in Stage S3 and S4. The solid curves denote the assumed diffusion curve with different diffusivity values D, and red thick curves show the best matching D (Stage S3: 0.8m^2/s, Stage S4: 0.6m^2/s). (B1, B2) Relative stress change dependence on horizontal distance (distance bins are the same as Figure 6) for stages S3 and S4. Squares represent the median calculated over log horizontal distance windows, and vertical bars represent the 25th and 75th percentile of data in each distance bin.

Appendix

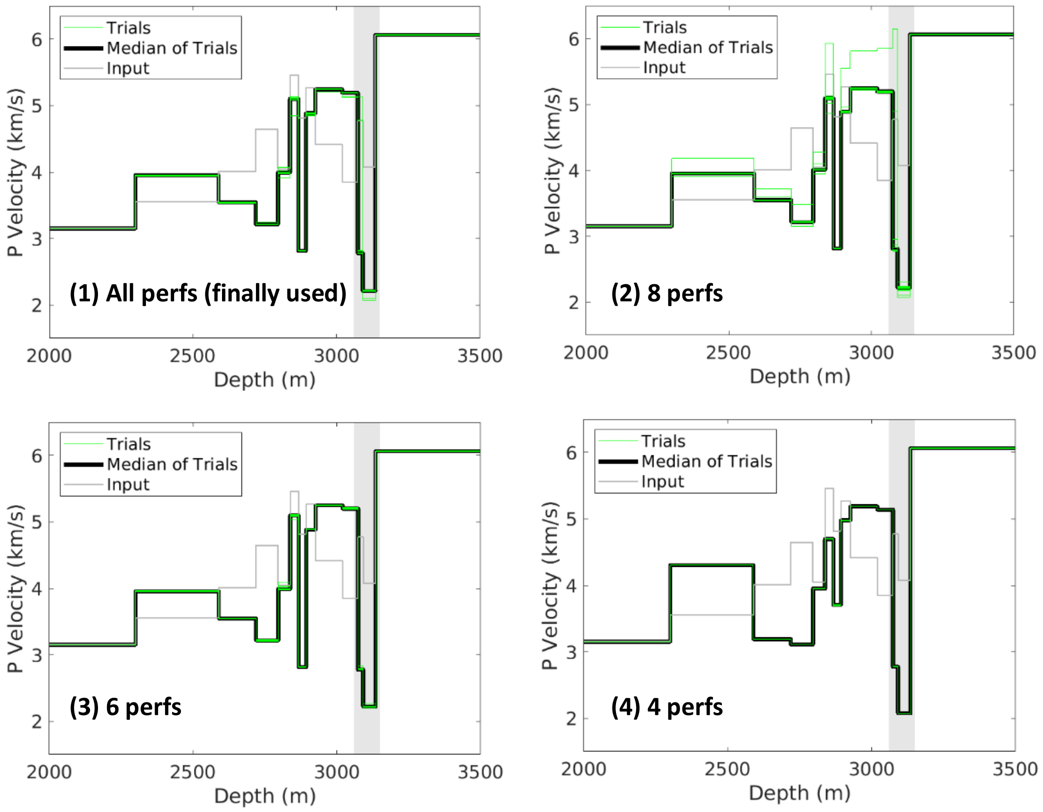

Figure S4.1: Verification of velocity calibration using fewer numbers of perforation shots. (1) All perforation shots are used, same as Figure 3. (2) - (4) show velocity model obtained using 8, 6 and 4 perforation shots, respectively. Potential shale depth is marked in gray.

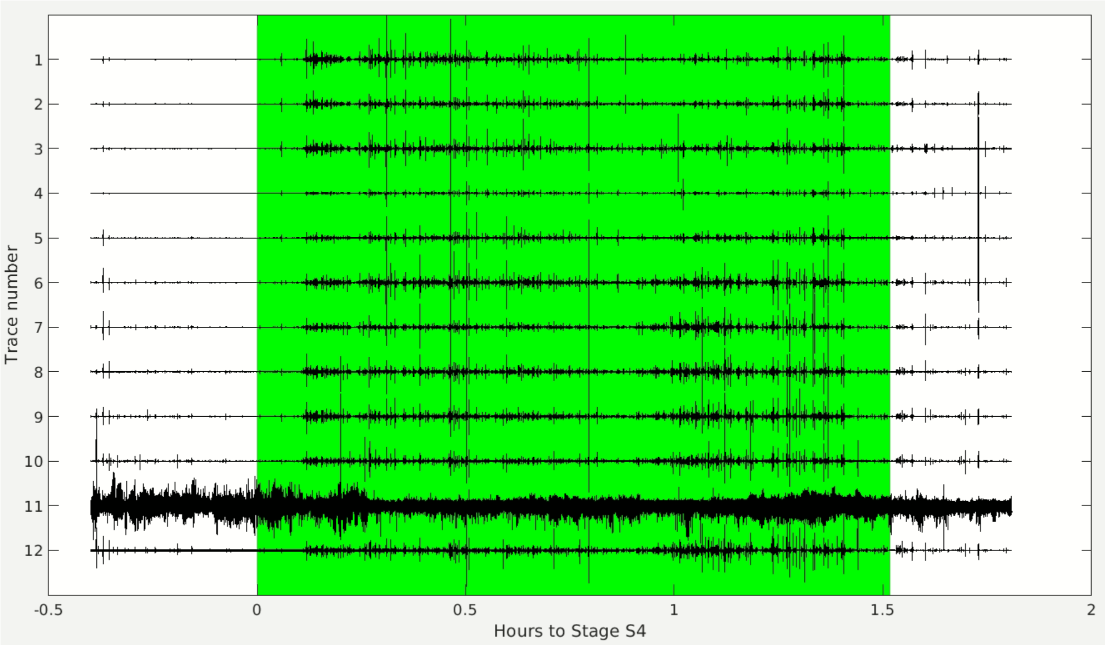

Figure S4.2: Raw waveform recorded by horizontal array in monitoring well E, which contains Stage S4 pumping period (green). X-axis shows the time relative to the beginning of Stage S4.

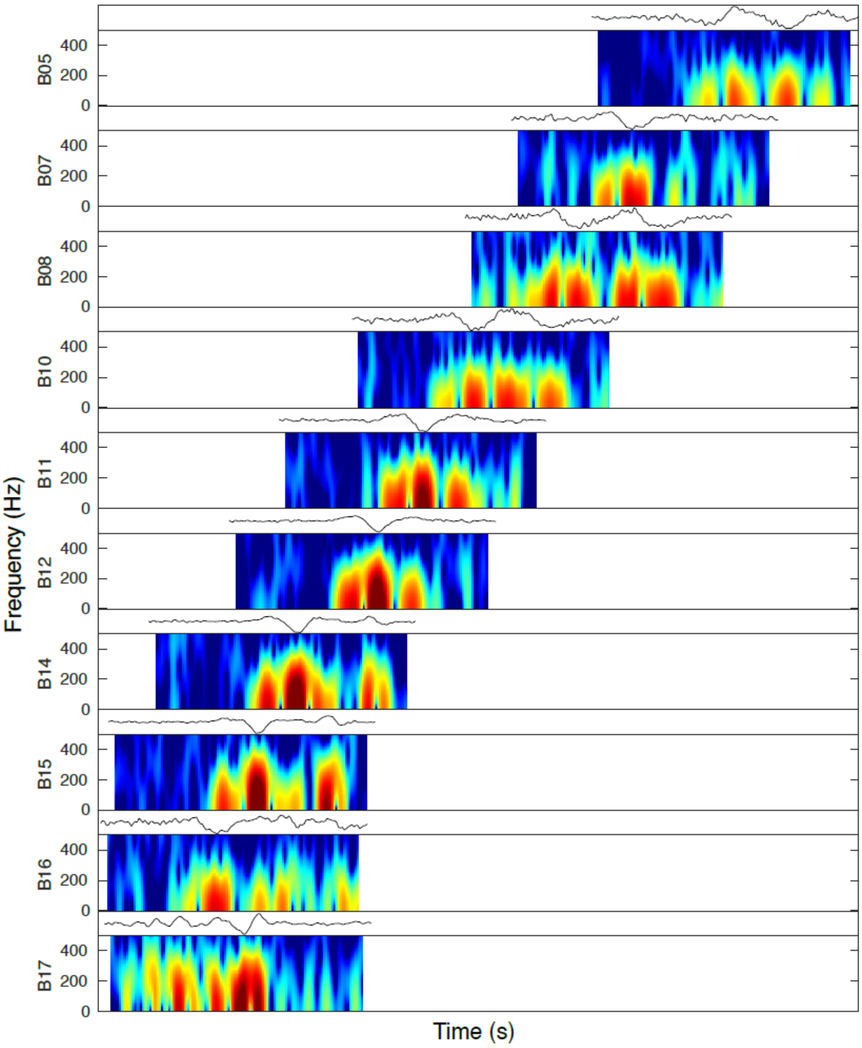

Figure S4.3: Waveform and corresponding spectrogram of an event in Stage S4 detected on 10 stations in monitoring well B. Y-axis represents frequency from 0 to 450 Hz, and X-axis represents time in seconds. The detection in each trace has 0.07s (140 samples) duration, and the spectrogram in each trace is calculated in a moving time window of 0.005s (10 samples) with a step of 0.0005s (1 sample) over X-axis. Colormap has maximum and minimum values of 80dB and 50dB.

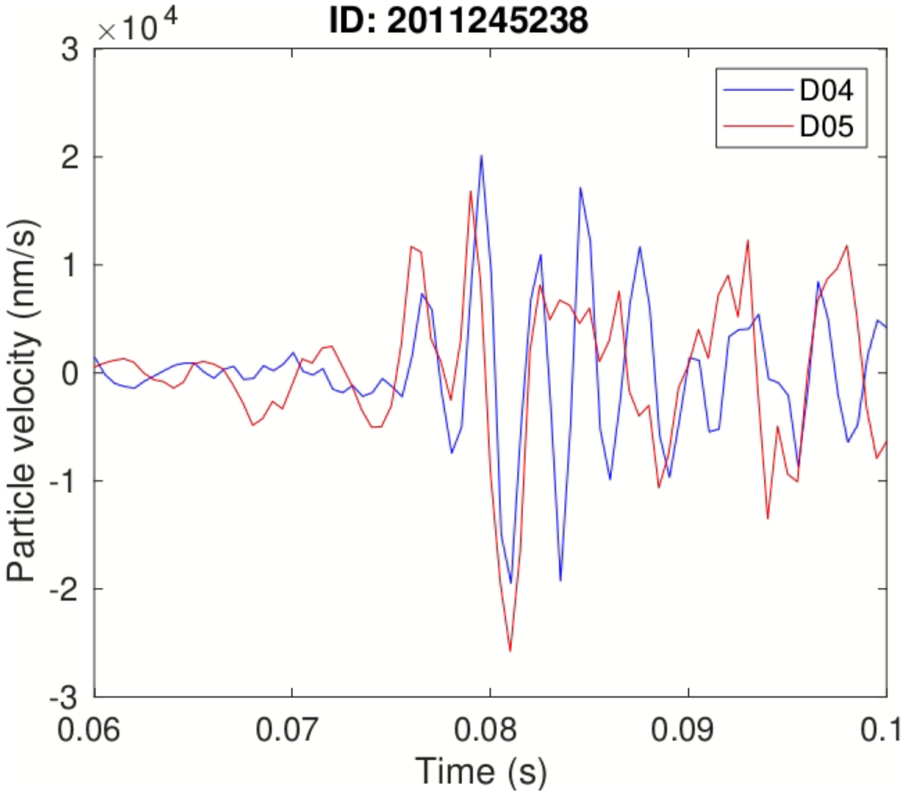

Figure S4.4: An example of waveforms for one event recorded by two stations in the same monitoring well D shifted with cross-correlation time lag.

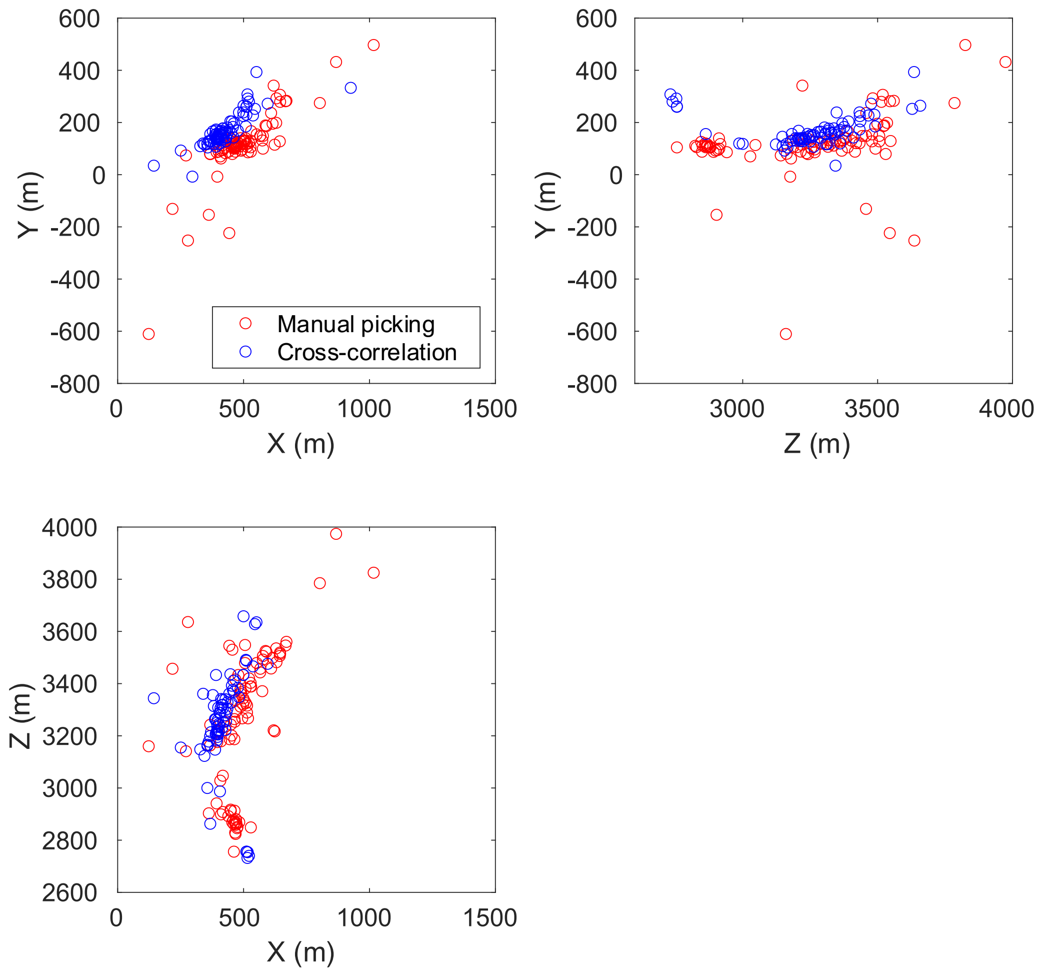

Figure S4.5: location results using manual picking (red) and cross-correlation time lags (blue) for Stage S3.

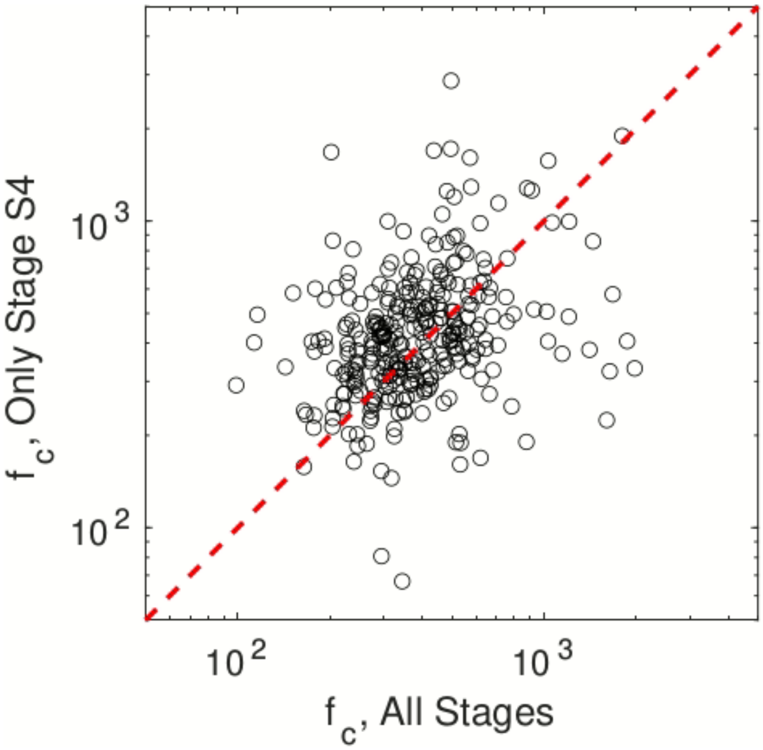

Figure S4.6: Comparison of corner frequency using all stages (X axis) and only Stage S4 (Y axis). Black circles represent individual microseismic events, and the red dashed line shows where the two results are consistent.

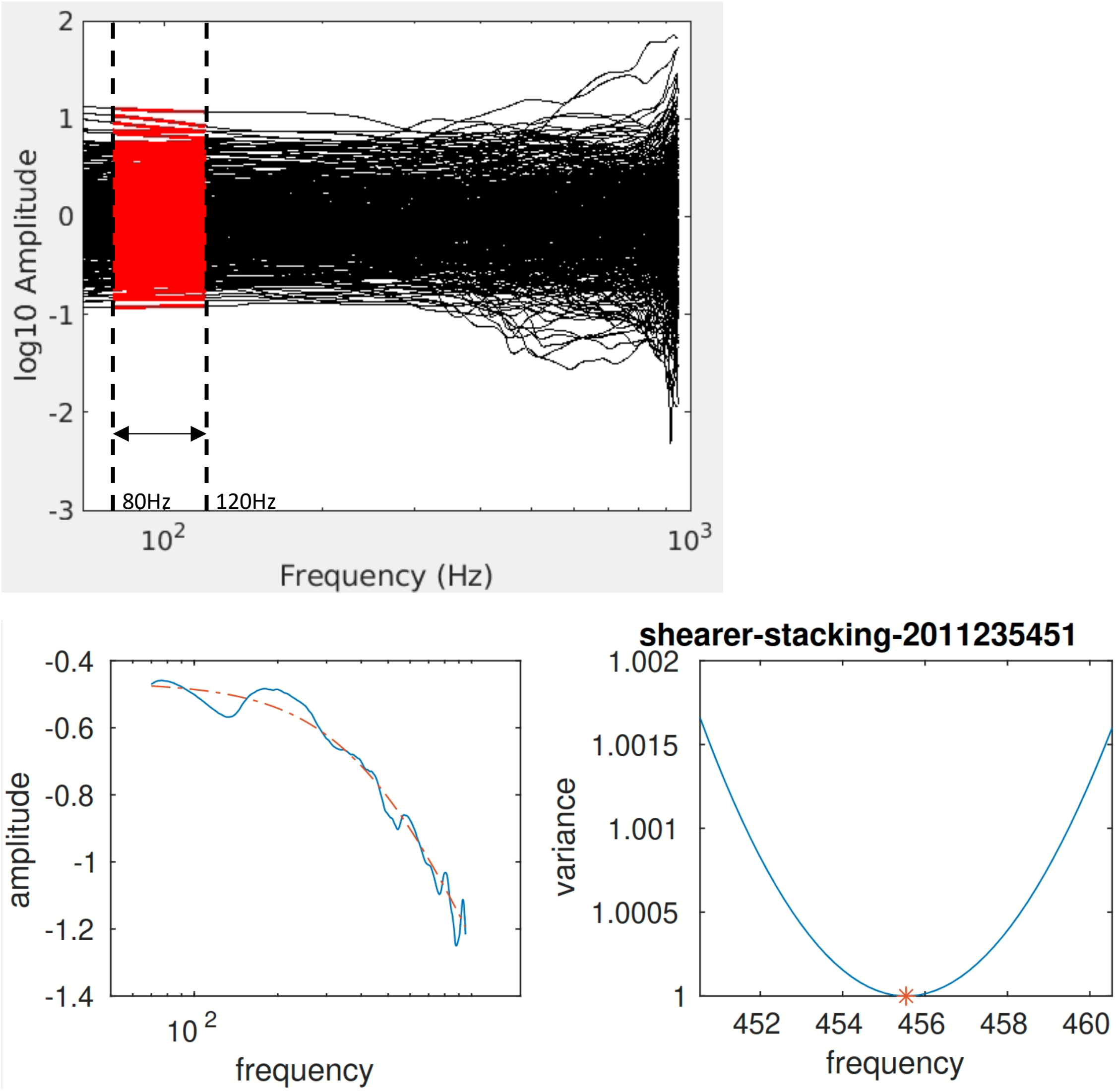

Figure S4.7: Top: event spectra of 449 events with SNR>2 per frequency sample from 2126 raw spectra on different stations after spectral decomposition for Stage S4. Red part of the spectra marks the low frequency plateau (80-120Hz) used to obtain relative moment magnitudes. Bottom left: an example spectrum corrected by ECS. Bottom right: misfit between theoretical model (red) and real spectrum (blue) with different corner frequency input, red asteroid marks the best fit corner frequency of this spectrum.

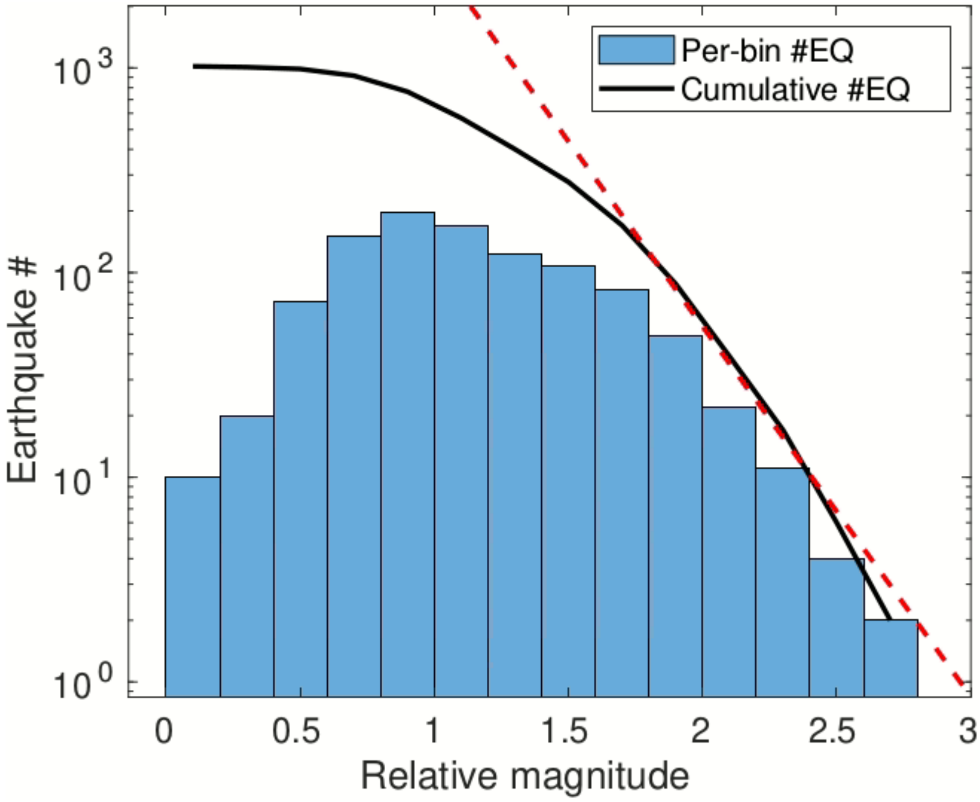

Figure S4.8: Relative moment magnitude histogram of earthquakes from all 4 stages. Black line shows cumulative earthquake frequency number larger than a certain magnitude. M_r=[1.5,2.5] approximates the Gutenberg-Richter Law (red dashed line).

	Total double pairs	Double pairs after iterations	Pairs %	Events located
Stage S1	5140	3540	68.9%	147 of 354
Stage S2	1956	1706	87.2%	66 of 158
Stage S3	7994	6651	83.2%	77 of 146
Stage S4	20326	16515	81.3%	220 of 536

Table 4.1: Table 1: Data used for location in each stage. Some double pairs that have significant differences between observation and predictions are removed after each iteration.

Chapter 5 Conclusions

5.1 Main Results

In this dissertation, I examine the earthquake source parameters (stress drop, corner frequency, moment, source radius) with a variety of resources including different methods, different instrument records and different types of earthquakes, and investigate the uncertainties associated with source parameter estimations. Then the source parameters are used to study the relationship between stress changes of small/micro- earthquakes and tectonic settings and subsurface structures.

Here I summarize the major findings in the previous chapters:

In Chapter 2, I analyze the source parameters including stress drop and source parameters for small earthquakes recorded by the HRSN borehole stations. By applying the proposed spectral decomposition and stacking method, I find the stress drops of larger magnitude earthquakes (Mw>1.5) have minimized scattering and almost no magnitude dependence, while the earthquakes with Mw<1.5 still suffer from resolution issue due to instrument limitations. This indicates self-similarity for earthquakes in this region. It is also found that different corrections for subsurface material properties can lead to different stress drops for the same earthquakes, and different interpretations about magnitude or depth dependence. These well-resolved stress drops contribute to the finding that the stress distributions vary significantly at different patches on the fault. Within a few patches that are strongly influenced by the 2004 M6 Parkfield earthquake, a rapid decrease and a gradual recovery of stress drop are observed, suggesting a large earthquake can cause changes in the subsurface stress distributions. However, these temporal changes are small compared to the background stress heterogeneity, and do not change the spatial patterns of stress drop distributions, which suggests that the crustal stress distribution is more likely controlled by heterogeneous fault structures.

In Chapter 3, I design a series of tests on real data recorded by both the high-resolution borehole network (with high sampling rate and low noise) and the regional surface network (with low sampling rate and high noise) in Parkfield, CA, to investigate the influence of data limitation and methodology on source parameter estimations. These results suggest that with sufficient bandwidth, different methods can lead to similar stress drops for the same earthquakes. However, when the bandwidth is insufficient, measurements of stress drops using different methods can vary significantly. These results suggest that when interpreting the stress drop patterns or scaling relationship, one should carefully consider the potential influence of data and method limitations. Cross-validation using multiple approaches is important to ensure proper interpretation.

In Chapter 4, I perform a complete workflow to process raw data to analyze the source processes of microseismic events during hydraulic fracturing. I build an event catalog by detecting events and locating these events via a calibrated 1D velocity model, and apply an improved spectral analysis method to examine the source parameters including source radius, relative magnitude and relative stress change (approximation of stress drop). I find that the source radius for microseismic events is nearly constant with magnitude, and the relative stress change increases significantly with magnitude, which differs from the self-similar scaling found in the previous two chapters and other previous studies with natural earthquakes or induced earthquakes occurring on pre-existing faults. This could be ascribed to the mixed source mechanisms of these microseismic events (i.e., tensile failure due to fracture opening versus shear failure on faults). Another finding is that these microseismic events exhibit spatial migration patterns following the fluid diffusion curve, and the relative stress change, source radius and relative magnitude increase when events are farther from fracturing point. These observations may be indications of pore pressure variation over time and space during the hydraulic fracturing operations, which influence source processes of seismic events.

5.2 Potential Future Research

The estimated stress drop and other source parameters could be applicable to studies that involve slip inversion, stress field inversion or ground motion prediction. Consistency of stress drop from different studies and datasets is important to understand the relationship of ground motion between small and large earthquakes. *Trugman and Shearer (2018)* and *Pennington et al., (2021)* found strong correlation between event stress drop and ground motion between-event residuals. Accurate measurement of small earthquake parameters can help improve the robustness of the Ground Motion Prediction Equations (GMPE), allowing more accurate extrapolation from the abundant observations of small earthquakes to infrequent large earthquakes.

Another potential direction may be to attempt to improve the traditional analysis workflow of source parameter measurements with state-of-the-art techniques. Deep Learning (DL) has been proved to be capable of solving high-dimensional non-linear problems based on big data, such as image identification (*Deng et al., 2009*) and semantic segmentation (*Long et al., 2015*). There are some current applications of different deep learning models including Convolutional Neural Network (CNN), Fully Convolutional Network (FCN), etc. in the seismology community for earthquake detection, location, focal mechanism and spectral analysis (*Kuang et al., 2021; Mousavi et al., 2020; Rajguru et al, 2018; Ross et al., 2018*). Similarly, the source parameter estimation can benefit from these new techniques. For example, deep learning models can measure corner frequency that exceeds traditional resolution limit by learning well-resolved and labeled corner frequency estimates, or identify different types of earthquakes based on the shape of spectra.

References

Jia Deng, Wei Dong, Socher, R., Li-Jia Li, Kai Li, & Li Fei-Fei. (2009). ImageNet: A large-scale hierarchical image database, 248–255. https://doi.org/10.1109/cvprw.2009.5206848

Kuang, W., Yuan, C., & Zhang, J. (2021). Real-time determination of earthquake focal mechanism via deep learning. *Nature Communications*, *12*(1). https://doi.org/10.1038/s41467-021-21670-x

Long, J., Shelhamer, E., & Darrell, T. (2015). Fully convolutional networks for semantic segmentation. In *Proceedings of the IEEE conference on computer vision and pattern recognition* (pp. 3431-3440).

Mousavi, S. M., & Beroza, G. C. (2020). A Machine-Learning Approach for Earthquake Magnitude Estimation. *Geophysical Research Letters*, *47*(1). https://doi.org/10.1029/2019GL085976

Pennington, C. N., Chen, X., Abercrombie, R. E., & Wu, Q. (2021). Cross Validation of Stress Drop Estimates and Interpretations for the 2011 Prague, OK, Earthquake Sequence Using Multiple Methods. *Journal of Geophysical Research: Solid Earth*, *126*(3), 1–24. https://doi.org/10.1029/2020JB020888

Rajguru, G., Bhadauria, Y. S., & Mukhopadhyay, S. (2018). Estimation of Earthquake Source Parameters Using Machine Learning Techniques. *2018 9th International Conference on Computing, Communication and Networking Technologies, ICCCNT 2018*.

Ross, Z. E., Meier, M. A., & Hauksson, E. (2018). P Wave Arrival Picking and First-Motion Polarity Determination With Deep Learning. *Journal of Geophysical Research: Solid Earth*, *123*(6), 5120–5129. https://doi.org/10.1029/2017JB015251

Trugman, D. T., & Shearer, P. M. (2018). Strong correlation between stress drop and peak ground acceleration for recent M 1–4 earthquakes in the San Francisco bay area. *Bulletin of the Seismological Society of America*, *108*(2), 929–945. https://doi.org/10.1785/0120170245